UNIVERSITÀ DEGLI STUDI DI NAPOLI
FEDERICO II

UNIVERSITÀ DEGLI STUDI DI NAPOLI FEDERICO II

PH.D. THESIS IN

INFORMATION TECHNOLOGY AND ELECTRICAL ENGINEERING

INNOVATIVE APPLICATION OF FIBER OPTIC SENSORS IN HIGH ENERGY PHYSICS EXPERIMENTS

FRANCESCO FIENGA

TUTORS: PROF. GIOVANNI BREGLIO

DR. SALVATORE BUONTEMPO

XXIX CICLO

SCUOLA POLITECNICA E DELLE SCIENZE DI BASE
DIPARTIMENTO DI INGEGNERIA ELETTRICA E TECNOLOGIE DELL'INFORMAZIONE

to Giovanna

ABSTRACT

This thesis describes the innovative applications to the monitoring in harsh environment, represented by the Compact Muon Solenoid (CMS) detector at the Large Hadron Collider (LHC), of the Fibre Bragg Grating (FBG) technology, which, although invented almost 40 years ago, is currently undergoing an explosion in variant manufacturing technologies and applications. The environment inside a large particle physic experiment like the CMS poses several challenges of monitoring spatially varying quantities in an aggressive environment, with high radiation, high magnetic field, tight electromagnetic compatibility (EMC) requirements, where particle detection priorities require monitoring sensors to have very low mass and associated service volume as well as excellent EMC compliance, conditions that can be very well satisfied by FBG-based sensors inscribed on optical fibres. The particular application described here is the monitoring of strain and temperature variation along the beryllium central beam pipe, a vacuum chamber which carries the counter-rotating proton beams in the Large Hadron Collider (LHC) to collisions within the CMS experiment.

ACKNOWLEDGMENTS

An undertaking of this sort would not have been possible without the support of the people I've come across in these years of PhD.
Throughout the duration of this Thesis work I have enjoined and benefited from innumerable discussions with my Tutors, Giovanni Breglio and Salvatore Buontempo.
I am grateful to Giovanni Breglio who gave me the unique opportunity to join the DIETI Department, at the University of Napoli Federico II, as a Doctoral Student. As thesis director, Giovanni Breglio provided me with help and support on numerous occasions but, at the same time, he gave me responsibilities fostering my professional and personal growth.
I am proud to have worked under the supervision of Salvatore Buontempo. I met Salvatore in March 2013 when, after my MSc graduation, I went to CERN as a physicist involved in the CMS upgrade activities during LS1. Working under his supervision, I immediately appreciated his knowledge and skills. Thanks to the discussions we had at that time, I got fascinated from the fiber optic sensors technology and its applications in the high energy physics domain and I firmly decided to pursue the way of the PhD focusing on this technological topic. During these years he guided me, being open to my initiatives and always suggesting to me the best for my research after examining my work with critical look. Salvatore went well beyond his duty of thesis co-director: he has been a mentor and a friend.
This Thesis work profited from the support of the Central Technical Coordination of the CMS experiment. I acknowledge Austin Ball (Technical Coordinator of the CMS Experiment), Wolfram Zeuner (Deputy Technical Coordinator of the CMS Experiment), Christoph Schaefer (former CMS LEXGLIMOS, Large Experiment Group Leader In Matters Of Safety) and Niels Dupont (CMS LEXGLIMOS) for their truly support and interest in the project and in the present and future, planned, upgrades of the iPipe system. Notwithstanding his busy agenda, Austin Ball followed all the developments of the iPipe project, up to the careful reading of this manuscript. I sincerely thank him for accepting the duty of officially evaluating this Thesis and for his valuable advices that have been precious for the achievement of this final version of the present manuscript.

I want to express my gratitude to Leandar Litov (Associate Professor in Particle Physics and Head of the Atomic Physics Department at the University of Sofia St. Kliment Ohridski) and to Alfredo Guemes (Full Professor for Materials Science at the Dpt. of Aeronautics, Universidad Politècnica de Madrid) for accepting the duty of officially evaluating this Thesis and for their clear comments and suggestions.
My work has been framed in the FOS4CMS group, which is well represented by the Hungarian colleagues, Zoltan Szillasi and Noemi Beni. I am grate for the time spent together *playing* with the fiber gratings and debugging software, and for all the logistic support they gave me (including an endless chocolate supply in the office!).
From the very beginning of my PhD activity, I had the chance to interact with Andrea Gaddi (CERN-EP-CMX-EI) head of the CMS Integration Office. I could benefit from his deep knowledge of the engineering challenges that are implied from the complex and fascinating structure of the CMS detector. His contribution was crucial in the detailed design of the iPipe monitoring system, and its upgrade.
Particular thanks are due to the CMS Tracker colleagues: Nicola Bacchetta and Erik Butz. The fruitful discussions I had with them have been fundamental for the understanding of the thermal dynamic inside the CMS Tracker volume and its effect on the iPipe measurements.
Thanks to the involvement of Wolfram Zeuner, I had the possibility to discuss the results of my analysis with Christine Vollinger (CERN-BE-RF-BR) and Benoit Salvant (CERN-BE-ABP-HSC) in the framework of the LHC Impedance Working Group. I want to acknowledge their propositive interest in the iPipe technology and data analysis which poses the basis for the forth chapter of this Thesis, opening several future perspectives for the application of the proposed technology in the field of particle accelerator. I would like to thank prof. Vittorio Vaccaro for the clarifying discussions we had concerning the RF beam induced heating.
I want to thank Alessandro Masi (CERN-EN-STI-ECE) for his willingness to share with us his facility and his strong interest in activities related to my thesis work.
Many people contributed to the successful achievement of the results of the here presented project. I would like to acknowledge Stefano Sgobba, Floriane Leaux (CERN-EN-MME-TN) for making possible the detailed study on the interaction between the glue and the metallic structure of the central beam pipe; Patrick Lepeule and Nicolas Zelco (CERN-TE-VSC-BVO) for their support during the delicate operations of the handling of the central beam pipe; Remy Gauthier (CERN-TE-MSC-MDT) for his precious contribution in the gluing of the sensors on the precious central beam pipe; Nebojsa-Boki Smiljkovic (CMS Integration Office) for his willingness in providing me with several detailed technical drawings of different sectors of the CMS detector and for his contribution in addressing various issues related to the integration of the iPipe monitoring system in CMS.

During the development of the project I benefit from questions, suggestions, criticisms and advices from the CERN colleagues involved in fiber optic sensing activities, Paolo Petagna and Gaia Maria Berruti (CERN-EP-DT-FS) as well as from the colleagues of the Optoelectronic Division of the University of Sannio, Andrea Cusano and Marco Consales.
A special thanks to the Optosmart engineers, Armando Laudati and Fabio Mennella. They shared with me their deep expertise, promptly reacting to all my technical requests.
I wish to thank my colleagues from the DIETI OptoPowerLab: Andrea Irace, Michele Riccio, Luca Maresca, Gianpaolo Romano and Paolo Mirone. Together with Giovanni Breglio, they welcomed me in the DIETI Department. A mention goes to Michele Riccio, the beating heart of the OptoPowerLab, for *having kept warm* my desk during all the periods I spent at CERN.
Thanksgiving is a duty towards Daniele Riccio, Coordinator of the PhD in Information Technology and Electrical Engineering, for the work done for the fulfillment of this XXIX PhD cycle, and towards the administrative staff of CMS, INFN Napoli and DIETI for their support in the logistic and bureaucratic aspect of the several period I spent abroad during my PhD.

Un grazie sincero a tutti gli amici che hanno condiviso con me le emozioni di questi anni, indipendentemente dalle distanze spaziali e temporali che spesso ci hanno separato.
Sono infinitamente grato ai miei genitori per il sostegno incondizionato e l'incoraggiamento a perseguire le mie scelte e non posso non ringraziare Erri, parte integrante della mia famiglia.
Questa tesi la dedico alla donna che in questi anni mi è stata accanto, supportandomi e sopportandomi. Non so immaginarmi senza ...
Grazie Giovanna.

CONTENTS

LIST OF FIGURES

INTRODUCTION

The work related to this Thesis is focused on the development of an innovative fiber optic monitoring system, based on the Fiber Bragg Grating (FBG) technology, for the structural and thermal monitoring of a high energy accelerator beam pipe. The beam pipe instrumented is the central beam pipe of the Compact Muon Solenoid Experiment (CMS), at the European Organization for Nuclear Research (CERN), which is part of the Large Hadron Collider (LHC) and is the place where the high energy LHC high energy particles collisions take place. It has to stand to an extreme vacuum condition (up to 10^{-13} atm) and, at the same time, it must not interfere with the particle resulting from collisions. Indeed, it is made of a beryllium tube section, 3m long with a central diameter of 45mm and 0.8mm thickness wall, sealed on the two extremities with two conical aluminium sections, each 1.5m long. The central beam pipe is a fundamental element of both the CMS experiment and the LHC ring. It needs to be continuously monitored in order to secure relevant informations about its structural and thermal state.
The proposed monitoring system consists of four single-mode optical fibers placed along the cardinal longitudinal positions on beam pipe cross section. On each fiber, 16 FBGs have been manufactured: 7 are glued on the pipe to measure the local strain and the remaining 9, for each fiber, are left unglued but in contact with the pipe in order to work as local thermometers and as temperature compensators for the adjacent strain sensors. The designed system allows the monitoring of any deformation induced on the CMS central beam pipe during the experiment motion during maintenance periods and magnetic field induced ones during operation phases. Moreover, the uniqueness of the iPipe monitoring system sensing position, whose FBG sensors are placed on the outer surface of the CMS central beam pipe, in direct contact with the metallic surface of the vacuum chamber, allows to measure for any thermal dynamic taking place on the vacuum chamber structure.
This thesis is organized as follows.

- Chapter 1 is dedicated to the fiber optic sensors technology, centering the discussion on the FBG sensors. An overview of the working principle

will be given together with a detailed and well documented state-of-the-art of the effects of ionizing radiation on the fiber gratings.

- Chapter 2 has the challenging goal of motivating the need for high precision measurements in the CMS environment. An introductory description of both the LHC accelerator and the CMS detector is given in order to help the reader understanding the complexity of the environment and given that the beam vacuum chamber, to be instrumented as the main objective of this Thesis, is an important part of both entities. Special attention is given to the description of the several FBG monitoring systems active in CMS to set the scene for the introduction of the iPipe project.
- Chapter 3 deals with the iPipe project. The preliminary studies are explained in details together with all the problematics encountered during the commissioning and operation of the system, which have been part of the core issues of this Thesis work. The radiation effects on the iPipe FBGs are discussed and the unique results from the strain monitoring of the CMS central beam pipe are shown.
- Chapter 4 is devoted to the application of the iPipe sensors to the direct monitoring of the beam-induced heating. The physical basis of this phenomenon are explained and documented leading to the interpretation of the iPipe temperature data in the framework of the beam impedance. The uniqueness of this results triggered the interest of the community and an upgrade of the system has been proposed, installed and is undergoing the commissioning phase in order to be ready for the restart of the LHC collisions.
- The conclusions summarize the main achievements realized during this thesis, underlining the open issues and possible improvements of FBG based monitoring system for particles accelerators beam pipes and equipments.

1 FIBER BRAGG GRATING

1.1 FIBER OPTIC SENSORS

An optical fiber sensor system could be seen as composed by a light source, a detector and a transducer, as shown in Figure 1. Generally, the source consists in lasers, diodes or LEDs, the transducer could be optical fibers or doped fibers or bulk materials and, at the output of the system, a photodetector is used to detect the variation in the optical signal that has been caused by the physical perturbation of the system. As optical fiber sensors operate by modifying one or more properties of light passing through the fiber, they can be broadly classified as extrinsic or intrinsic, as shown in Figure 2.
Intrinsic optical sensors directly employ an optical fiber as the sensitive material and also as the medium to transport the optical signal with information of the perturbation environment to be measured. In this case the light does not leave the fiber to perform the sensing function, except at the detection end of the sensor. In case of extrinsic sensors, on the other hand, the optical fiber is simply used as mean to carry light to and from a location at which an optical sensor head is located. The sensor head is external and usually is based on optical components which are designed to modulate the properties of light in response to changes in the environment with respect to the physical perturbations of interest. The intrinsic fiber sensor types are more attractive and widely researched as this scheme has many advantages compared to extrinsic, such as their in-fiber nature and the flexibility in the design of the fiber sensor head, [8].
Optical fiber sensors can also be further classified according to their spatial positioning. For example, a point sensor can be used to sense measurands from discrete points while distributed fiber sensors provide spatial and temporal information of the measurand from any point along a single fiber with a certain resolution. A style of sensor that is in between these two configurations is represented by the quasi-distributed scheme, where the measurand information is obtained at particular and pre-determined points

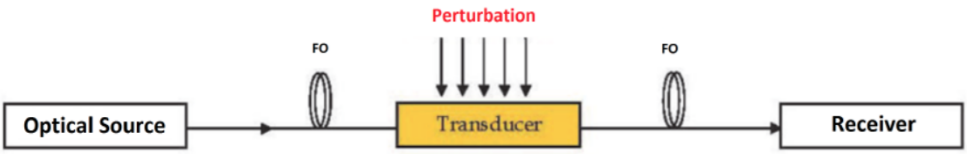

Figure 1: Basic components of an optical fiber-based sensing system

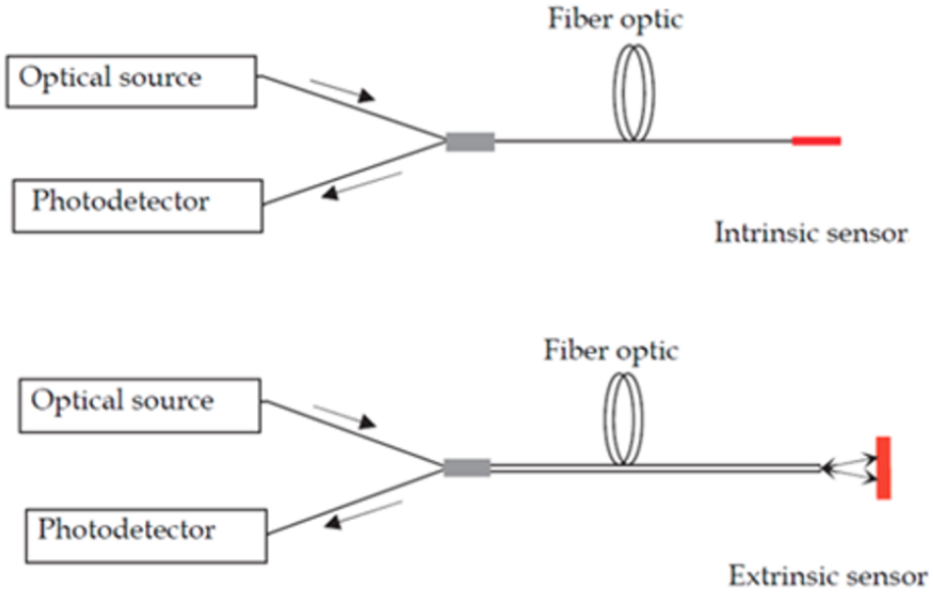

Figure 2: Intrinsic and extrinsic fiber optic sensors

along all the length of a fiber network, [9]. A schematic of the three major sensing schemes, point, distributed and quasi-distributed, is illustrated in Figure 3.

1.2 FIBER GRATING SENSORS

Fiber gratings [10] consist of a periodic perturbation of the optical fiber properties, generally of the core refractive index. Those sensors can be classified, based upon the period of the grating (Λ) into two main types:

- Fiber Bragg Grating (FBG), if Λ is of the order of μm,
- Long Period Grating (LPG), if Λ is several hundreds of μm.

Their working is based on the coupling of a propagating core mode and other modes of the core or the cladding. The phase-matching condition to be satisfied is given by [11]:

$$\Delta\beta = \frac{2\pi}{\Lambda} m \tag{1}$$

where $\Delta\beta = \beta_1 - \beta_2$ is the difference between propagation constants of the involved modes, referred to as 1 and 2, and m is an integer number, called order. This coupling reflects in the presence of one or more attenuation peaks in the transmission spectrum, whose position depends on the grating

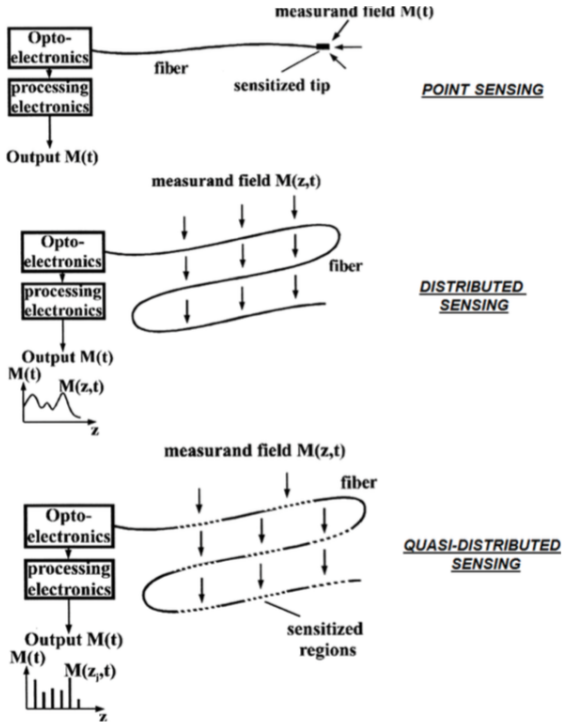

Figure 3: Point, distributed and quasi-distributed optical fiber-based sensing

characteristics but also in external factor, such as temperature and strain. From these consideration, we can state that at the basis of the fiber grating sensors these is a wavelength, or a frequency, measurement.

1.2.1 Fiber Bragg Grating

A fiber Bragg grating (FBG) [12] couples light from a forward-propagating mode to the backward, counter-propagating mode, in the core of an optical fiber. In this case, $\beta_2 = -\beta_1$ and $\Delta\beta = 2\beta_1$ results in a period Λ of the order of magnitude of μm [11]. The coupling occurs at a specific wavelengths, named Bragg wavelengths and defined as [13]:

$$\lambda_{Bragg} = 2 \cdot n_{eff} \cdot \Lambda / m \tag{2}$$

where n_{eff} is the effective refractive index of the propagating core mode and m is the order. So, the transmission or reflection spectra of a FBG show a narrow dip or peak centered at λ_{Bragg}, respectively, as shown in Figure 4.

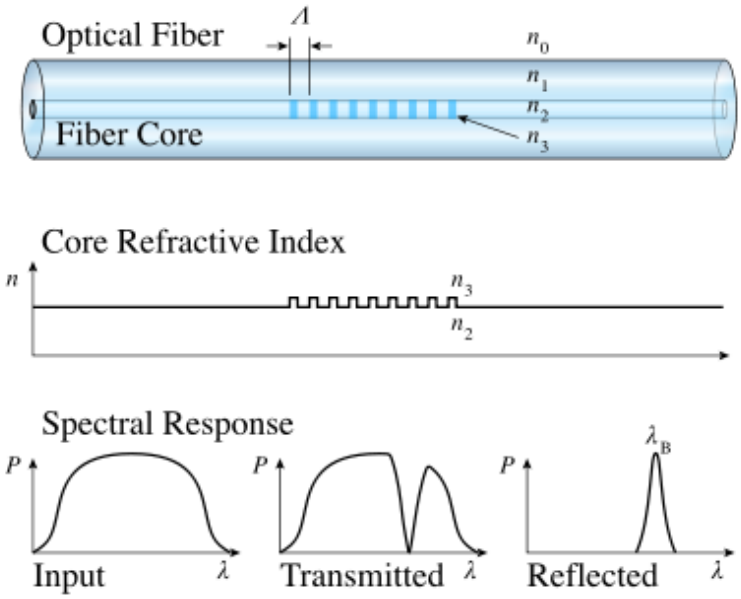

Figure 4: Principle of operation of a fiber Bragg grating sensor.

1.2.2 Long Period Grating

A Long Period Grating (LPG) contributes to couple light of a propagating core mode (the fundamental one) with discrete co-propagating cladding modes (indicated by their order n); in this case, $\beta_2 = \beta(n) > 0$ and $\Delta\beta$ is small, resulting in a period Λ of some hundreds of micrometers [11], [14]. As the cladding modes are quickly attenuated, the transmission spectrum of the grating contains a series of attenuation bands: each band corresponds to the coupling to a different cladding mode and it is centered at a wavelength defined as [14]:

$$\lambda(n) = \delta n_{eff} \cdot \Lambda \tag{3}$$

where $\delta n_{eff} = n_{eff} - n_{clad}^{(n)}$, n_{eff} and $n^{(n)}$ are the refractive indices of the propagating core mode and of the n^{th} cladding mode. The wavelength of the attenuation bands depends on several external parameters, such as temperature, strain and refractive index of the medium around the cladding [15], [11].

1.3 FBG TECHNOLOGY

A fiber Bragg grating consists of a periodic modulation of the refractive index in the fiber core formed by its exposure to an intense light interference pattern. At each index variation a small amount of light guided along the fiber core is reflected and all the reflections add coherently at a well

determined wavelengths, called Bragg wave-lengths and defined in Eq. 2. The formation of permanent grating was first demonstrated by Hill et al. in 1978, [16]. They excited a germania-doped optical fiber with intense argon-ion laser radiation at 488 nm and observed that after several minutes the intensity of reflected light increased until almost all the light was reflected from the fiber. The growth in back reflected light was explained in terms of non linear effect called photosensitivity, which permits the index of refraction in the core of the fiber to be increased by exposure to intense laser radiation. In this early experiment, a fiber Bragg grating was formed when a small amount of the laser light reflected back from the end of the optical fiber interferes with the exciting laser light to establish a wave pattern. The index of refraction increases to greater extent at position where constructive interference results in a maximum of laser intensity. As the strength of the grating, which is proportional to the depth of its index modulation, increases the intensity of the back-reflected light increases until it saturates. Although photosensitivity appeared to be an ideal means for fabricating these early Hill gratings in optical fibers, their usefulness was extremely limited because they only reflected at wavelengths in the visible close to the wavelength of the writing light, were spread along the optical fiber with varying strength and took a long time to produce. These limitations were overcome 10 years later by Meltz et al. in 1989, [17], who recognized from the work of Lam and Garside, [18], that photosensitivity was a two photon-process that could be made more efficient if it were a one-photon process corresponding to the germania oxygen vacancy defect band, at a wavelength of 245 nm (i.e. 5 eV), [13]. In the experiment of Meltz the fiber was irradiated form the side with two intersecting coherent ultraviolet laser beams of wavelength 244 nm, which corresponds to one half of the 488 nm, the wavelength of the blue argon laser line.

The transverse holographic method worked since fiber cladding is transparent to UV light, whereas fiber core is highly absorbing of this radiation. The principal advantage with regard grating fabrication is related to the fact that spatial period of photo-induced perturbation depends on intersecting angle between the two interfering beams. This permits a versatile and efficient fabrication of custom Bragg gratings operating at much longer wavelengths than the writing wavelength. The periodic perturbation of the core index of refraction gives rise to successive coherent scattering for a narrowband band of the incident light. The grating thus effectively acts as a stop-band filter, reflecting light with wavelengths close to the Bragg wavelength, and transmitting wavelengths sufficiently different from resonance condition. Each reflection from a peak in the index perturbation is in phase with the reflection from the next peak when the wavelength of the light corresponds to the Bragg wavelength as shown in Figure 4.

Theoretical formulations based on coupled mode theory [19] have been developed to analyze fiber grating spectra by Erdogan et al., [1]. Successively, a variety of different continuous wave and pulsed lasers with wavelengths

ranging from the visible to the vacuum UV have been used to write gratings in optical fiber. In practice, krypton-fluoride (KrF) and Argon fluoride (ArF) excimer lasers that generate (10ns) pulses at wavelengths of 148 and 193 nm, respectively, are used most frequently to produce FBGs. The exposure required to produce a FBG is typically a few minutes with laser intensities of 100 to 1000 mJ/cm^2 and pulse rates of 50 to 75 s^{-1}. Under these conditions, the change in the core index of refraction is between 10^{-5} and 10^{-3} in germanium doped single-mode optical fiber.

Techniques such as hydrogen loading proposed by Lemaire in 1993 can be used to enhance the optical fiber photosensitivity prior to laser irradiation [20]. Hydrogen diffusion makes the core more susceptible to UV laser radiation. Changes in refractive index of the order of 10^{-2} have been achieved by this means. Successively, the transverse holographic method of writing fiber Bragg gratings has largely been superseded by the phase mask technique in 1993 [21]. Phase mask is a thin slab of silica glass into which is etched (using photolitographic techniques) a one-dimensional square wave periodic surface relief structure. Since this material is transparent to UV laser radiation the primary effect of the phase mask is to diffract the light into the 0, +1 and -1 diffraction orders. Careful control of the depth of the corrugations in the phase mask suppresses zero-order diffraction, leaving the +/- 1 diffracted beams to interfere and produce the periodic pattern of intense laser radiation needed to photoimprint a Bragg grating in the core of an optical fiber. The photoimprinted index grating pariod will be the half of the phase mask period. Note that grating period is independent of the writing radiation wavelength.

Although, the usual practice brings the optical fiber almost into contact with phase mask, Othonos in 1995 demonstrated the improvements in the spatial coherence of the laser writing, relaxing the need for such close contact [22]. The phase mask technique greatly simplifies the manufacture of FBGs through easier alignment, reduced stability requirements on the photoimprinting apparatus, and lower coherence demands on the laser beam. It also permits the use of cheaper UV excimer laser source and tends to consistently yield high performance gratings. The prospect of manufacturing high performance gratings at low cost is critical to the large scale implementation of this technology for sensing applications. The main drawback associated to this approach relies to the need of separate phase mask for each grating with a different operating wavelength. On the other hand, it results very flexible since it can be used to fabricate gratings with controlled spectral responses characteristics. As a consequence of technological assessment, in the mid 1990's many research groups have been engaged in the study and realization of new grating devices through more complex refractive index modulation profiles. Examples include apodized FBGs, chirped FBGs, tilted FBGs, phase shift FBGs and long period fiber gratings [23], [24].

The commercial transition did not happen until the mid 1990's and was

subsequently strongly driven by communications needs and the ramping up of the telecommunications bubble, which saw a tremendous explosion of the number of companies and research groups engaged with the design, fabrication, packaging and use of gratings. First companies to produce commercial FBGs were 3M, Photonetics and Bragg Photonics in 1995. Soon after the telecommunications bubble collapse, there was a significant shift by many players in the industry from communications to sensing applications. At the time, this was a prudent and strategic move on the part of FBG manufacturers to keep exploiting the technical and manufacturing infrastructure. As FBGs made the transition from optical communications devices to sensing elements in the 1990s, the bulk of the sensing applications centered on discrete, single-point sensing of specific parameters-such as strain and temperature-using sensors based on embedded or packaged gratings. These early gratings were typically written using phase masks or side exposure interferometric techniques. These fabrication methods initially relied heavily on manual skills and labor, severely limiting many of the features and performance of the gratings in terms of production capacity, repeatability, mechanical strength, as well as number and quantity of FBGs written on a continuous fiber. Due to this increasing interest in FBG sensing technology, many research studies were devoted to the conception of optoelectronic unit able to demodulate FBGs based sensors.
However, the sensor industry is much more cost sensitive, demanding multiple sensing points and greater mechanical strength. Such requirements also call for the capability to fabricate an array of multiple FBGs at different locations along a same length of optical fiber. Such needs are being addressed by more sophisticated, on-line, reel-to-reel fabrication processes and systems that allow the writing of complex FBG arrays along a single fiber spool, [25], [26].

1.4 FBG THEORY IN PEANUTS

Several theoretical works have been trying to determine the optical properties of gratings, depending on:

- magnitude of effective refractive index (n_{eff}),
- period of the refractive index perturbation (Λ),
- grating length (L),
- number of grating periods (N), defined as L/Λ,
- refractive index modulation amplitude (Δn^{mod}), defined as the difference between the refractive index of the zones illuminated and not,

- modal overlap factor (η), which defines the amount of the power guided by the core and can be calculated as [27]:

$$\eta = \frac{\pi^2 \phi_{core}^2 NA^2}{\lambda^2 + \pi^2 \phi_{core}^2 NA^2} \tag{4}$$

  where ϕ_{core} in the core diameter.

From the well-known coupled-mode theory, the reflectivity (R) of uniform gratings, as a function of wavelength, can be expressed as [28], [18]:

$$R = \frac{\sinh^2\left(\kappa L\sqrt{1-\left(\frac{\delta}{\kappa}\right)^2}\right)}{\left(1-\left(\frac{\delta}{\kappa}\right)^2\right)\cosh^2\left(\kappa L\sqrt{1-\left(\frac{\delta}{\kappa}\right)^2}\right)+\left(\frac{\delta}{\kappa}\right)^2\sinh^2\left(\kappa L\sqrt{1-\left(\frac{\delta}{\kappa}\right)^2}\right)} \tag{5}$$

where $\kappa = \pi/\lambda_{Bragg} \cdot \eta \cdot \Delta n^{mod}$ is known as the coupling coefficient, $\delta = 2\pi n_{eff}/\lambda - \pi/\Lambda$ and δ/κ in the detuning ratio, depending on λ/λ_{Bragg}. Fig. 5 shows, as example, the profile obtained for an uniform grating with $\kappa L = 2$. The maximum value of R occurs at λ_{Bragg} (*i.e.* $\delta = 0$) and is [1]:

$$R_{max} = \tanh^2(\kappa L) \tag{6}$$

Another important parameter is the grating width, in particular the full width, defined as the distance between the first two minima, is given by [1]:

$$width = \lambda_{Bragg}\sqrt{\left(\frac{\Delta n^{mod}}{n_{eff}}\right)^2 + \left(\frac{\lambda_{Bragg}}{n_{eff}L}\right)^2} \tag{7}$$

In the weak grating case ($\Delta n_{mod} << \frac{\lambda_{Bragg}}{L}$), the filter bandwidth is limited by the FBG length, whereas in the strong grating case ($\Delta n_{mod} >> \frac{\lambda_{Bragg}}{L}$), the light does not penetrate the full length of the grating and the bandwidth is dependent only on the refractive index modulation amplitude.

1.5 FBG AS A SENSOR

The FBG response is sensitive to external factors. Indeed, any change which varies the refractive index or grating period, such as strain and temperature, will change the Bragg wavelength, making the grating a very good intrinsic sensor, with the information wavelength-encoded and independent of the signal intensity [13]. When a force ΔF is applied to the grating the signal will change according to the following formula:

$$\frac{\Delta\lambda_{Bragg}}{\lambda_{Bragg}} = \left(1 + \frac{1}{n_{eff}}\frac{\delta n_{eff}}{\delta S}\right)\left(\frac{1}{\Lambda}\frac{\delta\Lambda}{\delta F}\right)\Delta F \tag{8}$$

where S is the strain. A typical value for the sensitivity to an applied axial strain is 1 nm/millistrain, for a grating at 1300 nm, [16].

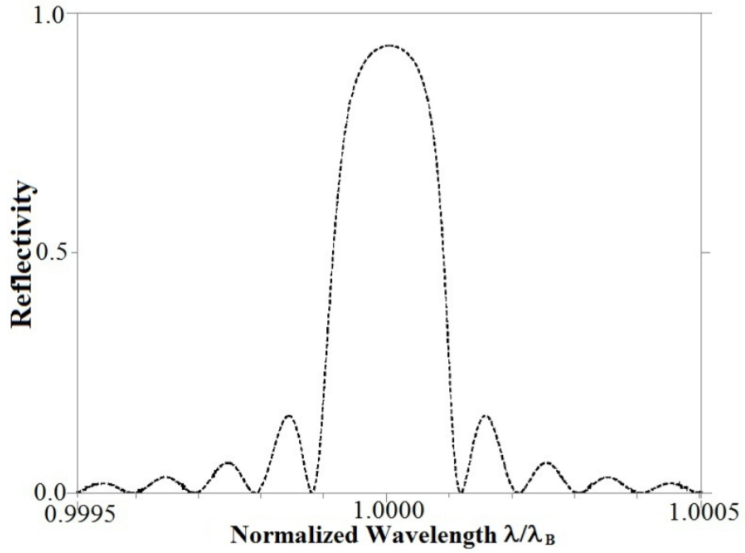

Figure 5: Reflection spectrum versus normalized wavelength for an uniform Bragg grating with $\kappa L = 2$ [1].

If there is a temperature variation of ΔT, the central wavelength of the grating will shift according to the relation:

$$\frac{\Delta\lambda_{Bragg}}{\lambda_{Bragg}} = \frac{1}{n_{eff}}\left(\frac{\delta n_{eff}}{\delta T}\right)\Delta T + \frac{1}{\Lambda}\left(\frac{\delta\Lambda}{\delta T}\right)\Delta T \tag{9}$$

where:

- $\frac{\delta n_{eff}}{\delta T}$ in the thermo-optic coefficient, about $10^{-5}/°\text{C}$ [29]
- $\frac{1}{\Lambda}\left(\frac{\delta\Lambda}{\delta T}\right)$ is the thermal expansion coefficient, about $0.5 \cdot 10^{-6}/°\text{C}$ at RT [30].

A typical value of the temperature coefficient of a bare grating at 1550 nm is about 0.01 nm/°C and it is primarily due to the thermo-optic effect [16]. However, it also depends on the fiber coating, particularly on its material and thickness, indeed by increasing the coating thickness it increases with a saturating trend [31]. The temperature sensitivity also decreases if the grating peak is at shorter wavelengths [32].

1.6 TYPES OF GRATINGS

The gratings different types are classified according to the laser source used for their writing: the UV laser can be pulsed or continuous wave, whereas the IR source has to be ultrashort pulsed.

1.6.1 UV-FBGs

The phenomenon behind the UV-FBG formation is the photo-sensitivity of silica doped with specific elements, primarily the germanium. In the past decades, gratings were written with all types of lasers, continuous wave or pulsed, emitting light at different wavelengths. Nowadays, the most commonly used light sources are KrF and ArF excimer lasers emitting, respectively, 248 and 193 nm pulses with a duration of $\sim$10 ns at repetition rates of 50-75 Hz. The exposure of a Ge-doped fiber to UV light for few minutes at intensities of 100-1000 mJ/cm^2 causes an increase of the refractive index ranging between 10^{-5} and 10^{-3} but it can reach 10^{-2} by loading the fiber with H_2 [13]. During inscription n_{eff} and Δn^{mod} increase, indeed the peak position shifts towards longer wavelengths, while the peak width and reflectivity increase [33]. The relation between Δn^{mod} and the incident fluence (I) depends on the excitation photon energy. For the gratings writing with an ArF excimer laser, Malo et al. found a dependence of the growth rate on I^2, indicating a two-photon process, in which the carriers are generated by direct excitation in the silica bandgap and then they are trapped at Ge-related defects [23]. The thermal stability of gratings depends on the fiber composition and the inscription conditions but, generally, they do not withstand temperatures higher than 600°C. This is related to the defects originating Δn^{mod}: studies about the fluence dependence of the Ge-related defects and Δn^{mod} and their thermal stability showed that the grating formation is mainly associated with the generation of GeE' and GeH centers and indeed it is the much higher formation efficiency of these centers that gives rise to the much higher photosensitivity of H_2-loaded fibers [34].
Most commonly observed are Type I FBGs. This name refers to FBGs, whose formation is accompanied by a monotonous increase of the refractive index modulation amplitude. Type I gratings can be written under continuous or pulsed UV radiation with intensity below 10 MW/cm^2 in various types of fibers, whether photo-sensitized or intrinsically photo-sensitive. The inscription mechanism corresponds to single-photon absorption at pre-existing sites located in the band gap.
By increasing the pulse energy beyond a threshold value the induced refractive index modulation does not grow anymore linearly with the pulse energy but increases very quickly up to saturate around $5 \cdot 10^{-3}$. The gratings written in this regime are labeled as Type II FBGs [35]. Such gratings show high temperature stability because the refractive index changes are related with glass structural changes. Indeed, studies with optical microscope show that laser damage, responsible for the index change, is limited to the core-cladding interface [35]. Those gratings exhibit high reflectivity and large bandwidth and they withstand temperatures up to 800°C. However, their use is limited by their poor quality spectra.
If the Type I grating writing is not stopped when the grating is formed, but the fiber is further exposed to the UV light a regenerated grating appears,

called Type IIA grating, [36]. In contrast to the initial Type I grating, this new grating shows a steady blue shift during the growth of its strength, which explains the name "negative index grating". These gratings are written in highly Ge-doped, B/Ge or Sn/Ge co-doped fibers, with or without H_2-loading [37]. Their inscription is characterized by a non-monotonic evolution in both modulation and effective index, with three phases. Initially, n_{eff} and Δn_{mod} increase and a Type I grating is written. Then, by increasing the accumulated laser energy [37] or by subjecting the grating to a thermal treatment at high temperature, as 700°C [38], the Type I grating is erased and n_{eff} and Δn_{mod} decrease, until the starting point of the regeneration process is reached: Δn_{mod} starts to increase again, while n_{eff} decreases, implying the blue-shift of the initial central wavelength.
Another type of regenerated gratings is Type IA gratings, which are written after erasure of a Type I grating in hydrogenated germano-silicate fibers. Differently from the Type IIA, a large red wavelength shift during inscription is measured [39]. Also in this case the wavelength shift occurs in three phases [40]: an initially rapid increase of the Bragg wavelength, followed by a slower growth up to reach a plateau at a saturation value that depends on fiber type, hydrogenation and irradiation conditions. Type IA exhibit the lowest thermal sensitivity among all the FBG types [39], [41], whereas the strain response remains unchanged [41]. Similarly to Type IIA, Type IA gratings are formed in B/Ge co-doped fiber. The difference is the use of hydrogen loading for Type IA gratings inscription.

1.6.2 IR fs-FBGs

The FBGs inscription can be made also using 800 nm femtosecond radiation [42]. The fs-laser is focused into the core of the fiber and induces local refractive index changes in a point-by-point writing process. The process is highly nonlinear and therefore basically independent of the fiber material, which means that doping the fiber is not required. The FBGs can be written in radiation insensitive fibers and special pure core fibers for harsh environments.
The grating formation is characterized by a threshold for the pulse peak intensity, which mainly depends on the temporal and spatial qualities of the laser light and the accuracy of the alignment of the incident beam onto the fiber core [43], and also on the presence of dopants in the fiber, which decrease the threshold [44]. Above this peak intensity threshold, a grating will be written, but increasing the peak intensity two regimes of induced index change are observed: in analogy with the UV-FBGs, the two types gratings are referred to as type I-IR and type II-IR [45].
Compared with the traditional UV-laser method, the photosensitivity of the fiber material and the hydrogen loading treatment are not required in the fs-laser approach [46]. Owing to the ultrahigh peak power of the fs-laser, the FBGs can be inscribed in the fiber made of any material. This latter

consideration makes the fs-FBGs an attractive solution for sensing in high radiation environment using special radiation tolerant fibers.

1.7 EFFECTS OF γ–RADIATION ON FIBER GRATINGS

During the last two decades, several experimental research have investigated the FBG sensor technology behavior in ionizing radiation environment, a detailed review of the achieved results can be found in [4].
Ionizing radiation induces changes in both the refractive index (Δn_{eff}) and the period ($\Delta\Lambda$) of a fiber grating resulting in a Bragg wavelength shift (BWS):

$$\frac{\Delta\lambda_{Bragg}}{\lambda_{Bragg}} = \frac{\Delta n_{eff}}{n_{eff}} + \frac{\Delta\Lambda}{\Lambda} \tag{10}$$

From the studies reported in literature, it can be stated that under γ-radiation the central wavelength of a fiber Bragg grating shifts towards the red exhibiting a saturated trend. The BWS saturation values and at the respective accumulated doses depend on the fiber chemical composition and the conditions of the grating inscription. This rule is not followed by the N-doped silica fiber whose Bragg wavelength does not show a saturation effect, at least up to a 1.5 MGy dose [47]. The H2-loading used to make easier the grating inscription causes a higher sensitivity to radiation. Recent studies showed that the most resistant gratings under γ-radiation are the FBGs written in fluorine-doped fibers with the more recent technique that uses femto-second radiation at 800 nm [48]: $\Delta\lambda_{Bragg}$ saturates around 5 pm at low γ-doses, $\sim$5 kGy. The experimental investigation of the radiation effects on the FBGs is focusing the attention of the research with the aim of applying this technology to the monitoring of radiation hazardous environment, like present and future nuclear power plants [49]. These argument will be addressed in more details in the following sections of this chapter, while in the next chapter the application to the harsh environment represented by an high energy physics experimental facility will be explained.
Only few studies have been published concerning the behavior of LPGs when exposed to ionizing radiation. As for FBGs, a peak shift is observed as a consequence of the radiation induced refractive indices (Δn_{eff} and $\Delta n_{clad}^{(n)}$) and period ($\Delta\Lambda$) change:

$$\frac{\Delta\lambda^{(n)}}{\lambda^{(n)}} = \frac{\Delta n_{eff} - \Delta n_{clad}^{(n)}}{n_{eff} - n_{clad}^{(n)}} + \frac{\Delta\Lambda}{\Lambda} \tag{11}$$

The effect of γ-radiation on standard LPGs written in N-doped and Ge-doped fibers has been investigated by Vasiliev et al. [50]. Within the experimental error of $\pm$ 0.3 nm, any radiation induced change in the transmission spectra has been revealed after a cumulated dose of 9.3 kGy

(dose rate of 6.6 Gy/s).
The turn-around-point long period grating (TAP-LPG) [51] exhibit a trasmission spectra characterized by dual resonant peaks due to coupling to higher order cladding modes. Under radiation, both peaks shift in different directions with high sensitivity and indeed they are good candidates as dosimeters [52].
The chiral long period grating (CLPG) is characterized by a periodic modulation of the optical properties of the fiber achieved by twisting the fiber as it passes through a miniature oven. The period greatly exceeds the optical wavelength so that core and cladding modes can be coupled to produce several narrow dips in the transmission spectrum. Even if their radiation sensitivity depends on the fiber composition, the CLPG are very sensitive to radiation with a dip shifts up to 10 nm after a γ-dose of 100 kGy has been cumulated [53].
Since this Thesis work has focused on the application of FBG sensors, the next sections of this chapter will be devoted to the explanation of the FBG sensing technology.
In the following paragraphs a review of the radiation effects on the FBG types reported in section 1.6 will be given.

1.7.1 UV-FBGs

The radiation influences the position, amplitude and FWHM of the Bragg peak, depending on the grating parameters and the writing conditions as well as the used fiber. Generally, the ionizing radiation induces a red Bragg wavelength shift with a saturating tendency. The red-shift results from the increase of the average effective index n_{eff} [54]. For the germanosilicate fibers, as demonstrated by Neustruev et al. [55], the γ-irradiation can be considered as a further UV-light exposure since it creates the same paramagnetic defects as the UV-light. Moreover, the γ-radiation should affect only the mean value of n_{eff} and not the modulation amplitude Δn_{mod} [56].
Two main reason can be addressed to explain the saturating behavior [57]: the limited concentration of precursor defects, which are responsible for the refractive index change, and the competition between the annealing and the generation of the defects [2], that is also dependent on the radiation dose-rate and the annealing rate.
In general, the BWS depends on the manufacturing parameters [2, 58], *e.g.* composition of the optical fiber, hydrogen loading, annealing, and on the irradiation parameters, *e.g.* dose rate, temperature.
In Figure 6 the BWS, under identical manufacturing and irradiation conditions, of several grating made in different fibers doped with germanium, boron, phosphorous, cerium or nitrogen to achieve the photosensitivity. As demonstrated by Henschel et al. [2], it is not possible to find a clear correlation between the observed radiation sensitivity and the fibers composition.

Therefore, fibers that show higher radiation induced attenuation (RIA) do not give rise to gratings with higher radiation sensitivity. The cause is that the grating inscription with high UV light intensity changes the fiber properties so much that the resulting material can no longer be compared with that of the initial fiber and even the defect generation by ionizing radiation in this new material will be different [2]. However, Lin et al. observed in B/Ge co-doped fibers that the higher the GeO_2 concentration, the higher the FBG radiation sensitivity, easy to explain as the formation of more Ge-related color centers [59]. Before the writing of the grating, the

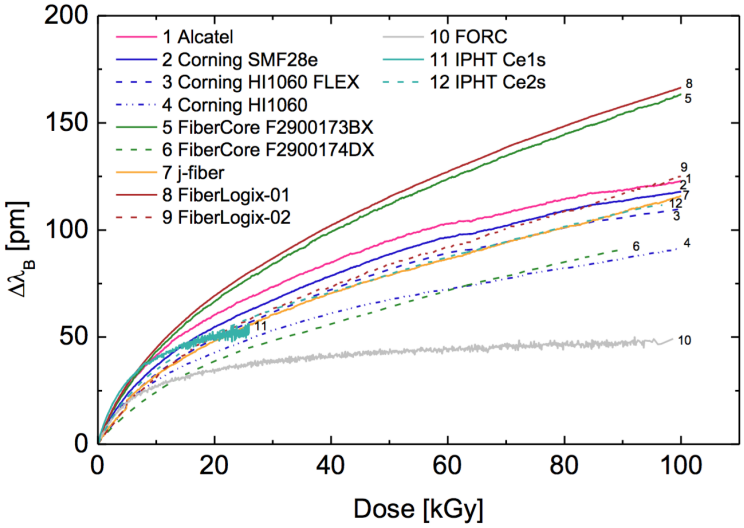

Figure 6: Bragg wavelength shift of gratings made of different fibers, during γ-irradiation at RT up to 0.1 MGy, with dose-rate of 0.9 Gy/s [2].

photosensitivity of the fiber is enhanced with the H_2-loading and, consequently, after the writing an annealing has to be performed to accelerate the hydrogen out-diffusion and stabilize the grating. Increasing the fiber sensitivity to UV light, the hydrogen increases also the radiation sensitivity of gratings. Indeed, BWS saturates at higher shift levels and at higher doses for gratings written in loaded fibers than in the unloaded [47, 59, 60]. A probable reason of the high radiation-sensitivity of gratings written in hydrogen-loaded fibers is the radiolytic rupture of the OH-bonds, whose concentration increases with the H_2-loading [60].

Except special fiber coatings, it is not possible to write gratings with UV light without removing it since it absorbs such wavelengths. In practice, gratings have to be inscribed in bare fibers that has to be re-coated after the grating writing process. The coating influences the grating radiation-sensitivity [61]: the exposure ionizing radiation modifies the structure of the coating, which can shrink or swell, resulting in a Bragg wavelength shift. However, it can be thought that the coating could shield rays. This shielding effect has to be considered only for UV light or X-rays of

very low energy, but not for γ-rays with an energy of about 1 MeV [58].
Besides the fiber, the conditions of writing and using could also influence the grating response under radiation. The grating radiation sensitivity does not depend on the writing UV laser light, for example its wavelength [62]. It depends on the Bragg wavelength initial value and it increases with increasing λ_{Bragg} [32], whereas it depends slightly on the fiber tension during the grating inscription, decreasing by increasing the tension [58].
It has been experimentally demonstrated that the sensitivity of the grating to ionizing radiation is independent of the light power used for measuring the spectra [62] even if, by the phenomenon known as photo-bleaching, the light power increasing reduces the fiber RIA.
The dose-rate also influences the grating sensitivity. Indeed, it has been observed that by increasing the dose-rate, the BWS saturates at higher shift levels and at higher doses [63]. Also the irradiation temperature play a role, since increasing the temperature facilitates the defect annealing resulting in a decrease of the BWS [58]. Finally, it has been observed that a pre-irradiation could reduce the radiation sensitivity, because during the pre-irradiation most of the precursors is converted [59]. However, this effect depends on the post-irradiation recovery [54].
As described in the previous section, the Type II grating is damage grating in any kind of fiber. This implies that the radiation sensitivity of this type of grating is defined by the fiber properties [2]. In Figure 7 a comparison between the BWS of a Type I and a Type II grating written in the same kind of photosensitive fiber is shown, highlighting the lower radiation sensitivity of the Type II grating [2]. Type IA gratings are formed in standard

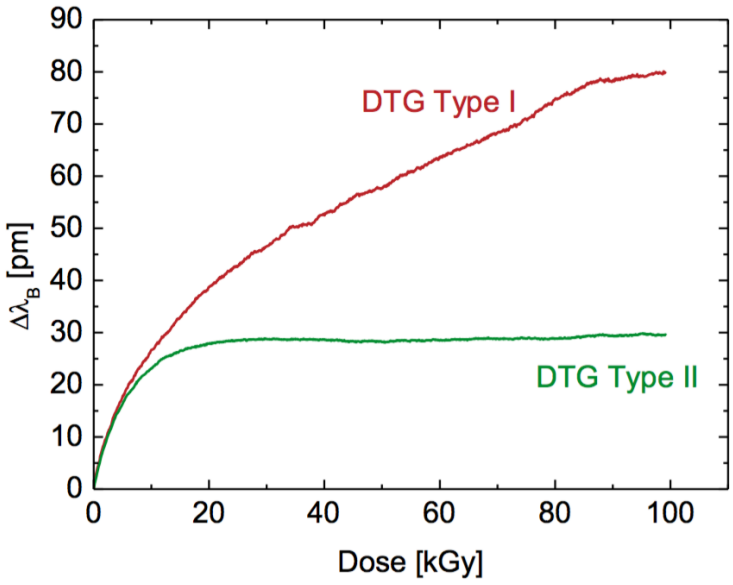

Figure 7: Comparison of the BWS in Type I and Type II gratings [2].

telecommunication hydrogen-loaded fibers following fiber UV pre-exposure. If the pre-exposure is not done a standard Type I grating is formed, meaning that both Type I and Type IA gratings can be written in one fiber. Faustov et al [3] performed a comparison study, irradiating with γ from a Co^{60} source pairs of Type I - Type IA gratings written in the same fiber section. Two types of fiber were used: a B/Ge co-doped fiber Fibercore PS-1250/1500 and a highly Ge-doped fiber Fibercore SM-1500. All fibers were hydrogen loaded. From the results reported in the plot in Figure 8 it can be stated that Type IA FBGs are more radiation sensitive with respect to standard gratings. Moreover, Type IA gratings exhibit a faster post-radiation relaxation: after a sufficiently long time the BWS changes its sign and this behavior is observed for both boron-containing and boron free fibers. It was concluded that the damage to the glass matrix due to the UV blank exposure, combined with the presence of trapped hydrogen, is responsible for both, the high ionizing radiation sensitivity of Type IA gratings, and their post-irradiation annealing behavior. The results also indicate the possible role of boron for the radiation sensitivity enhancement [3]. Type IIA FBGs are regenerated gratings and can

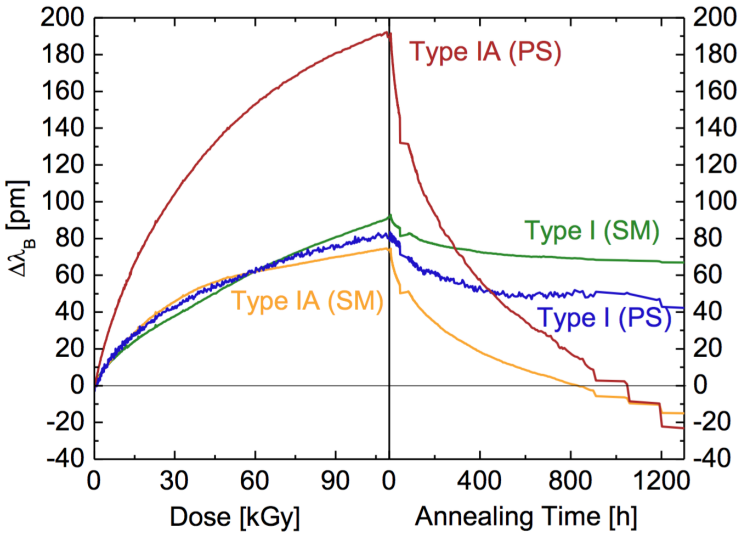

Figure 8: Comparison of the BWS in Type I and Type IA gratings [3].

be inscribed in highly Ge or Ge/B co-doped fibers without hydrogen loading. Gusarov et al. [61] found that the Type IIA FBGs are more radiation resistant as compared to Type I FBGs written in the same fiber. A saturation trend is observed also for Type IIA gratings but with no significant post-irradiation recovery.

Finally, several works show that the temperature sensitivity of the UV FBGs is not influenced by radiation [47, 64, 2, 65].

1.7.2 IR fs-FBGs

The radiation effects on Type I-IR and Type II-IR femtosecond FBGs were studied for the first time by Grobnic et al. [48]. Fig. 9 shows the radiation-induced BWS in FBGs written in the standard Ge-doped fiber Corning SMF-28, proving that the H_2-loading increases the radiation sensitivity, especially for Type I-IR gratings, that exhibit higher BWS with respect to the Type II-IR gratings. Moreover, BWS saturating behavior is observed only for the gratings made in unloaded fibers, at levels that are similar for both grating types and depend only the fiber composition. On the same plot, the BWS of UV Type I FBGs are also shown [2], showing a behavior similar to that observed for the Type I-IR FBGs.
The radiation-induced BWS is larger in the fiber with higher RIA at λ_{Bragg}, however it has been observed that a RIA difference of more than two orders of magnitude leads to a BWS difference of less than a factor 10 [48].
A major advantage of fs-IR gratings is the possibility to write gratings with

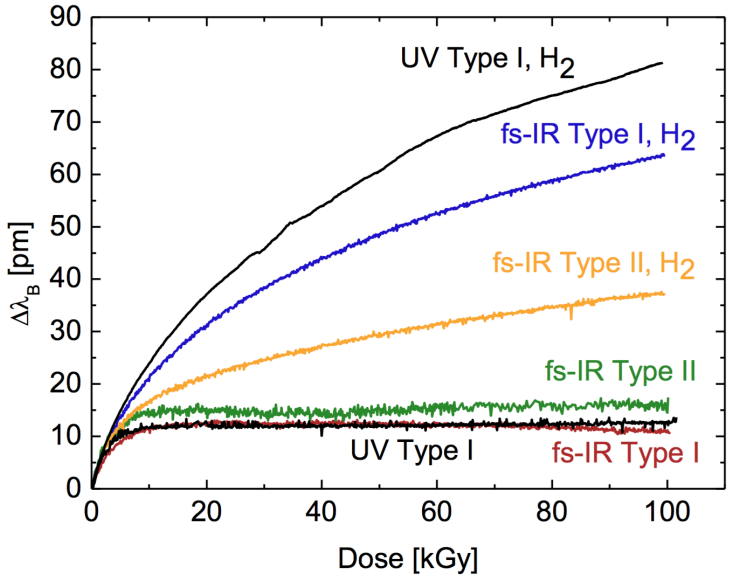

Figure 9: Comparison of BWS for fs-IR-FBGs and UV-FBGs written in a Corning SMF-28 with and without hydrogen loading [4].

a very good reflectivity inside almost any fiber, making possible the manufacturing of very radiation hard FBGs. Indeed, in Figure 10 the BWS of Type II-IR gratings written inside a pure silica fiber (PSC), fiber 2 of Table I (Corning) and two very radiation hard fluorine doped fibers (Fujikura and Draka). It is remarkable that the BWS of the FBGs written inside the F doped fibers is only a few pm up to a dose of 100 kGy and they even stay below 5 pm up to 1 MGy at a slightly higher dose rate [66]. Radiation-induced temperature sensitive coefficient changes were below the measurement

accuracy, meaning that such gratings are good candidate for sensing in high radiation dose rate environments [4].

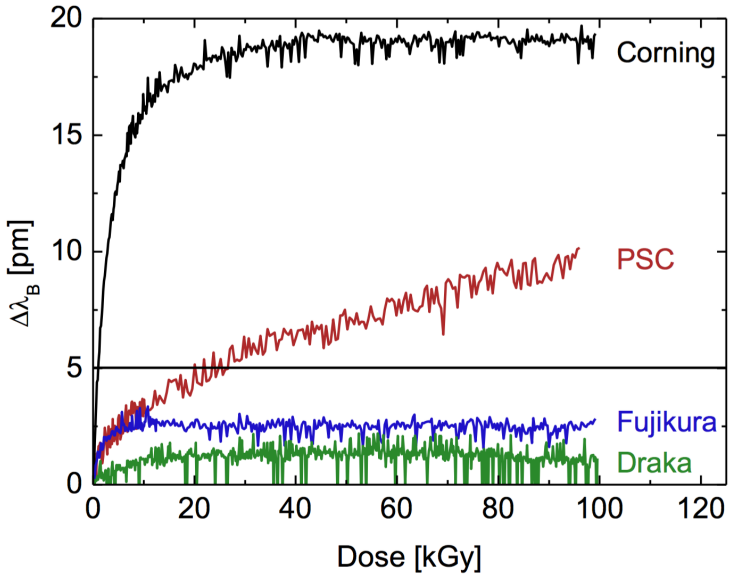

Figure 10: BWS of Type II-IR FBGs written inside a Corning SMF-28, a PSC fiber and two fluorine core doped fibers from Fujikura and Draka [4].

1.8 EFFECTS OF MIXED γ–NEUTRON RADIATION

As just seen, a lot of papers have been published until now about the γ-radiation tolerance of the gratings. In contrast, very few tests were performed on the gratings in nuclear reactor cores and all on the standard gratings: type I-UV FBGs. The sensitivity of the Bragg wavelength to mixed γ-neutron radiation is higher than that to pure γ-radiation [67]. λ_{Bragg} red-shifts showing a saturating behavior under a neutron flux lower than $1.5 \cdot 10^{11}$ n $cm^{-2}s^{-1}$, with a γ-dose-rate up to 180 Gy/h, whereas under an higher neutron flux (lower than $1.5 \cdot 10^{14}$ n $cm^{-2}s^{-1}$), with a γ-dose-rate up to 9 MGy/h λ_{Bragg} increases almost linearly with increasing dose without any saturation and the peak width also increases, indicating the grating erasure. Annealing at high temperatures and pre-irradiation do not improve the grating radiation stability [68]. As for the γ-radiation, the hydrogenation increases the grating sensitivity: the wavelength shift, the amplitude reduction and the peak broadening are bigger for the grating written in loaded fibers than in the unloaded one [67], [68], [69]. The temperature sensitivity does not change because of the radiation [69].

1.9 INTERROGATION TECHNIQUES AND MULTIPLEXING

The interrogation system, which processes the back-reflected FBG sensors optical signal, represents the key element of monitoring systems in terms of both performance and cost [70]. The requirements for FBG interrogation systems are low power, high resolution, high speed, small size and capability to deliver real-time measurements. FBG sensors require expensive optical sensing interrogator to achieve all these performances. FBG have been extensively accepted by engineers and have become the most prominent sensors for structural health monitoring (SHM), because of their high accuracy. The typical resolutions and the measure ranges of the FBG sensors are the ones required by civil engineering: resolution as low as 1 $\mu\epsilon$ and 0.1 °C, which translates into a wavelength resolution of about 1 pm, strain measurement ranges in the order of 10 $m\epsilon$ and more than 200 °C as temperature operating range. Whereas this wavelength resolution is easily achieved with expensive laboratory instrumentation, the ability to resolve changes on this order using small, packaged electro-optics units able to operate on the field is more of a challenge. The choice of fiber Bragg interrogation method depends on the available optical component technology suitable for a specific application. The most straightforward method for interrogating a FBG sensors array is based on passive broadband illumination in the telecom C band (1530-1565 nm). A linear sensor array can be created in a single long optical fiber by writing a set of Bragg gratings with different and unique Bragg wavelengths or by bonding stubs of common optical fiber to different FBGs. FBG sensors wavelength spacing can be 1-2 nm, allowing up to a few tens to be multiplexed in a single fiber operating in the C band. Each FBG can be localized at any position along the optical fiber. However, minimum spacing and maximum number of gratings are ultimately ruled by cross-talk coming from multiple reflections and spectral shadowing. Thus the same optical fiber behaves as an array of stress sensors, as a multiplexing system and as the transmission medium. This makes it possible to have multi-point, as well as quasi-distributed sensing.
Light with a broadband spectrum which covers that one of an FBG sensor feeds the system, and the narrowband component reflected by the FBG is routed to a wavelength detection system. The two most important interrogation schemes are: wave division multiplexing (WDM) and the time division multiplexing (TDM). A TDM system employs a pulsed broadband light source and identifies different gratings of the same wavelength by the time taken for their return signals to reach a detector, being the returns from closer gratings received before those from more distant ones. A system of passive sloped filters can be used to determine the wavelength of each pulse as it arrives. Alternatively a high-speed spectrometer can be used. The key disadvantages of TDM systems is the requirement to have low reflectivity gratings, and to maintain a minimum spacing between the gratings to allow

the interrogator enough time to make a wavelength measurement. These disadvantages often limit the performance and practicality of a TDM measurement system. With a WDM system many gratings can be combined on a single fibre and addressed simultaneously provided each has a different Bragg wavelength. This is achieved in practice either by using a broadband light source and a spectrometer for detection, or an agile tunable or swept-wavelength light source and simple photodiode detectors. The interrogation unit used for the purposes of the work presented in this Thesis employs the latter method.

The state of the art of commercially available fiber Bragg grating interrogator is represented by Micron Optics products [71] which are designed specifically for fiber sensor applications.

2 FBG SENSING IN HEP: THE CMS EXPERIMENT AT LHC

2.1 THE LARGE HADRON COLLIDER

The Large Hadron Collider (LHC) is a particle accelerator and collider at the European Organization for Nuclear Research (CERN) near Geneva, Switzerland. The LHC is designed to accelerate bunches of either protons or heavy ions and bring them to collision at the centres of four particle detectors with a centre of mass energy up to $\sqrt{s} = 14$ TeV.
The LHC physics program is broad and diverse, ranging from precise measurements of Standard Model (SM) parameters to the search for new physics phenomena. One of its main goals is establishing the origin of the electroweak symmetry breaking, either by discovering the SM Higgs boson and measuring its properties or excluding it and looking for evidence for alternative mechanisms. It also enables searches for physics beyond the SM that could appear at the TeV scale, such as supersymmetrical particles, new heavy gauge bosons, technicolor particles or extra dimensions. The LHC is thoroughly described in [72].

2.2 LHC: AN OVERVIEW

The LHC is a circular accelerator. This topology allows the particles to be indefinitely recirculated through the accelerating sections, thus allowing to reach very high energies while keeping a relatively compact design. The highest energy accelerators that preceded the LHC, the LEP (Large Electron Positron) lepton synchrotron and the Tevatron hadron synchrotron were both circular accelerators. The LEP collided electrons with positrons at a centre of mass energy of up to $\sqrt{s} = 209$ GeV, while the Tevatron collided protons with antiprotons at a centre of mass energy of up to $\sqrt{s} = 1.96$ TeV. In order to pursue the goals of the LHC physics program, extremely rare processes need to be studied. The number of events per second generated in a collider via a given process is given by:

$$N = L\sigma \tag{12}$$

where σ is the cross section for the process under study and L the machine luminosity, which depends only on the beam parameters. The LHC was therefore designed to provide collisions with an unprecedented peak instantaneous luminosity of $L = 10^{34}$ cm^{-2}s^{-1}. At this luminosity, a light Higgs boson event would occur with an average frequency of ≈ 0.25 Hz. As

a comparison, at the maximum luminosity obtained at the Tevatron, $L = 5 \cdot 10^{32}$ cm^{-2}s^{-1}, a light Higgs boson event would only occur with an average frequency of the order of 10^{-4} Hz.
A circular collider's luminosity can be written as:

$$L = \frac{N_1 N_2 n_b f_{rev} \gamma}{4\pi\epsilon_n \beta^*} F \tag{13}$$

where N_1 and N_2 are the numbers of particles per bunch in each beam, n_b is the number of bunches per beam, f_{rev} in the revolution frequency, γ is the relativistic gamma factor for particles in the beam, ϵ_n is the normalized beam emittance which give a measure of how much the particles depart from the ideal trajectory, β^* is the beta function at the collision point giving the envelope for the particles' motion and F is the luminosity reduction factor due to the crossing angle at the interaction point. f_{rev} and γ are determined by collider radius and particle energy while all the other parameters may be controlled to maximize the luminosity.

2.3 DESIGN AND NOMINAL PARAMETERS

The LHC is housed in the tunnel which the LEP collider occupied until 2000. It uses superconducting resonating cavities to accelerate the two counter-rotating proton beams and superconducting magnets to bend them. The necessity for high luminosities dictated the decision to collide protons with protons instead of antiprotons as done e.g. at the Tevatron. While using antiprotons would have enabled a simplified collider configuration of a common vacuum and magnet system for both counter-rotating beams, antiproton production and storage are challenging processes. They would have imposed significant limits on the total number of particles in the antiproton beam, N_2 in equation 13 , thus bounding the maximum luminosity. Therefore two proton beams are used, each controlled by separate magnets.
The 26.7 km long tunnel straddles the French-Swiss border near Geneva; it lies between 45 m and 170 m underground and consists of eight straight sections, each about 528 m long, and eight arcs. The LHC would have longer arcs and shorter straight sections for the same circumference, thus requiring less intense magnetic fields to bend the beams. However reusing the existing tunnel was clearly the most cost-effective option. The straight sections serve as insertion regions: four of them house physics experiments, one the acceleration system, one the beam dump and the remaining two the beam cleaning systems. The arcs are occupied by magnets and the systems to make them functional. The overall layout of the tunnel is shown in figure 11. Due to space constraints in the tunnel the LHC uses twin bore magnets that consist of two sets of coils and beam channels within the same mechanical structure and cryostat. Each arc consists of 23 cells, each one composed of

dipoles for deflecting and quadrupoles for focusing the bunches. In order to focus the beam in both planes, a series of focusing and defocusing quadrupoles is arranged. In total there are 1232 main dipoles and 392 quadrupoles. In addition, sextupole, octupole and decapole corrector magnets are positioned to correct errors in the particle trajectory.
In this geometry structure the bending radius of the dipoles is about 2.8 km.

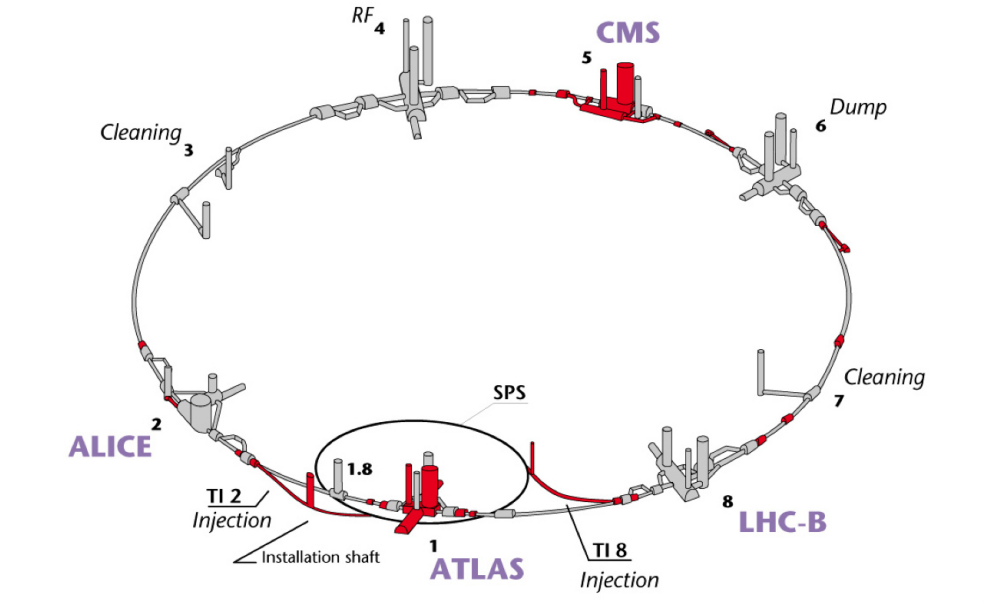

Figure 11: Layout of the LHC tunnel [5]. The red parts are new underground buildings built specifically for LHC. The grey parts represent existing LEP infrastructure.

The magnetic field needed to keep 7 TeV protons on a circular trajectory can be calculated as:

$$B = \frac{p}{e\rho} \tag{14}$$

where $p = \sqrt{E^2 - m^2}$ is the proton's momentum and ρ is the bending radius. Thus one obtains a peak dipole field of 8.33 T. Producing such a high field using a conventional electromagnet is unfeasible, due to extremely high currents and consequent heat dissipation. The LHC therefore uses superconducting magnets. In particular the magnet coils are made of niobium-titanium alloy, a superconductor with a critical temperature of 9.2 K. The coolant used is super-fluid helium at 1.9 K. Helium becomes super-fluid at 2.17 K. Super-fluid helium has the highest thermal conductivity of any known substance, making it a very good choice as a coolant. In this state it is also characterized by a complete absence of viscosity, which enables it to penetrate in the complex shape of the coils. The high-field super-conducting magnets operate in a static bath of pressurized super-fluid helium at 1.9 K,

cooled by continuous heat exchange with flowing super-fluid helium.
Before reaching the LHC, the particles are accelerated by a chain of accelerators that gradually increase the particles' energy. The protons start their journey to the LHC in the linear accelerator Linac2. This accelerator yields protons with an energy of 50 MeV which are then injected into the first circular accelerator of the chain, the Proton Synchrotron booster (PS), which increases the energy to 1.4 GeV. The protons are then transferred to the Proton Synchrotron (PS), that raises the energy to 25 GeV and organises them in bunches with about $1.15 \cdot 10^{11}$ particles each. From the PS the beam is injected into the Super Proton Synchrotron (SPS) where the energy of the bunches increases by a factor of almost 20 up to 450 GeV, which is the injection energy of the LHC. A schematic of the CERN accelerator complex is depicted in Figure 12.
The LHC acceleration system consists of 8 radio-frequency (RF) superconducting resonating cavities per each beam, that supply the protons with about 485 keV per revolution during the ramp phase from 450 GeV to 7 TeV. The RF cavities operate at a peak voltage of 2 MV at a frequency of approximately 400 MHz. This results in 35640 potential wells in the RF field, so-called RF buckets, where it is energetically favourable for the bunches to be located in the beam. This corresponds to a spacing in time of only 2.5 ns, but only every tenth RF bucket is used, making the minimum bunch spacing $\Delta t = 25$ns. The LHC therfore has $N_B = 3564$ possible locations, called buckets, where bunches can sit for each beam. The bunch patterns of the two counter-rotating beams together determine when there will be collisions in the the centre of the experiments. After acceleration the beams circulate in the machine for a period of typically 10-20 hours during which they are brought into collision.
In high-luminosity colliders, there is a non-negligible probability that one single bunch crossing may produce several separate events, a phenomenon known as pileup. The average number of superimposed events can be estimated as:

$$\mu = L\sigma_{pp}\overline{\Delta t} \tag{15}$$

where $\overline{\Delta t} = \Delta t \cdot (N_B/N_b)$ is the average bunch spacing. Assuming a proton-proton inelastic cross section of $\sigma_{pp} \approx 80$ mb, one obtain $\mu = 25$.

2.4 EXPERIMENTS

At the LHC experimental interaction points, four particle detectors reconstruct the collision events to perform detailed studies of known physics processes and to search for evidence of new physics. Two of them, ATLAS [73] and CMS [74], are general purpose detectors; ALICE [75] is dedicated to the study of the quark-gluon plasma, which is postulated to have existed during the early universe, using lead-ion collisions; LHCb [76] is targeted

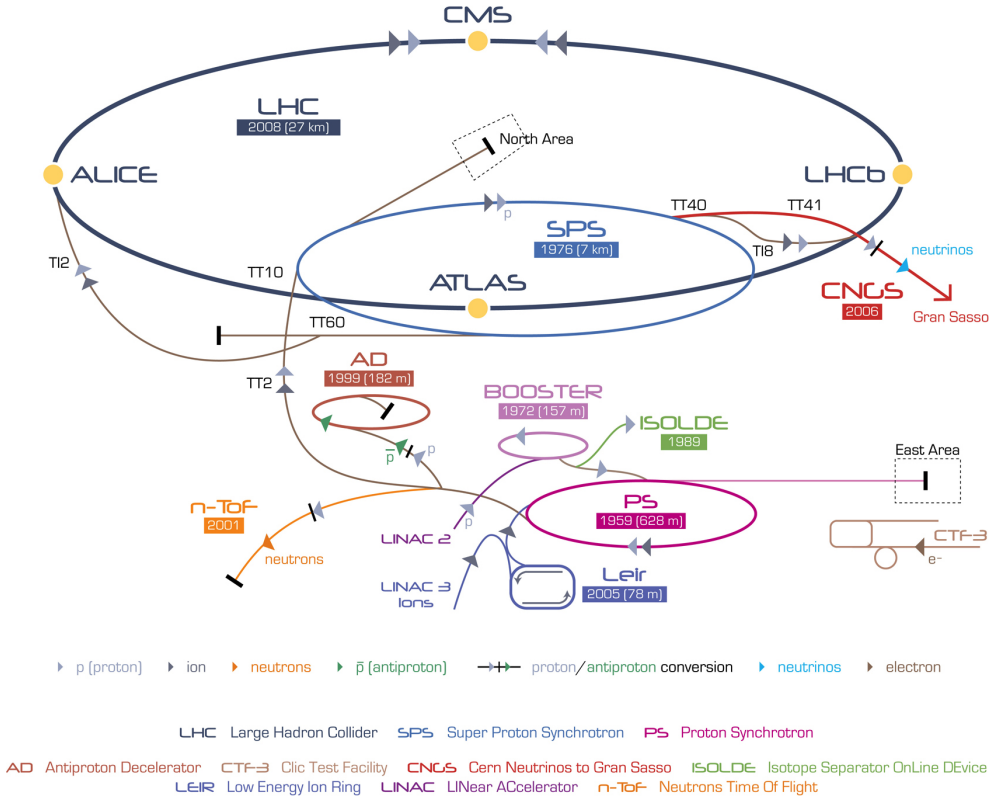

Figure 12: The CERN Accelerator Complex.

towards studying the decays of B hadrons in order to better understand the matter-antimatter asymmetry in the universe.

2.5 THE CMS EXPERIMENT

The Compact Muon Solenoid [74] is one of the two "general purpose" detectors at the Large Hadron Collider. It was designed with the aim to study a large spectrum of physical phenomena, starting from the completion of the Standard Model predictions looking for the Higgs Boson and up to the search for new physics beyond the Standard Model at the TeV scale.
The experiment is located in an underground cavern at LHC experimental point number five, near the french town of Cessy. The main feature of the detector is a strong super-conductive solenoidal magnet, which can reach a 4 T field and dictates the cylindrical shape of the experiment. Another characteristic of CMS is its modularity. This had made it possible to build CMS on surface, while the experimental cavern was being excavated, and it was lowered one section at the time in 2007. The magnet occupies the central region of the detector, called barrel, which is externally subdivided in 5 wheels. The wheels compose the iron yoke for the return of the magnetic fields, and contain the chambers for the detection of muons. The central wheel (designated wheel 0) is also the structural support for the magnet to which it's connected. The barrel region is closed on both ends by four instrumented iron disks called endcaps. Once closed, the detector is quite compact, being a cylinder 21.6 m long and with a diameter of 14.6 m. Its total weight is of about 14500 tons. In Figure 13 an expanded section of the CMS detector is shown, with highlighted the main sub-detectors.

2.5.1 CMS Coordinate system

The CMS coordinate system used to describe the detector is a right-handed Cartesian frame, centered in the interaction point and with the z axis along the beam line (this direction is referred to as *longitudinal*). The x axis is chosen to be horizontal and pointing towards the centre of the LHC ring, and the y axis is vertical and pointing upwards. The $x - y$ plane is called *transverse* plane.
Given the cylindrical symmetry of the CMS design, usually a (ϕ, θ) cylindrical coordinate system is used in the reconstruction of the tracks of particles. ϕ is the polar angle, laying in the $x - y$ plane, measured from the x-axis in mathematical positive direction (i.e. the y axis is at $\phi = 90°$. The azimuthal

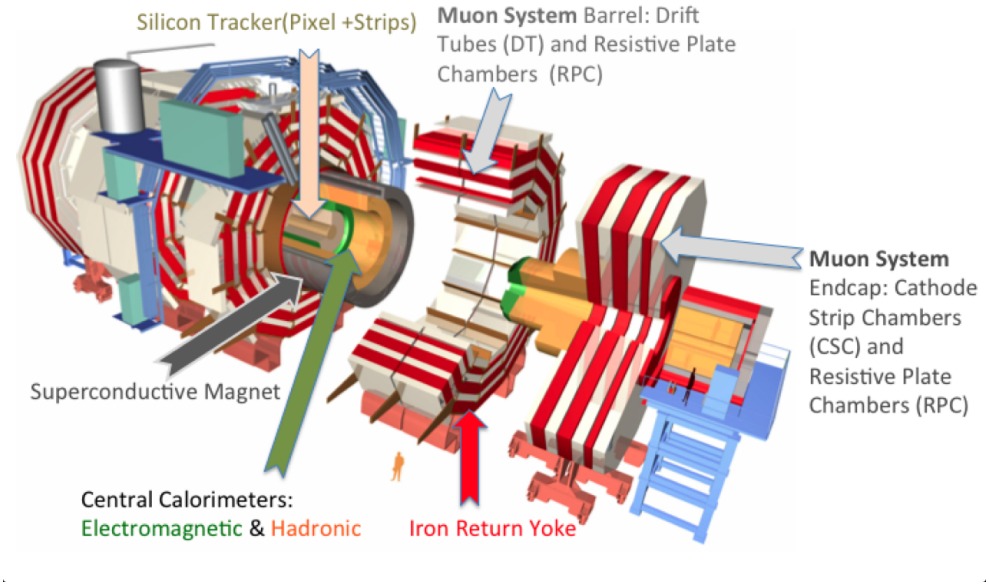

Figure 13: CMS schematic layout.

angle θ is measured from the z-axis towards the $x-y$ plane. The angle θ can be translated into the pseudo-rapidity η by:

$$\eta = -\ln\left(\tan\frac{\theta}{2}\right) \tag{16}$$

A longitudinal view of CMS detector displaying the segmentation η of the sub-detectors is shown in Figure 14.

2.5.2 The CMS Tracker

The CMS tracking , [77], is located inside the coil, and it is the first detector surrounding the interaction point. It is designed to allow a precise reconstruction of the trajectory of the charged particles produced in the collisions. The active envelope, as can been seen from Figure 15, extends to a radii of 115 cm, over a length of approximately 270 cm on each side of the interaction point, with a total sensitive surface of around 200 m^2. At the nominal LHC luminosity, every 25 ns typically 20 proton-proton collisions occur, producing around 1000 particles crossing the tracker volume. The flux of particles equates to have a high hit rate of 100 MHz/cm^2 at the innermost detector layer, decreasing to 300 kHz/cm^2 at the outermost. This imposes stringent conditions on the detector and readout electronics. To satisfy them the detector technology must provide high granularity combined with a fast readout, and be able to operate in this harsh environment for a expected lifetime of approximately 10 years.

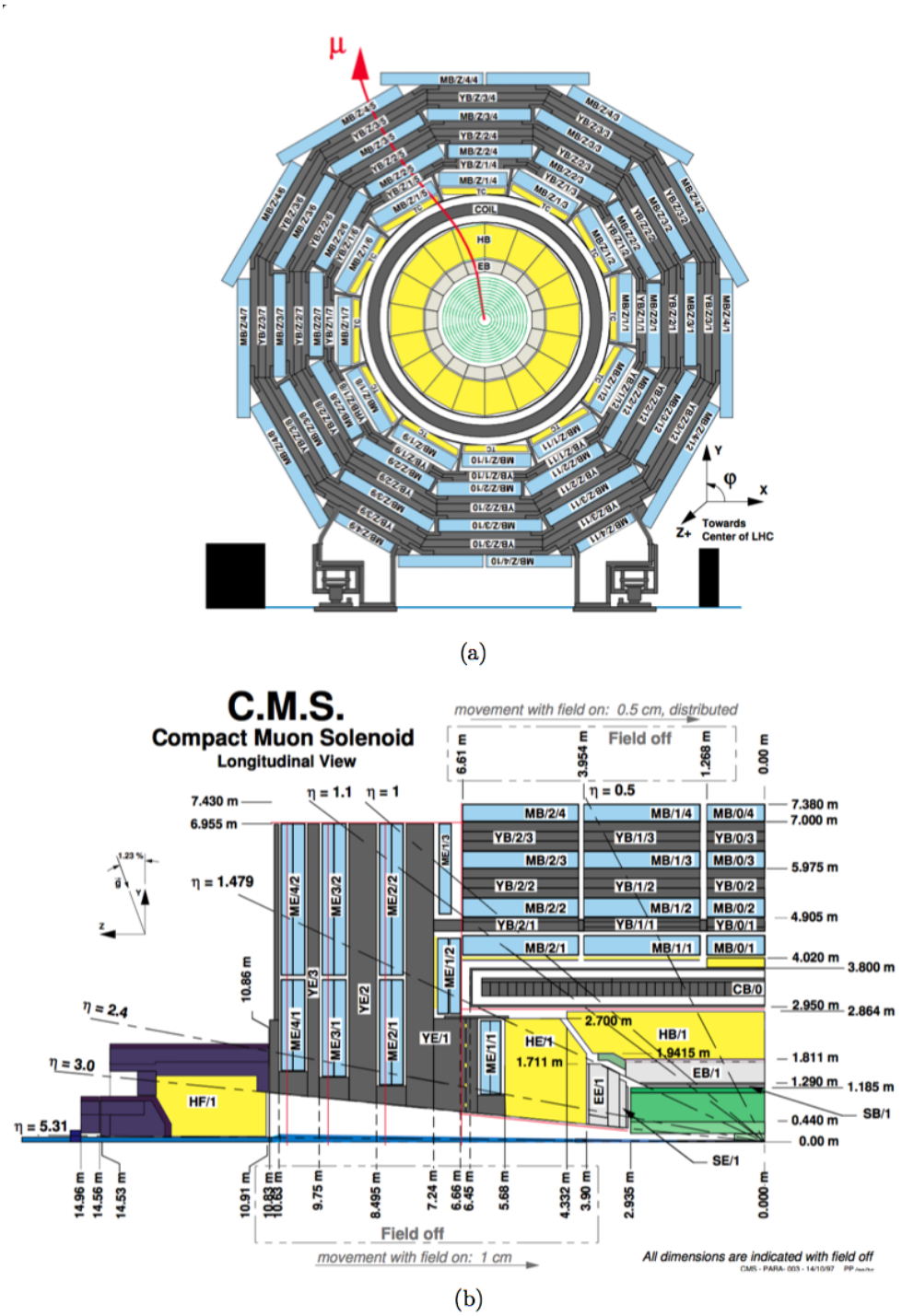

Figure 14: On (a) a transverse view of CMS in the barrel region. On (b) a longitudinal view of one quarter of the detector.

The CMS tracker consist of two parts instrumented with two technologies:

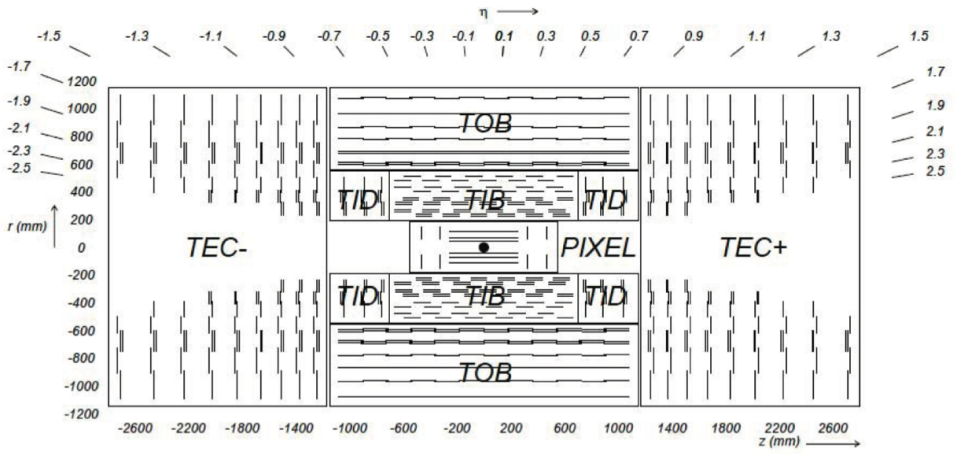

Figure 15: The tracker schematic structure.

Pixel detectors and Silicon Strips. The Pixel system is the first element after the collision point. The detector consists of two sub-detectors: the Barrel (BPIX) and Forward (FPIX). The BPIX is made of three layer detector with 53 cm long with layers at mean radius of 4, 7 and 11 cm. The FPIX has two layers at z = $\pm$ 34.5 and $\pm$ 46.5 cm with a radial coverage between 6 and 15 cm. The detector has more than 66 million readout channels, the sensitive area is of 1 m^2 of pixels with a unit size of 100 $\times$ 150 μm^2.
The Silicon Strip Tracker is formed of 15148 detector modules mounted on the four different subsystems: Tracker Inner Barrel and Disk (TIB/TID), Tracker Outer Barrel (TOB) and Tracker End Caps (TEC). Each is assembled on an independent mechanical light support structure. The TIB is a group of 4 layers and covers up to $|z| < 65$ cm, using silicon sensors geometry with a thickness of 320 μm and strip pitch between 80 and 120 μm. The TIB is the loser part to the interaction point and is exposed to a high dose of radiation. The TOB is a group of 6 layers with a half-length of $|z| < 110$ cm. The radiation level of TOB when compared to the TIB is lower. The geometry can be different with thicker silicon sensors of 500 μm which can be used to maintain a good signal-to-noise ratio for longer strip length and wider pitch between 120 to 180 μm. The outer endcap TEC is composed of 9 disks that are between the 120 cm and 280 cm in Z axis. The inner endcap TID is composed of 3 small disks filling the gap between the TIB and the TEC. The TEC and TID modules are organized in rings, centered on the beam line. The Silicon Strip tracker has around 9.3 millions of strips with 200 m^2 of active sensing area. It can provide a minimum of 10 measurement points in the radial projection along a particle track for pseudorapidities up to a maximum of η=2.5.
The structure for the different parts of the silicon strip tracker is made of carbon fibre in order to reduce the budget material, high mechanical strength

and low dilation coefficient. The cooling circuits have to allow the silicon strip tracker to operate with a temperature below -10 °C in order to reduce the thermal runaway and anti-annealing processes during the LHC collisions, while during the shutdown periods it should be at 0 °C.

2.5.3 The Electromagnetic Calorimeter

The CMS Electromagnetic Calorimeter [78] detector is a layer surrounding the CMS Tracker which function is to measure the energies from the electrons and photons. The ECAL consists of 76000 lead tungstate $PbWO_4$ crystals[1] with a density of 8.28 g/cm^3, a 3D view is shown in Figure 16. The detector volume is centered on the interaction point with a length 7.9 m and a 3.6 m in diameter with an approximated crystal mass of 90 tonnes. It is composed of a Barrel (EB) with a pseudorapidity range $|\eta|<1.479$ that is made of two halves, each of them divided into 18 ϕ-sectors called Supermodules housing 1700 crystals. The two Endcaps (EE) with a pseudorapidity range $1.479<|\eta|<3$ are composed of two *Dees* divided vertically, each one formed by groups of 25 crystals called Supercrystals making a total of 3675 crystals per Dee. On the front of the EE towards the interactions point the Preshower (ES) is installed with a pseudorapidity range $1.653<|\eta|<2.6$.
The crystals are tapered and distributed over the Barrel and Endcaps with the tip oriented approximately 3° away from the main interaction point, to attenuate the effect of inter-crystal gaps. The crystals will deteriorate with the radiation creating colour centres and a self-anneal, depending on the temperature and time causing a variation on the energy measurement. In order to make an accurate measurement a very precise system for monitoring the crystal transparency was installed. Two different technologies of photo-detectors have been used on the Barrel and the on the Endcaps. Avalanche Photodiodes (APDs) were used on the Barrel, specially developed by the Hamamatsu Photonics for CMS ECAL. The endcaps use Vacuum Photo-Triodes (VPTs) developed by the manufacturer RIE in St Petersburg. The ECAL detector has to work under a magnetic field of around 3.8 T, resistant to radiation and have a lifetime around 10 years and up to doses of 4 kGy and $2 \cdot 10^{13}$ n/cm^2 in the Barrel region and up to 50 times higher in the Endcaps. The Preshower detector is installed in the forward regions. Its main function is to identify two photons with a small distance between them, that are produced from the decay of the particle π in order to exclude them from single photon with high momentum measured on the ECAL crystal. The Preshower is a sandwich made of two lead absorbers and two orthogonal layers of silicon strip sensors in the configuration absorber-sensor-absorber-sensor. The ES is composed of 4300 detectors providing a total of $1.4 \cdot 10^5$ detector channels, covering an area of 16.5 m^2.

1 The lead tungstate has the properties of having a short radiation length of 0.89 cm, related to the energy loss of high energy, electromagnetic-interacting particles with it.

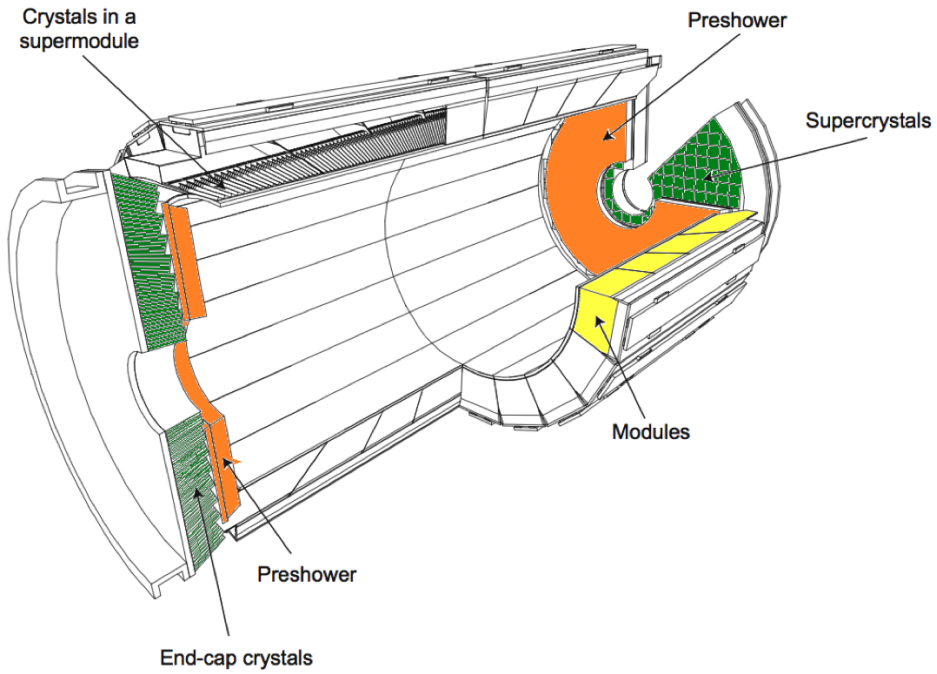

Figure 16: View of the CMS ECAL structure: Barrel (one supermodules in yellow), Endcap (in green), Preshower (in orange).

2.5.4 The Hadronic Calorimeter

The CMS Hadronic Calorimeter (HCAL) [79] was designed to measure hadrons, as protons, pions or kaons produced by the LHC collisions. A longitudinal view of a quarter of CMS is shown in Figure 17 where the location of all HCAL components are indicated. From the measurements of the hadrons it is possible to do an indirect measurement of the existence of non-interacting particles that do not leave any record when they cross the CMS detector, using as indirect measurement the imbalance momentum or a missing energy. To make this possible the hadronic calorimeter has to be hermetic. This means that it has to contain all the particle energy inside the hadronic calorimeter. In order to be the most hermetic as possible the HCAL was designed with two barrels (HB and HO), two endcaps (HE) and two forward (HF) detectors.

The hadronic calorimeter also demands a design with the adequate granularity and mass resolution. The working concept is based on a sequence of absorber and tiles of fluorescent scintillator material. The HCAL is made of around 10k individual tiles. Brass was chosen as absorber as it has short interaction length, is non-magnetic and easy to machine. In order to measure the total of the high energy particles inside of the hadron calorimeter, it is necessary to maximize the amount of absorber; this leaves few space for the scintillating tiles. The concept used was tiles with

embedded wavelength-shifting (WLS) fibers that are the optimal solution for the space available. The sensor technology used to measure the light from the fibers was hybrid photomultiplier (HPMT).

The barrel HB is built in two half and is installed between the ECAL and the magnet (1.77 m $\leq$ R $\leq$ 2.95 m). Each half barrel is made of 18 barrel wedges with 26 tonnes each, with 17 layers, the first fifteen layers of the absorber are made of brass and the last 2 are made of stainless steel for structural reinforcement. The HB has a pseudorapidity range of $0 < |\eta| < 1.4$. A barrel HO or is placed outside the magnet coil in the barrels with a few more additional layers to measure all the energy that was deposited on the HB without escaping any energy to the outside. The thickness of the scintillators in this barrel is around 10 mm. The HO has a pseudorapidity range of $0 < |\eta| < 1.3$.

The Hadronic Endcap modules (HE) are placed behind the ECAL endcap on the Muon Endcap disks. Each module has 18 wedges with 14 tonnes each, with 19 layers of absorber and with a pseudorapidity range of $1.4 < |\eta| < 3.0$. The HE has geometry with a inner radius of 0.4 m and a outer radius about 3 m with a thickness of 1.8 m. The HF calorimeter is placed on both sides of the detector at 11.1 m away from the interaction point. The HF has a pseudorapidity range of $3.0 < |\eta| < 5.0$. The materials could not be the same, used on the HB/HO and HE due to the high levels of the radiation on the region. The selected absorber on the HF calorimeter was iron. The active material used was quartz fibers embedded on the iron absorbers installed parallel to the beam pipe.

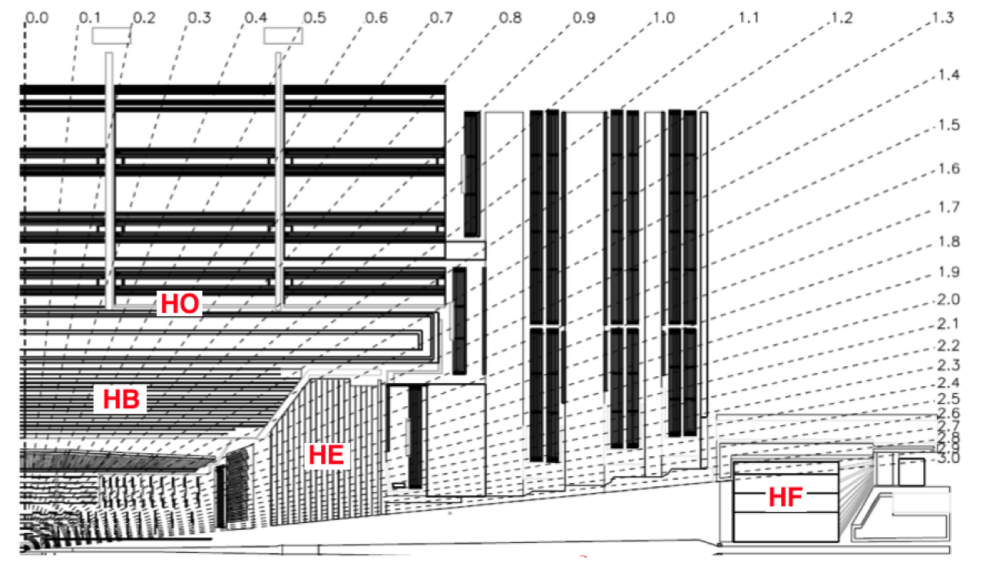

Figure 17: Longitudinal 2D view one quarter of the CMS detector with all HCAL calorimeters

2.5.5 The Muon System

As implied by the experiments middle name, the detection of muons is of central importance to CMS. Muons provide a clean experimental signature in the detectors that allows to identify signatures of interesting processes, like the "golden-plate" Higgs decays into ZZ or ZZ* then decaying into four muons, over the very high QCD background rate expected at LHC with full luminosity. Therefore a precise and robust muon measurement was a central theme from its earliest design stages.
The CMS Muon System [80] has the function of efficiently identifying muons and measuring their momenta, with a measuring range from a few GeV up to TeV and triggering. The muon detector is one of the largest ever built, having a muon position resolution in ranges between 50 and 200 μm. The area covered by the muon chambers is around 2,000 m^2 for the barrel detector and an area of 1,500 m^2 for the endcaps. The layout of the muon system is shown in Figure 18. The muon detectors were built with three different detector technologies based on gas detectors: drift tubes (DT) chambers installed on the barrels, cathode strip chambers (CSC) installed on the endcaps and the resistive plate chambers (RPC) on both barrels and endcaps. The muon system has, in total, an active detection area of 25,000 m^2 in the different layers of the chambers and nearly 1 million channels. The combination of the different technologies according to the background rates and magnetic field ensures an excellent performance of muon detection and efficient triggering in the pseudorapidity range $0 < \eta < 2.4$.
The geometry of the muon barrels (MB) detector consists of 5 cylindrical barrels with 15 m of outer diameter and 2.5 m long. Each barrel is divided into 12 sectors of 30° azimuthal angle each, and with 4 layers. They are made with rectangular DTs and RPCs parallel to the beam pipe as depicted in the schematic in Figures 18 and 19. Each muon chambers installed in the barrel wheels have 12 layers of drift tubes grouped in 3 independent units called SuperLayers (SL). The SL is made of drift cells with a spacial resolution of 250 μm, which has a rectangular shape and a maximum drift length of 2.1 cm, operating at a selected voltage that can determine 400 ns maximum drift time. The gas used on the drift tubes is a mixture of Ar(85%)+CO_2(15%).
The muon endcap (ME) regions have the chambers with the trapezoidal shape organized in series of concentric rings around the beam pipe, as shown in Figure 19b. The total ME consists of four layers on the positive and on the negative side. The distribution of the CSCs is made in three chambers rings, each ring contains 36 chambers, while the RPCs, at the moment, are installed only on the two external rings. The CSCs use the technology of the multiwire proportional chamber, having 6 anode wires separated with 7 cathode panels with milled strips on them. The strip on the cathode panels runs radially in accordance with the CMS coordinate system. The nominal voltage of operation is 3.6 kV and the gas mixture used is Ar(30%)+CO2(50%)+CH4(20%) with a gas volume of 50 m^3 with the

sensitive planes of all chambers is around 5000 m^2. The RPC chambers are used on both Endcaps and Barrels for trigger purpose. The chambers have double gaps design assembled with two Bakelite sheets of 2 mm thickness interspaced with 2 mm gas gap. In the centre of the gap a plane of readout strips is installed. The two gaps are filled with a gas mixture $C_2H_2F_4$(96.2%)+i-C_4H_{10}(3.5%)+SF_6(0.3%). The mode of operation is in avalanche mode, which can work efficiently with rates up to 10 kHz/cm^2.

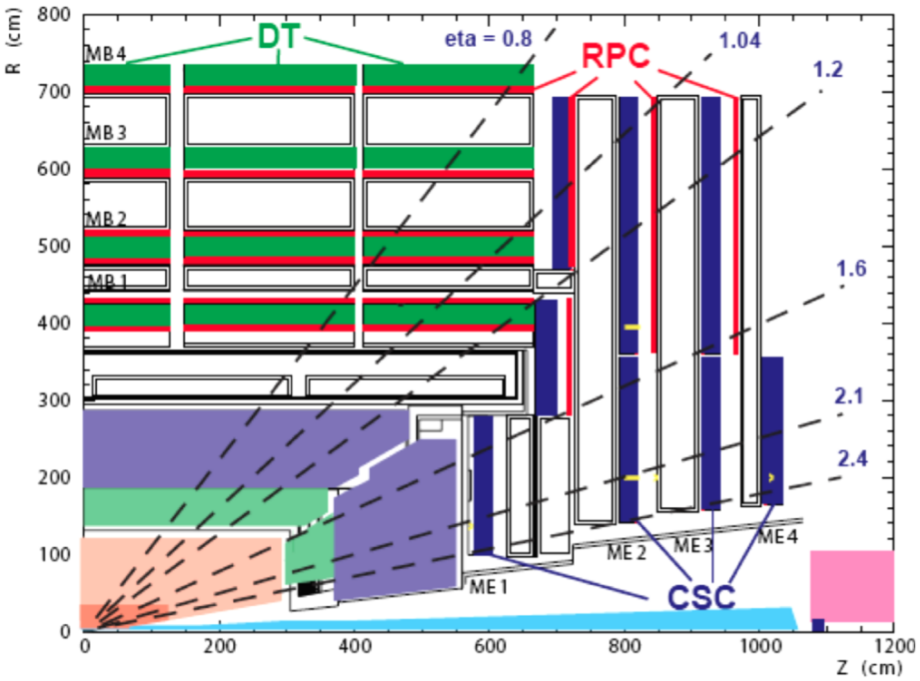

Figure 18: Longitudinal view of on quarter of the CMS detector: he various system composing the CMS muons spectrometer are shown.

2.5.6 The CASTOR calorimeter

CASTOR (Centauro And Strange Object Research) [81] is one of the two forward calorimeters of the CMS experiment. CASTOR covers a pseudorapidity range from $5.10 < \eta < 6.57$. During the LHC heavy ion collisions this pseudorapidity range is very sensitive for observation and studies of the so-called centauro and strangelet objects, which were initially observed in cosmic ray induced showers [81]. Studies of energy flow in such forward region done for proton-proton, proton-ion and ion-ion collisions are also of high interest for tuning of cosmic ray showers Monte-Carlo generators. The CASTOR calorimeter is located at 14.37 m away from the interaction point. The dimension of the detector is about 1.5 m in length and 36 cm in diameter. A sketch of the detector is shown in Figure 20. Each

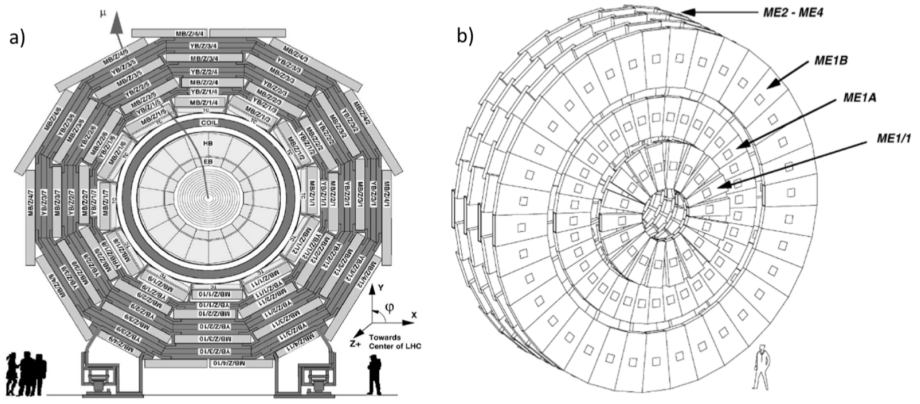

Figure 19: Transverse view of the CMS detector with an example of one muon crossing the detector (a) and Endcap Muon detector disks (b).

halves of the detector weighs around 1 tonne. CASTOR is exposed to a residual magnetic field between 0.1 T and 0.16 T with a radiation level between 2 kGy and 20 kGy. The detector is longitudinally segmented in 14 modules. The azimuthal segmentation provides 16 sectors. Each module consists of five alternating layers of tungstate and quartz glass (radiation hard fused silica). The layers are installed with an angle of 45° with respect to the beam axis to provide efficient collection of the Cerenkov light produced by the shower particles in quartz plates. Cerenkov light produced in the quartz plates during shower development are transported with air-core light-guides and to HAMAMATSU R5505 photomultiplier tubes. This type of photomultipliers can work under a magnetic field of up to 0.5 T, with the field lines doing a $\pm 45°$ angle in relation with the PMT-axis.

2.6 NEED FOR ADDITIONAL MONITORING SYSTEMS IN CMS

The CMS operation in very complex environmental conditions requires a constant monitoring of temperature, structural deformation, relative humidity, magnetic field and ionizing radiation. Indeed, all the CMS area is under constant monitoring with the main scope of having information about of the working condition of all the subsystems. The monitoring became crucial for all the equipment that are temperature dependent and/or have to work under particular thermal conditions. The monitoring system originally installed in CMS are made of traditional electronic sensors [74]. The already significant number of detectors and electrical wiring installed at the CMS, does not facilitate further installation of additional monitoring systems. Moreover,

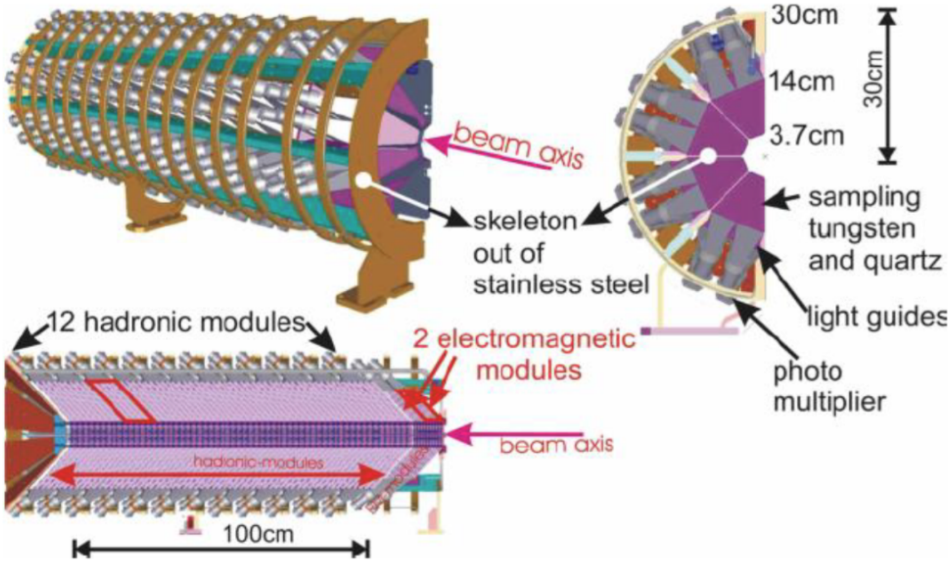

Figure 20: Sketch of the CASTOR structure.

during the operation of LHC, the high level of radiation and magnetic field is often not compatible with a good functioning of conventional electronic sensing devices. The FBG technology, unknown to the CMS community at the time of the design of the detector, represents a valuable and innovative answer to the request for additional monitoring systems to be inserted in the complex structure of the CMS detector, where cabling easiness play a key role. Indeed, the FBG technology allows the realization of wide monitoring quasi-distributed systems with an elevate number of sensing points with a single optical fiber.

2.7 FBG BASED MONITORING SYSTEM FOR CMS

Monitoring systems based on the FBGs technology were installed, by our group, in the underground site of CERN CMS experiment since 2009. They were gradually increased up to 200 temperature and strain sensors, running 24/7 for 3 years during LHC collisions, without any interference with CMS operating conditions, [82]. Since February 2013 until March 2015 the LHC has been stopped in order to allow technical interventions and upgrade of the machine and experiments, Long Shut-Down (LS1). During this period, we expanded our FBG monitoring system. Now we have nearly one thousand FBG sensors installed and operational, covering the CMS experiment from the outer to the most inner part. The central beam pipe structural monitoring system is part of the CMS-FBG monitoring system and

it is taking data, continuously, from the beginning of 2015.

2.7.1 Readout and data handling

The spectral features of the FBG sensors, allow to realize efficient spatially-distributed sensing systems on a single fiber by using the WDM technique together with a spectrally-encoded readout technique based on tunable laser source. This technique consists in interrogating a certain number of grating at the same time exploiting the spectral diversity between their selves: since a FBG reflects only a narrow portion of the incident light, by putting several gratings in series on the same fiber, the instrument will read a reflection spectrum that is composed by the central wavelengths of each grating. The attenuation of the optical fibers is sufficiently low allowing the readout system to be placed on a more comfortable place where both the magnetic field and the radiation level is low enough to be operated and maintained. Optical fibers installed on the various parts of the CMS detector are then directed to the Underground Service Cavern (USC) about 120 meters away from the sensors. The USC is a member of the twin caverns of the CMS experiment and is isolated by means of radiation hazards from the experimental one that houses the detector itself. Being radiation safe, this cavern is accessible during the LHC operations as well. The optical fibers are read out by a MicronOptics sm 225-500 optical interrogator system [71] that is equipped with an ethernet interface and can be accessed through a proprietary TCP/IP protocol. In order to reduce network traffic on the interrogator, it is connected to a mini private network created by the readout computer. This computer has another network interface installed as well, that allows the integration and sharing of the FOS system data with the CMS Detector Control System, [83]. In order to be able to be integrated into the CMS DCS, the read out software uses the Distributed Information Management (DIM) protocol [84] that is a custom protocol over TCP/IP developed at CERN. DCS system of the CMS detector is implemented in the widely used PVSS/WinCC [85] process management software language using the CERN built Joint Controls Project (JCOPS) framework [86]. In PVSS/WinCC we also developed a module that connects to the read out software via DIM and then provides the quasi standard interface required by the experiment. This module besides the relaying commands to the FOS system is responsible for the archiving the recorded data into the CMS online Oracle database. Furthermore, the read out software is also able to dump the raw data into text files to allow offline analysis. The scheme of the data management for the FOS4CMS is depicted the Figure 21.

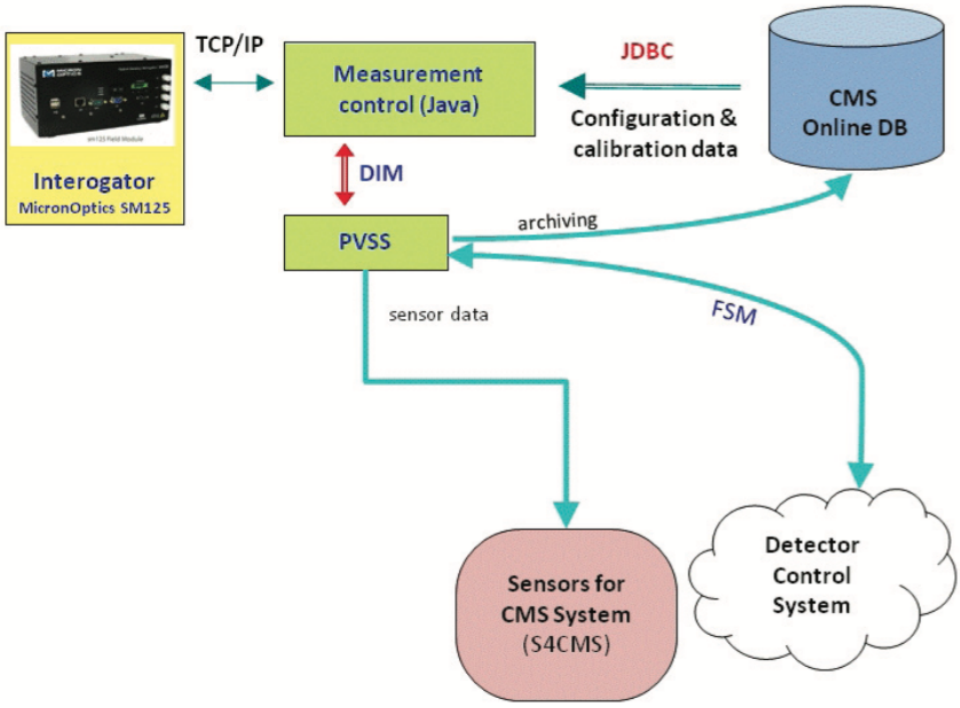

Figure 21: Integration of the FBG data taking system in the CMS Detector Control System

2.7.2 Tracker bulkhead temperature monitoring

The very first FBG monitoring system installation has covered the temperature monitoring of the two BulkHead side plus and side minus of the CMS detector. The installation took place in July 2009 and took data 24/7 until the end of 2012.

The designed monitoring system consists of 20 FBG sensors spliced in two arrays and an interrogation system for fiber optic sensors. The FBG sensor arrays were built on the basis of a standard single-mode optical fiber SMF-28. The sensors are packaged with a ceramic material and their dimension are 40 x 10 x 5 mm. On each fiber we spliced 10 FBGs, whose wavelength spacing was chosen in order to guarantee the correct peak detection. The junctions FBG-SMF28 have been made using a fusion splicer that minimizes the power loss induced from the junctions by implementing an auto-alignment facility of the fiber cores. The distance between each adjacent sensor is approximately 2m. The two arrays have been installed on the Tracker Bulk Head external surface, one on the positive and one on the negative side. In Figure 22, as an example, it is shown the layout of the system together with illustrative graphs of the data recorded by the sensors installed on the positive side, where large temperature variations can be seen. They are in complete coincidence with the Tracker power cycles. Temperature has been recorded continuously throughout the year 2011 and more detailed results are reported in [82]. The

system has been running until the end of 2012 when the Long Shutdown 1 (LS1) began.

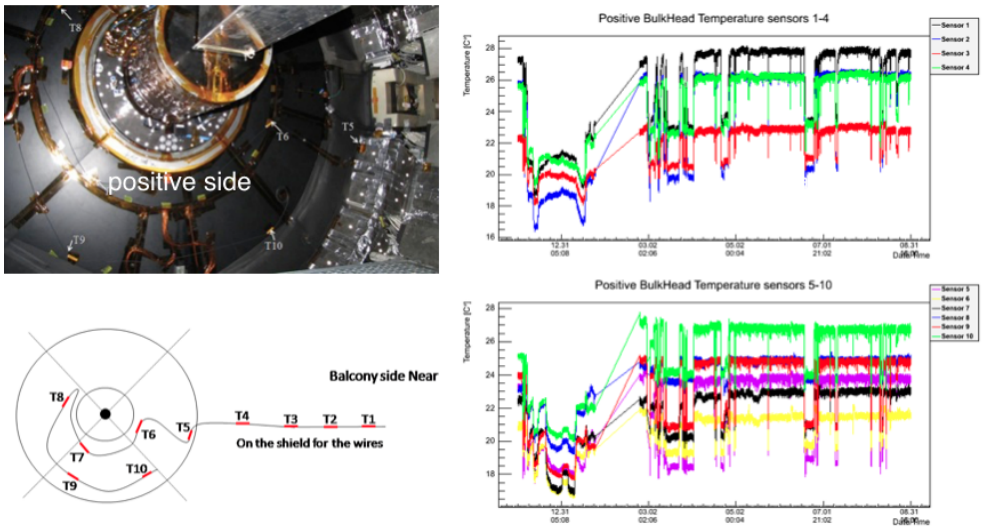

Figure 22: Layout of the Bulkhead FBG monitoring system and temperature dynamic recorded on the positive side.

2.7.3 HF raisers and CASTOR platform structural monitoring

The 3.8T CMS magnet cycles induce strain deformation on the detector structure. A strain monitoring system composed of eleven FBG sensors has been installed on the HF riser structure: ten FBG has been glued on the structure to measure the strain deformation while one has been left free to be used as thermal compensator, [82]. The strain sensors layout is shown in Figure 23(a): four sensors are on the NEAR side, two on the IP side (S1 and S6) and two on the non-IP side (S5 and S7) while six sensors are on the FAR side, three on the IP side (S8, S9 and S10) and three on the non-IP side (S2, S3 and S4).During a B-field rump up, compression of the Raiser structure is observed on the IP side , while decompression of the same structure is seen on the non-IP side, as shown from the strain dynamic versus B-field values plotted in Figure 23(b,c).

Calculations done by the CMS Integration Office showed that despite the relatively large shear displacements ($\sim$1.5 mm), the rotation centre is more or less coinciding with the internal beam pipe support therefore no destructive force is exerted on the beam pipe. Moreover, the FBGs data highlight that the raiser structure responds very similar to every magnet ramps.

The CASTOR detector has to be placed on a platform attached to the HF raiser structure. In order to ensure the safe operation of the whole structure, the strains in this platform have to be measured. A strain monitoring system composed of eleven FBG sensors has been installed on the HF platform structure: eight FBGs has been glued on the structure to measure the strain

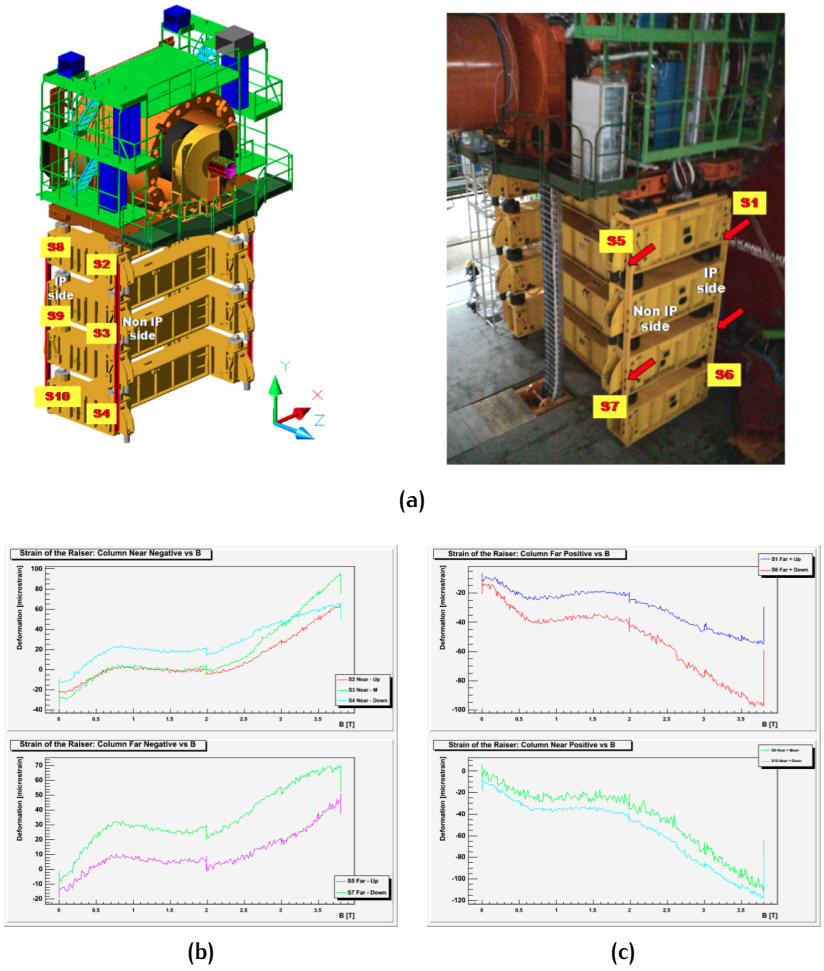

Figure 23: Layout of the FBGs monitoring system installed on the HF Riser structure (a) and strain data recorded during magnet ramp up (b) and ramp down (c).

deformation while three has been left free to be used as thermal compensators, [82]. The layout of this monitoring system is depicted in Figure 24(a).
Therefore, at first a calculation has been performed at zero magnetic field

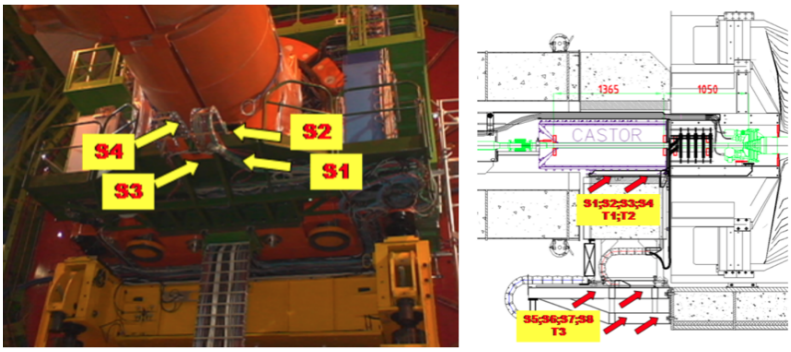

(a)

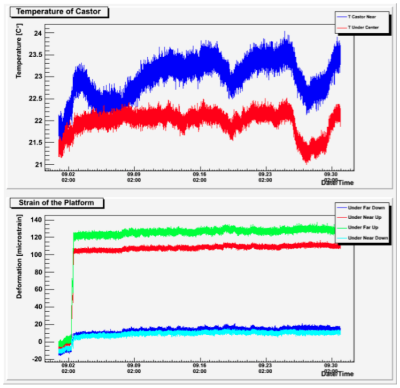

(b)

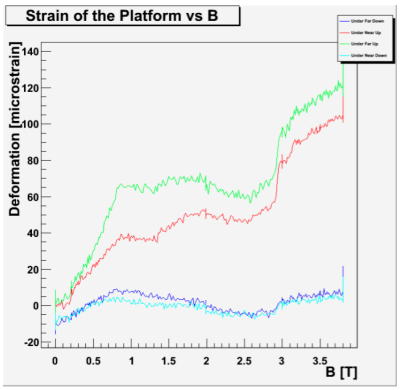

(c)

Figure 24: Layout of the FBGs monitoring system installed on the HF platform structure (a), with an example of temperature and strain dynamic during CMS operation and magnet ramps (b,c).

for the gravity-only distortion that was validated by the FBG data. Then, the FBG data recorded in high magnetic field was used to calculate the strain distribution. Calculations showed that no destructive forces are exerted in this region. An example of the strain dynamic acting on the CASTOR paltform during a magnet rump is show in the plots in Figure 24(b,c). The morphing of the entire structure, HF raisers plus Castor platform is shown in Figure **??**. These FBGs measurements represent the experimental proof of the stability oh the HF raiser structure together with the CASTOR platform. Moreover, this monitoring system has been the first FBG strain monitoring installed in CMS and in a HEP experimental facility.

2.7.4 Cavern temperature monitoring

In 2011, during LHC Run1 period, a temperature monitoring system for the whole CMS Experimental Underground Cavern (UXC) has been installed,

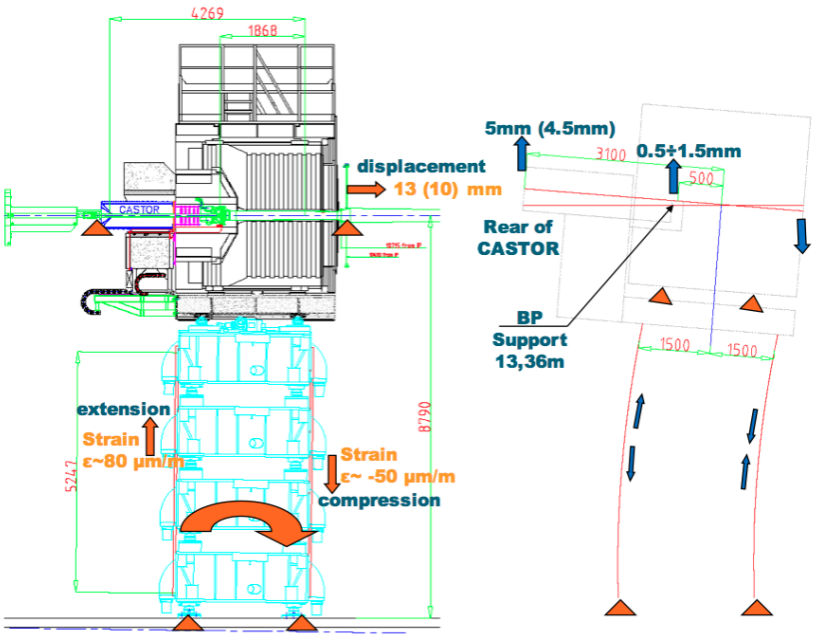

Figure 25: Morphing of the HF raiser and platform structure computed from the FBGs strain data.

[82]. It is composed by a 2 km long SMF-28 fiber with sixty FBG sensors: 23 sensors on wall near side, 3 sensors on wall +Z side, 23 sensors on wall far side, 8 sensors on shaft far side, 3 sensors on wall -Z side as shown in Figure 26. The system is up and running and the data are displayed 24/7 in the CMS control room during operation and maintenance phases. This FBG temperature sensors system allows the monitoring of the thermal gradient of the whole CMS UXC.

2.7.5 RPC Endcap temperature monitornig

The RPC Endcap muon system has been equipped with a FBG based monitoring system during LS1. On each chamber on the disks RE$\pm$2, RE$\pm$3 and RE$\pm$4 we have placed a FBG temperature sensors, that is to say 72 sensor per disk on a single fiber, for a total of 432 FBG sensors. The temperature is an essential parameter to be monitored for the correct understanding of the performaces of the RPC detector, since it enter as a correction factor in the computation of the applied high voltage which is directly related to the detector efficiency. As all the other FBG monitoring system installed in CMS, also the RPC's one is in data taking 24/7 and the temperature data are displayed in the RPC detector control station in the CMS control room. The layout of the system, as well as a picture of one RPC disk, is shown in Figure 27.

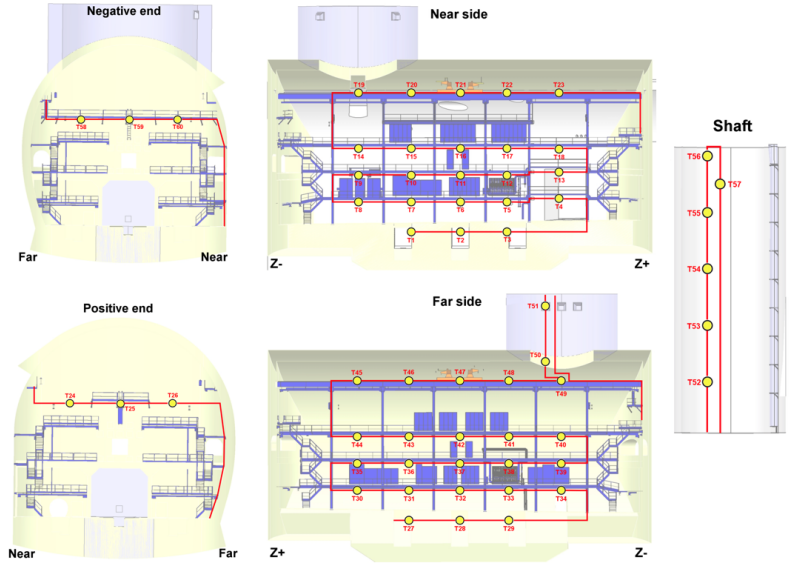

Figure 26: Layout of the CMS Experimental Underground Cavern (UXC) FBGs temperature monitoring system.

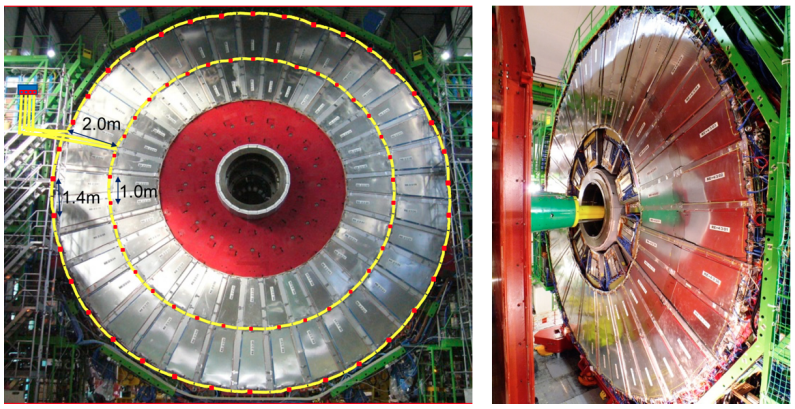

Figure 27: Layout of one of the six FBG temperature monitoring systems installed on the RPC endcap disks.

2.7.6 BRM temperature monitoring

The CMS Beam Radiation Monitoring (BRM) system is composed of 6 different subsystems that monitor the beam conditions and radiation field in and around CMS over time scales that range from bunch by bunch to long term monitoring. The remit of the BRM is to provide monitoring of the beam-induced radiation field within the UXC55 cavern and the adjacent straight sections, and to provide real-time fast diagnosis of beam conditions and initiate protection procedures in the advent of dangerous conditions for the CMS detector. During LS1 we equipped the new Pixel Luminosity Telescope[2] (PLT) and the Beam Condition Monitor[3] (BCM) Analog Opto Hybrid (AOH) boards, the PP0 and the cooling circuit with a temperature monitoring system based on the FBG sensor written in naked SMF-28 fiber, for a total of 80 FBG sensors. In particular, the AOH board temperature FBG array contains 10 gratings:

- 4 grating for measuring laser temperature;
- 1 grating for measuring ambient/radiation effects;
- 1 grating for measuring PP0 Regulator temperature;
- 1 grating for measuring cooling inlet to BCM and PLT;
- 1 grating for measuring outlet of BCM/Inlet to PLT;
- 1 grating for measuring outlet of PLT silicon/ROC section;
- 1 grating for measuring final cooling return.

In Figure 28 a photo of the AOH the FBG array installed is shown next to a view of the web CMS based detector monitoring, *cmsonline*, where the data recorded from this temperature monitoring system are available.

2.7.7 External Yoke structural monitoring

New detectors were not the only large-scale additions to CMS. The most massive change to the structure of the experiment was the addition of the new 125-tonne shielding discs, yoke endcap disc four (YE4), installed outside of the fourth endcap muon station at either end of the detector. The YE4 is part of the CMS return yoke system, which provides the path for the

2 The PLT is comprised of two arrays of eight small-angle telescopes situated on either side of the CMS interaction point. Each telescope hovers only 1 cm away from the CMS beam pipe, where it uses three planes of pixel sensors to take separate, unique measurements of luminosity.

3 The BCM of the CMS detector at the LHC is a protection device similar to the LHC Beam Loss Monitor system. The main purpose of the system is the protection of the silicon Pixel and Strip tracking detectors by inducing a beam dump, if the beam losses are too high in the CMS detector.

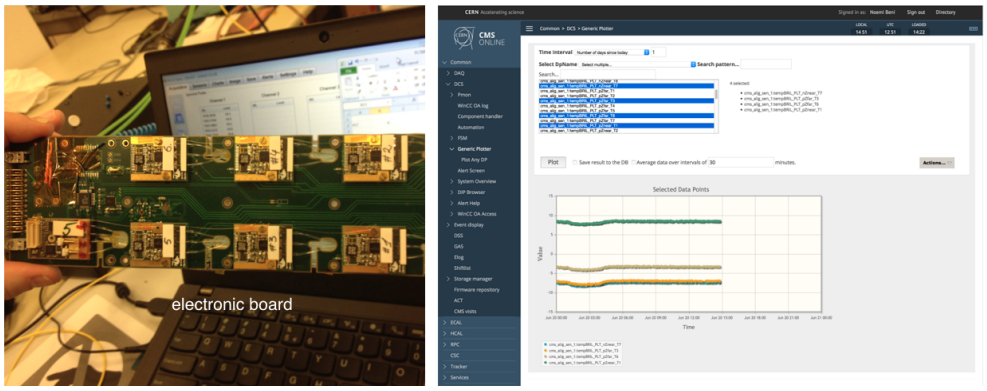

Figure 28: Example of a AOH board equipped with a temperature FBG array and view of the *cmsonline* web page where the temperature data are displayed 24/7 in realtime.

magnetic flux return in the CMS experiment. The return yoke, whose total weight is ≈ 12500 tonnes, consists of five dodecagonal three-layered barrel wheels and four endcap disks at each end comprised of steel blocks up to 620 mm thick, which also serve as absorber plates for the muon detection system. The YE4 disks, in particular, are 14 m in diameter, 125 mm thick. To monitor any magnetic field induced movement on the YE-4, at the end of LS1 we have designed and installed a FBG based strain monitoring system. The layout of the system, as well as a photo taken during the installation of the FBG arrays, is shown in Figure 29. The strain monitoring system is comprise 35 FBG sensors: 10 temperatures (left free) and 25 strains (glued on the disk surface).

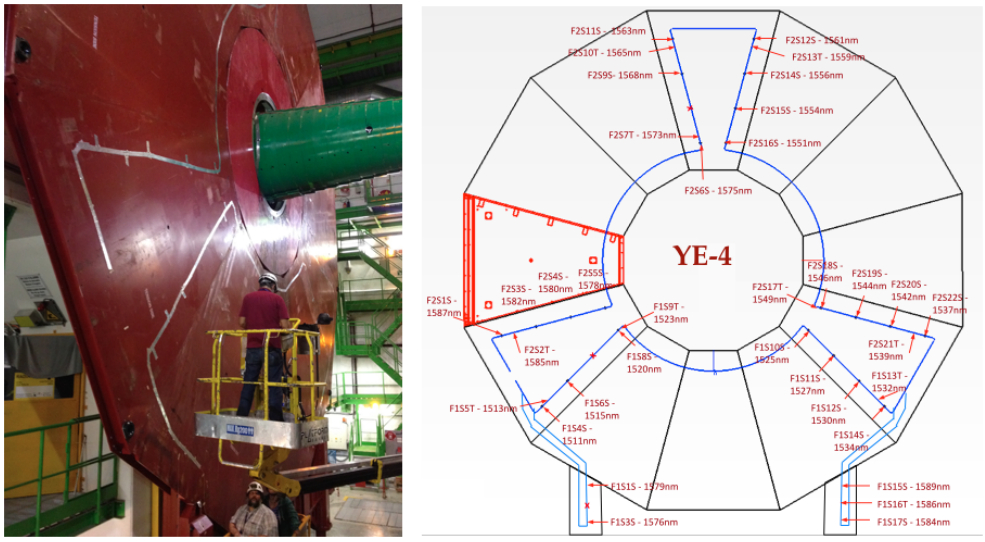

Figure 29: Layout of the strain and temperature FBG monitoring system installed on the YE4 disk.

2.7.8 Tracker RH monitoring

From 2011, our multidisciplinary research group has been involved in the development of new generation of relative humidity fiber optic-based sensors to be applied to the monitoring of the environmental parameter of the CMS Tracker detector. After a dedicated R&D phase, a full network of 72 optic fiber-based sensors, each one formed by a FBG temperature sensor and one FBG relative humidity sensor, has been installed from the end of 2013 in the critical areas of the CMS Tracker end-flange for constant distributed thermo-hygrometric monitoring [6]. The layout of this monitoring system is depicted in Figure 30.
During the LS1, the fiber optic-based sensors readings have been constantly compared with the information provided by a network of conventional non-radiation-resistant sensors and also with some punctual dew point measurements provided by a few sniffers, available on the volume. This had allowed for validation of the FBGs measurements in term of both temperature and relative humidity, in a region where the concentration of power cables and cooling pipes creates strong local gradients. After the CMS closing and even the restarting of the LHC operations in April 2015, the full network of FBG-based thermo-hygrometers installed in the experiment, has been continuously working, providing distributed monitoring of the environmental conditions in the detector, preventing from the risk of local condensation and ice formation. An example of temperatre, relative humidity and dew point reconstruction is shown in Figure 31.

2.7.9 Central beam pipe monitoring system

We designed and installed a new fibre optic sensors (FOS) structural monitoring system on the new central beam pipe of the CMS experiment to monitor on-line unpredictable mechanical deformations, [87] and [88]. The central beam pipe is a fundamental element of both, the CMS experiment and the LHC ring. It have to stand to an extreme vacuum condition (up to 10^{-13} atm) and, at the same time, it must not interfere with the particle resulting from collisions. To satisfy those conditions, in its final version, the central beam pipe is made of a gossamer Beryllium tube that need to be continuously monitored to have information about its structural and health state. Hence, is mandatory that, any monitoring system to be installed on the beam pipe must not interfere with the particle detectors that wrap around the pipe. The detailed description of the monitoring system, as well as the result coming from the analysis of the data recorded is the main subject of present Thesis work and it will be widely addressed in the next two chapter.

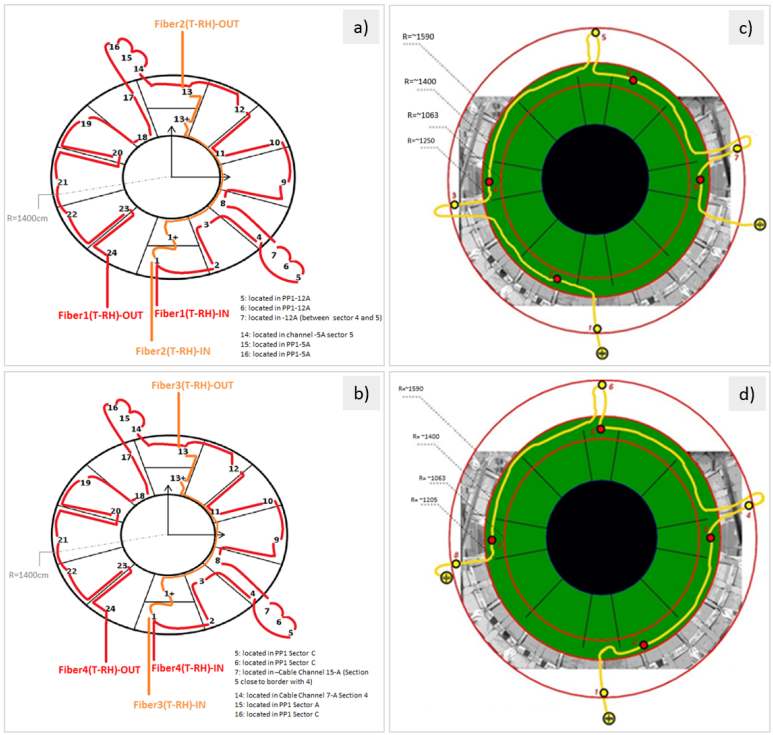

Figure 30: Schematics of the FBG-based thermo-hygrometers installed (a-b) on the inner and (c-d) outer face of the Tracker Bulkhead on both sides of the CMS experiment [6].

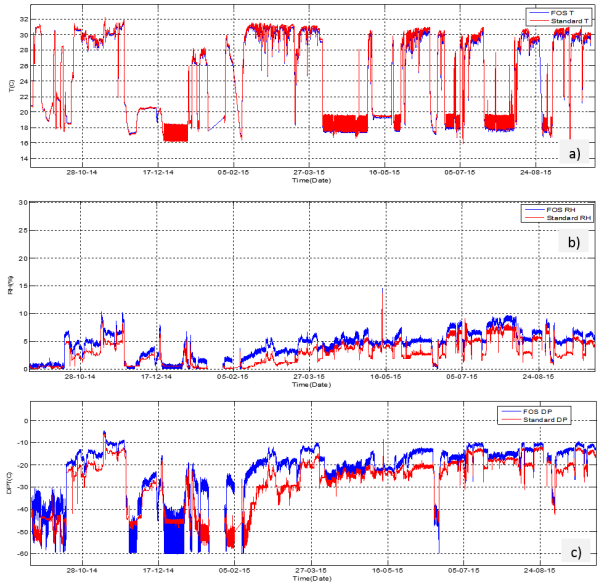

Figure 31: Temperature (a), relative humidity (b) and dew point (c) reconstruction from the FBG-based thermo-hygrometer installed in position 15 of the schematic in Figure 30. For comparison, the readings from the standard hygrometer installed in the same position are reported in red [6].

3 IPIPE PROJECT

3.1 INTRODUCTION

The central beam pipe is a fundamental element of both, the CMS experiment and the LHC ring: it is the place where the high energy proton-proton collisions take place. It have to stand to an extreme vacuum condition (up to 10^{-13} atm) and, at the same time, it must not interfere with the particle resulting from collisions. To satisfy those conditions, in its final version, the central beam pipe is made of a gossamer Beryllium tube that need to be continuously monitored to have information about its structural and health state. Hence, is mandatory that, any monitoring system to be installed on the beam pipe must not interfere with the particle detectors that wrap around the pipe. Radiation immunity represents one of the most important specification required to a monitoring system operating in a High Energy Physics (HEP) environment, while other needs are: low complexity layout, multiplexing and multi-parameters measurement capabilities.
On the basis of these technical specifications, we designed and installed a unique structural system based on Fibre Bragg Grating (FBG) sensors, that has been called iPipe monitoring system, on the new central beam pipe of the CMS experiment to monitor the thermal condition and on-line unpredictable mechanical deformations.

3.2 CMS BEAM PIPE SYSTEM

The CMS beam pipe spans over ± 18 m from the interaction point (IP) to both ends of the experimental cavern. It is segmented into a central section and 4 sections on each end. The central section is 6.2 m long and consists of a cylindrical part of 3.8 m length with conical ends. Before the Long Shutdown 1 (LS1), occurred from 2012 to 2014, the cylindrical piece had an inner diameter of 58 mm and was made out of 0.8 mm thick beryllium, while the conical parts were made out of stainless steel also 0.8 mm thick. During LS1 the central beam pipe has been replaced with a new central beam pipe, that will be described in the following sections, to cope with the requirements coming from the upgrade of the Pixel detector, [7]. The design of the CMS beam pipe system and especially the central section has been the subject of extensive studies leading to the conclusion that a cylindrical central part followed by a conical section at each end is the most favorable in terms of reducing backgrounds since it minimizes the solid angle with heavy material as seen by particles produced at the IP [89], [90], [91]. The conical section of

the former central portion of the beam pipe starts at $\pm$1.9 m and follows the η=4.9 cone, it extends into the end-cap portion of the pipe and terminates in a thin window before a flange at $\pm$10.7 m which couples it to the HF pipe. The HF pipe is almost 3 m long, also slightly conical, varying in diameter from 170 mm to 208 mm and is constructed from 1.2 mm thick stainless steel. It terminates in a thin window flange which carries 3 ion pumps and reduces the inner diameter to 58 mm, for coupling to the CASTOR-T2 (CT2) pipe. This cylindrical pipe again terminates in a flange and bellow system, which couples it to the cylindrical, stainless steel forward pipe, 2.4 m long, which terminates at the junction to the TAS absorber at 18 m. The schematic of the CMS beam pipe can be seen in Figure 32.

The main features of the CMS beam pipe system are:

- the Be central section which presents minimal material to particles emerging from the interaction point;
- the conical outer sections along lines of constant η (allowing the use of stainless steel while still minimizing background in the muon system);
- the thin reducing window at the end of the endcap pipe;
- the HF and CT2 pipes which allow forward calorimetry up to η=7, external to the return yoke;
- the placement of pumps and flanges out of the detector acceptance.

The radius and thickness of the central beryllium section are important parameters affecting the physics performance of the CMS tracking system. The impact parameter resolution and vertex resolution could be substantially improved by a re-designed pixel tracker, which has an additional fourth tracking layer within the limited space between the beam pipe and the strip tracker, ensuring also that the first measured point, given by the radius of the first layer, is as close to the beam line as possible. The support system proposed for the upgraded pixel tracker, would have allowed such a 4-layer system to be installed, but with installation tolerances so small as to pose a substantial risk. Reduced risk and better performance have been obtained reducing the beam pipe radius. This requirement had to be balanced against assuring safe and efficient operation of the accelerator and minimizing background in the experiment.

3.3 THE NEW CENTRAL BEAM PIPE

3.3.1 Design Constraints

As already pointed out, the main reason to change the beam pipe design was to allow a new Pixel detector to be mounted closer to the interaction point. This can only be achieved by reducing the outer diameter of the cylindrical

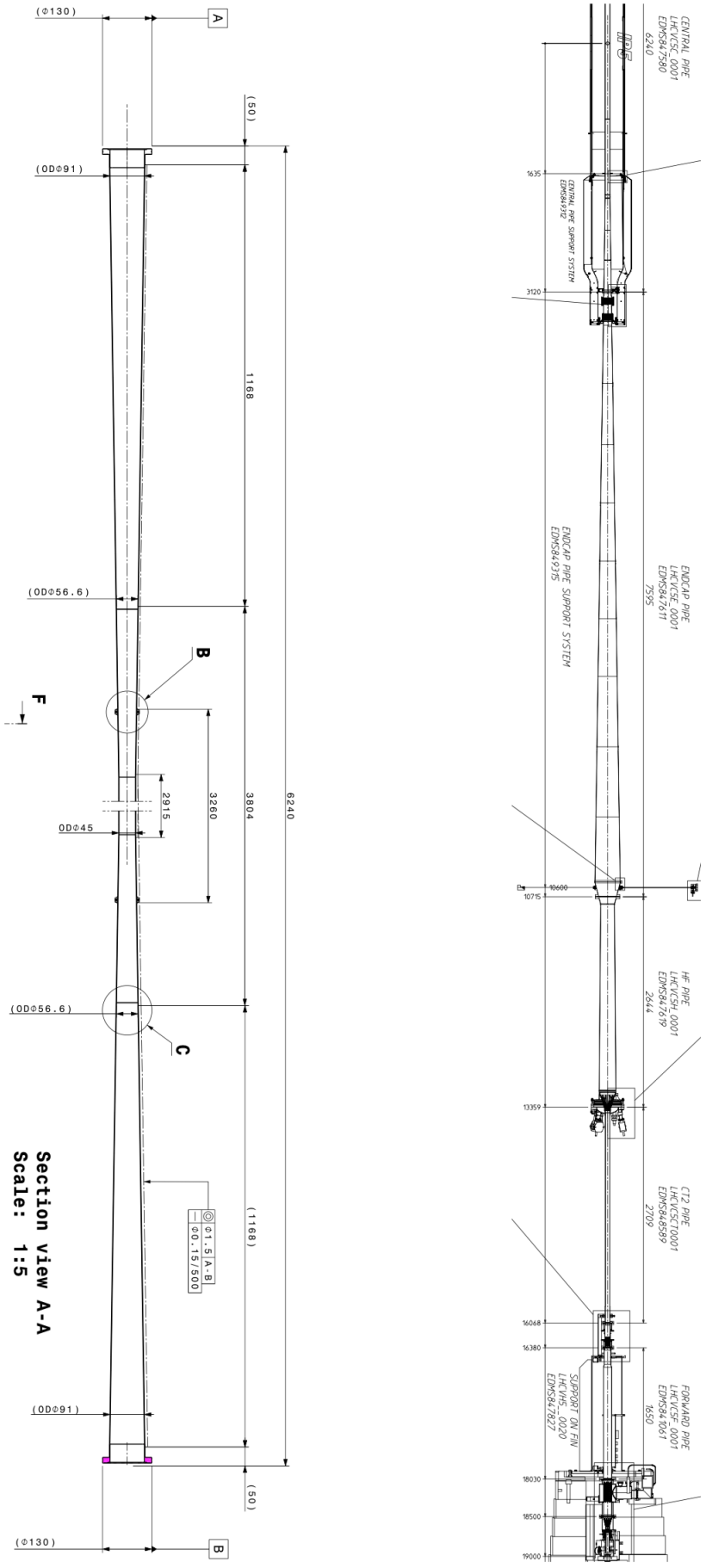

Figure 32: The right schematic shows the elements of the beam pipe system of CMS. The left one presents the final drawing of the CMS new central beam pipe.

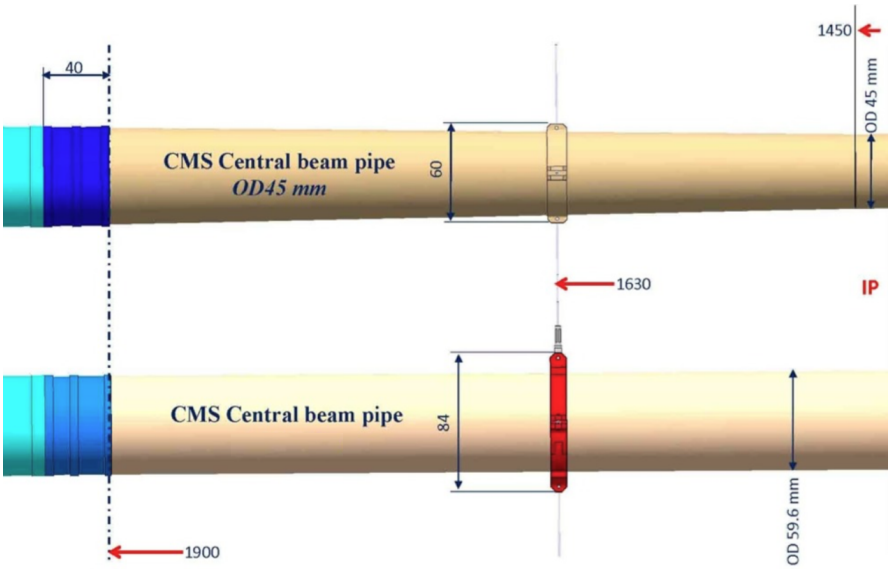

Figure 33: Sketch of the new (top) and old (bottom) beam pipe. For the new pipe notice the conical part extending to z=1450 mm in order to achieve a smaller diameter on the cylindrical part of 45 mm.

part of the beam pipe (see Figure 33). As the new Pixel detector features the innermost barrel layer at 29 mm from the beam line, taking into account mechanical tolerances and the 2 mm stay clear region for ease of installation and adjustments, the outer diameter of the cylindrical part of the beam pipe cannot exceed 45 mm. From the old central pipe design, a certain number of mechanical and physical characteristics need to be maintained:

- the overall length of 6240 mm;
- the longitudinal extension of the pure Beryllium section of the beam pipe of 3804 mm);
- the cone angle of the conical section (η=4.9);
- the support position at $\pm$ 1630 mm;

With all these constraints in mind, the new beam pipe is defined by simply extending the conical part following the η=4.9 line closer to the center until the cylindrical part can start with an outer diameter of 45 mm. The transition from conical to cylindrical now occurs at z=1457 mm from IP. As a consequence, the inner conical section already starts within the pure Beryllium part of the beam pipe and the support at z=1630 mm finds itself in the conical part. The only other parameters left free for optimization are the inner radius of the cylindrical part for a length of 2915 mm and the material to be used for the outer conical part. Consequently, a study was carried out by which the minimal inner radius of the beam pipe was determined to be 21.7 mm with a wall thickness of 0.8 mm (see following section for further details).

3.3.2 Choise of Materials

For the choice of the beam pipe material for the outer conical part, three options were investigated. The first option is to keep the material unchanged by using Stainless Steel as was done for the current beam pipe design. Secondly, two other alloys were considered, type 2219 Aluminum(93%)and Aluminum/Beryllium composite(AlBeMet®[1]). The Stainless Steel option was discarded, since this material is heavy, it gets easily activated and in addition, some of its isotopes have a rather long half-life. As a consequence, significant effort would be required to shield the Stainless Steel pipe during opening and maintenance of the detector, a feature which is not in accordance with the ALARA principle for radiation protection. Aluminum (type 2219) on the other hand, although easily activated as well, results in radioactive isotopes with short half-lives and, just after one month cool down period, the activation level drops by about a factor of three. Aluminum beam pipes are widely used in the LHC experimental areas and present very little technical risks. Finally, the AlBeMet®composite performs best in terms of activation and material density, since 62% of this alloy is made of pure Beryllium and in addition its mechanical properties are nearly as favourable as the Aluminum alloy type 2219. However, in spite of these obvious advantages, not a lot of experience exists with beam pipes built out of this material, it has never been used for LHC experimental beam pipes and in fact only short pipes have ever been built with it (at DESY). AlBeMet®is very brittle and some of its properties, such as notch sensitivity, are not very well known. Technical and schedule risks were considered higher for AlBeMet®with respect to Aluminum and it comes at a substantial higher cost. All of these facts were considered during the CMS central beam pipe Engineering Design Review (EDR held at CERN on March 5^{th} 2012) and resulted in the recommendation of using Aluminum as material of choice for the external conical part, 1.6 m support collars and end flanges.

3.3.3 Support Structure

The CMS central beam pipe is part of the CMS beam pipe, as shown in Figure 32. A view of the half cross section of the CMS experiment is shown in Figure 34 to help the reader to visualize were the beam pipe is located with respect to the CMS structure.

1 AlBeMet®is the trade name of the Materion Brush Beryllium & Composites (formerly known as Brush Wellman) company for a beryllium and aluminum composite material derived by a powder metallurgy process. This powder metallurgical product is produced by gas atomization available as rod, bar, tube and sheet. These shapes are derived by consolidating the Al/Be powder by hot isostatic pressing (HIP) and cold isostatic pressing (CIP) followed by extrusion. The extruded bar is fabricated by CIPing the isotropic spherical Al/Be powder into semi-dense billets and then canning the billet for subsequent extrusion with a minimum of 4:1 reduction ratio

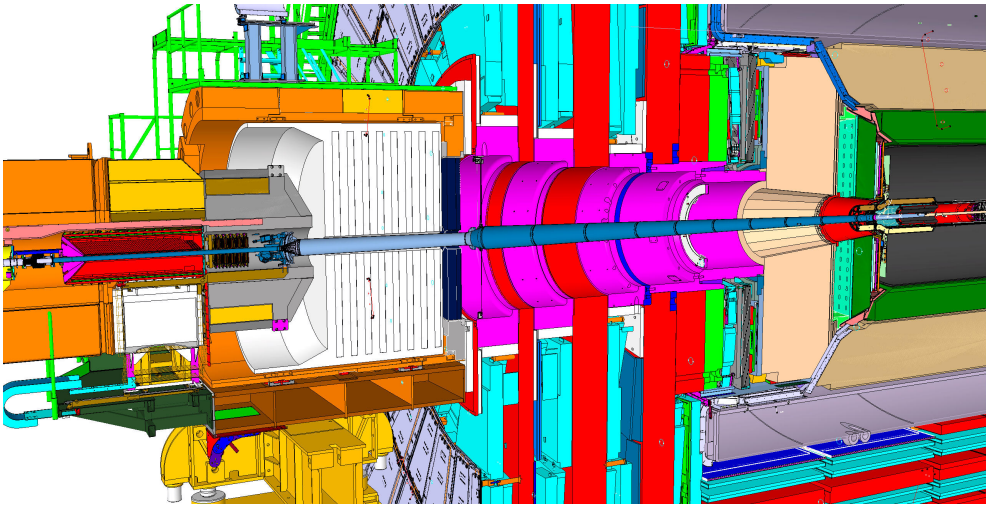

Figure 34: Technical drawing of the half cross section of the CMS detector.

The central beam pipe is attached to the Tracker structure by means of a pair of 4 stainless steel wires (two vertical and two horizontal). The attachment points are located 1.6 mm away from the interaction point, resulting in a span of 3.2 m. The technical 3D view of this support inside the Tracker volume is shown in Figure 35(a). The new beam pipe design made the need redesign also these supports, moving away from Stainless Steel clamps to Aluminum in order to significantly reduce the amount of material. The redesign have been done taking into account not only the primary function of supporting the beam pipe without introducing stress to the structure, but also the need to maximize clearances to the Barrel and Forward detectors during the insertion and removal processes.

Between the central beam pipe and the subsequent endcap beam pipe there is, on both side, a double bellow in order to reduce any mechanical interaction between the two sectors and to secure the stability of the central beam pipe. A permanent support for the central beam pipe and bellows is attached to the tracker bulkhead. The above described support, called tracker support, is shown in Figure 35(b). It consists of three separate supports:

- a x-y support for the central pipe at z = 1.6 m through wires engaged into pulleys and attached to the nose, also called *fishing rod*, structure for tensioning and regulation, shown in Figure **??**a;
- a x-y support for the central pipe at z = 3.1 m through a system of sticks and carriages integrated into the nose structure;
- a x-y-z support for the endcap pipe at z = 3.5 m through a system of sticks integrated into the nose structure.

The z = 3.1m support holds the central pipe at the connection flange to the endcap pipe just before the double bellow section, visible in Figure 35(b),

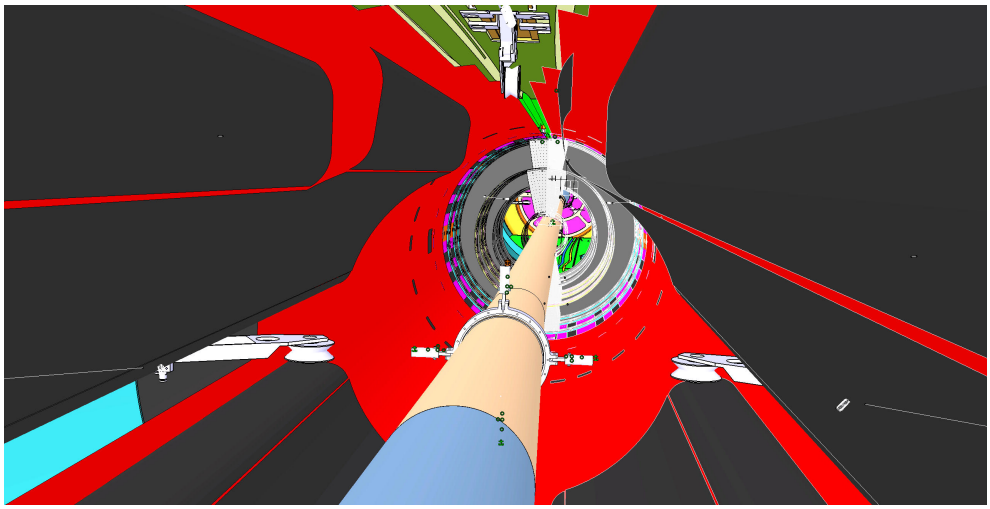

(a)

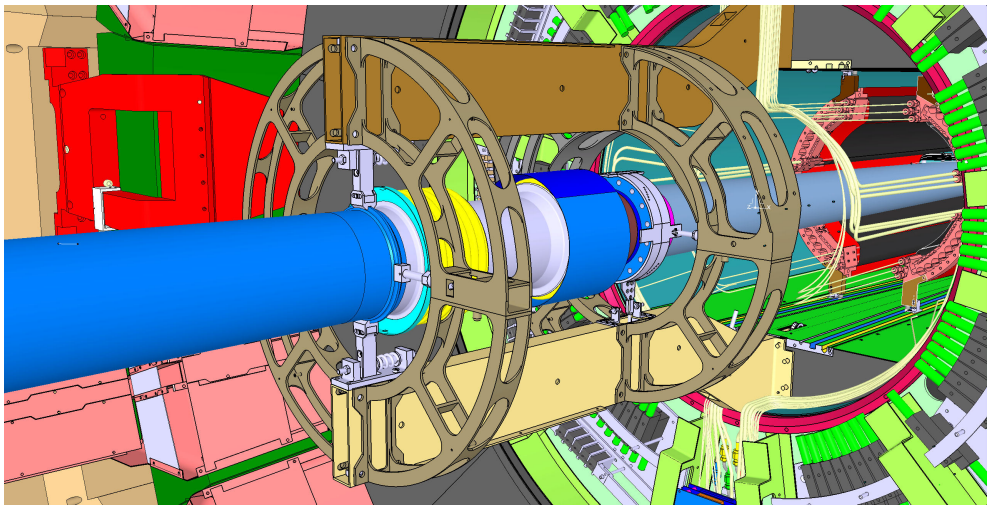

(b)

Figure 35: Technical drawing of the x-y support for the central pipe for tensioning and regulation at z = 1.6 m in (a), and of the tracker supports at z = 3.1 m and z = 3.5 m (b).

while the z = 3.5m support holds the endcap pipe through a full translation-constrained point. The tracker supports are configurable for various operations. In particular:

- the x supports will be removed during pixel detector insertion and bakeout jacket insertion and removal,
- the z support at 3.5 m will be removed during bakeout to allow for thermal expansion. A temporary support will be used instead.

Between the endcap beam pipe and the HF beam pipe, inside YE3 at z = 10.7m, there is another permanent support: it hangs from above and is stabilized from sides and bottom. The top hanger has x, y and z adjustment. Finally, at z = 13m, there is a support installed in the base for the CASTOR, between the HF and the CT2 sector of the beam pipe. It is a lever mechanism used to reduce the deflection of the beam pipe. It will be activated from below when the two halves of the base are closed below the beam pipe. The HF and the CASTOR support are shown in Figure 36.

The above described permanent support are in place when the CMS detector is closed in its operational configuration. During maintenance phases the permanent supports are integrated or, depending on the specific maintenance case, substituted by temporary supports, that will not be described in this work. A detailed description of all the permanent and temporary supports of the CMS beam pipe can be found in [92].

3.3.4 Tolerances and Aperture

The required beam aperture determines the theoretically minimum inner diameter for any new beam pipe. During injection the beam occupies the largest aperture in the vertical plane and in case of an asynchronous beam dump the beam is largest in the horizontal plane. The dimension of the beam pipe must be chosen such that, taking into account all possible mechanical tolerances of the beam pipe, all installation tolerances and all possible movements of the pipe during operation, the wall of the pipe can never approach the beam closer than the limiting distance required by the beam aperture. As a prudent precaution for the safety of the detector, no element of the beam-pipe within it should have a smaller aperture than the closest machine element to the interaction region, which in the CMS case is the TAS absorber, situated at 18 m and having an inner radius of 18 mm.
During the design of the LHC experimental beam pipes, conservative aperture estimates lead to the request for a stay-clear cylinder of 14 mm radius around the nominal beam line close to the interaction point. The following mechanical factors have been considered to contribute to limiting the practicably achievable minimum inner pipe radius, such that the stay-clear cylinder is always contained within the physical pipe:

- construction tolerances causing the pipe radius to be less than nominal;

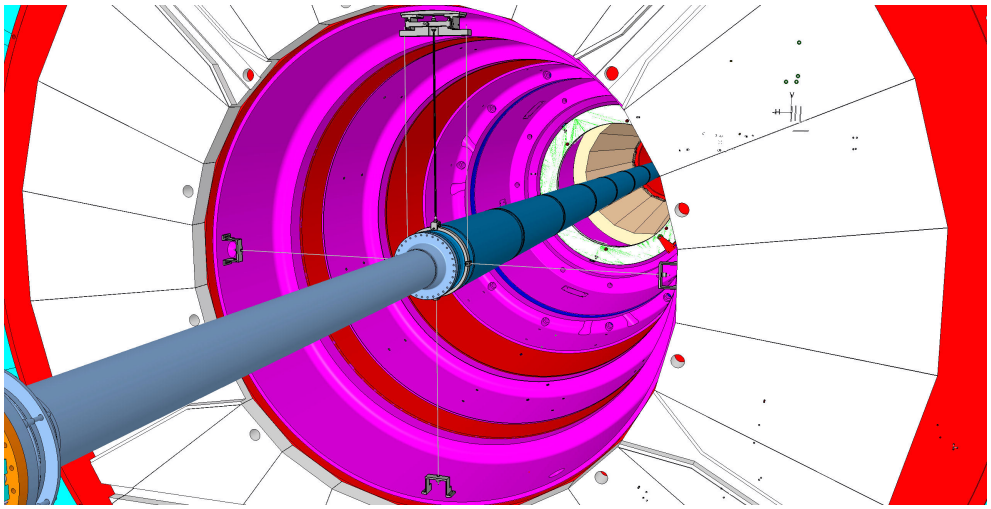

(a)

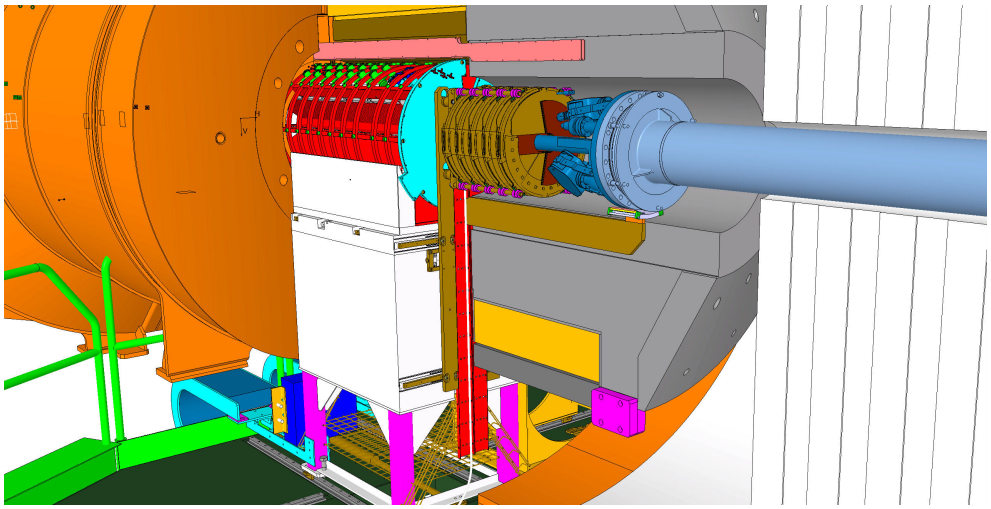

(b)

Figure 36: Technical drawing of the HF permanent support located at Z = 10.7 m with respect to the impact point (a). Drawing of the CASTOR permanent support located at Z = 13 m

- mechanical sagging of the pipe between supports;
- the precision with which the pipe can be surveyed into place;
- time-dependent movements of the beam pipe supports (attached through the Tracker, Tracker support and barrel Hadron Calorimeter to the central yoke wheel). These may be caused by displacements of the whole cavern with respect to the plane of the LHC machine, settling or flattening of the central yoke wheel, or distortions due to the magnetic field.

To significantly lower the limit on the minimum diameter of the cylindrical portion of the new central beam pipe, with respect to the old central beam pipe, significant improvements in minimizing the uncertainty of the beam pipe envelope with respect to the ideal beam line have been achieved.
New aperture calculations were made by machine experts in order to establish whether the smaller diameter central beam pipe section would still be compatible with safe and stable beam operation for various machine optics and energies. Relevant inputs to the aperture calculations are:

- The final value of 6.05 mm as the linear sum of the tolerances for the position of the beam pipe with respect to the ideal beam line.
- Stay clear region of 14.00 mm around the beam. This quantity is to be added to the 6.05 mm linear sum of the tolerances.
- New beam pipe radius in the central cylindrical section is assumed to be 21.7 mm.
- Closed orbit tolerance of 4 mm at nominal injection energy and optics (170 μrad crossing angle, 2 mm beams separation and 3.75 μm nominal normalized transverse emittance)
- Beta-beating of 20%.

The output of the aperture calculation is a quantity called *n1* defined as the largest setting in sigma ($\sigma_{x,y}$ is the rms beam size) of primary collimators such that the local aperture is protected from secondary halo [93]. Taking into account also operational margins, the primary aperture of the LHC needs to stay at n1>7.0. This value of n1 is the criterion for the geometrical acceptance for all elements in the ring. From the calculations, the n1(σ) value for the new beam pipe is 19.8 during the Injecton phase (450 GeV) and 454 at Flat Top phase (7 TeV).

3.3.5 Machine Induced Background

Extensive studies were made on the impact of machine induced background events in CMS. One important aspect of the new beam pipe is the measure of its impact on the machine induced background events showering the central

portion of the detector.
Machine Induced Background events (MIB) were simulated in the LHC detectors focusing on two main sources: tertiary beam halo and beam-gas interactions. It is found that background rates in detector subsystems strongly depend on the origin of MIB, particle energy and type. Using this source term, instantaneous and integrated loads on the detectors and impact on the detector performance can be further derived. The latter was done for CMS using both GEANT4 [94], and FLUKA [95] simulation codes. Material and shape of the central section of the pipe have an impact on how the MIB events are seen by the CMS detectors close to the beam line (mainly Pixel, inner portion of the silicon strip tracker, HF, BCM1 and PLT). Of relevance for CMS in this context are mostly beam-gas events interacting with the beam-pipe and beam- pipe elements in the proximity of the interaction region, hence superimposing to the innermost detectors showering particles to the normal p-p interaction products originated from the IP. Especially for the Pixel, these extra particles, being almost parallel to the silicon modules, may leave a large number of hits and, if the event is triggered at L1, causing at present sizeable dead-time for the experiment (long time to readout and clear). Figure 37 shows the interaction map for events which primary beam-gas interaction occurred along LSS5. As can be seen from the colored density map, the beam pipe material is a source of many of these interactions and in particular the region where from conical it becomes cylindrical at around 2 m from the IP which scores the highest density in the map.
The shape and mostly the material in the conical section of the of the beam pipe plays a major role in determining the amount of showering particles from beam-gas interactions which eventually make their way in the inner region of the CMS detector.
Results show that while hadron and neutron densities are not affected too much by the change in beam pipe layout and material, the electron density, which by far dominates the overall background, does (Figure 38). This is explained by reduced electromagnetic showers in the conical part of the beam pipe due to lighter material.

3.4 MECHANICAL ANALYSIS OF THE NEW CENTRAL BEAM PIPE

The static and dynamic (modal) analyses of the design for the new central beam pipe of the CMS experiment have been made in a dedicated study within the CERN EP-CMX-EI section and have been presented in an internal calculation note [96]. In this section the results achieved will be summarized. The geometry proposed for the new CMS central beam pipe is shown in Figure 39 consists of:

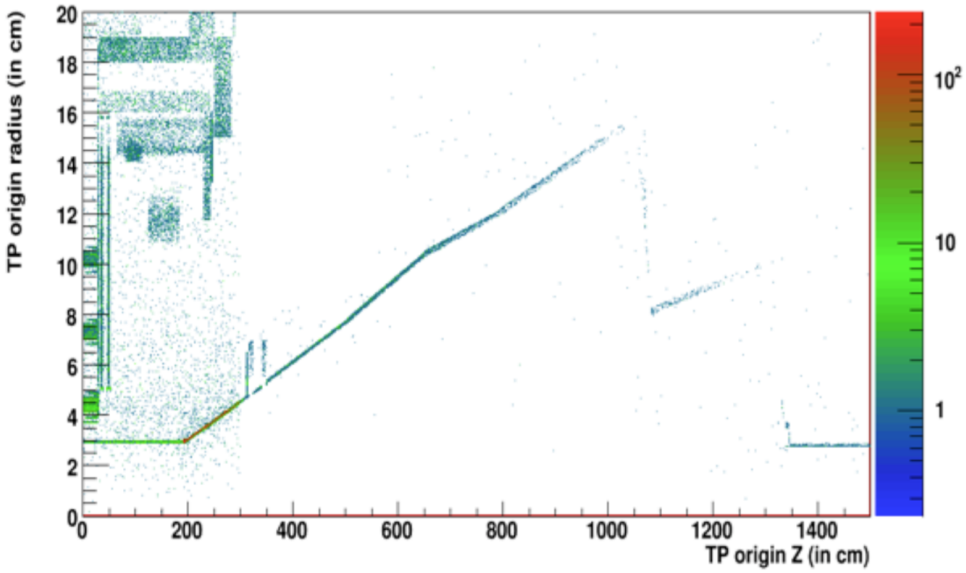

Figure 37: GEANT4 simulation of hit density in proximity of CMS for events where primary beam-gas interaction occurred along LSS5. As expected, the highest values are found at the end of the conical section of the pipe between 200 mm and 250 mm from IP5 [7].

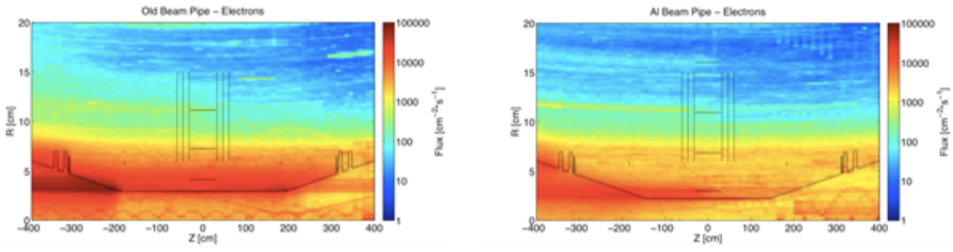

Figure 38: Fluka simulation of the hit density for electrons emerging from the interaction of primary beam-gas events (entering from the right) with detector material for the old beam pipe (left) and the new aluminum beam pipe (right) [7].

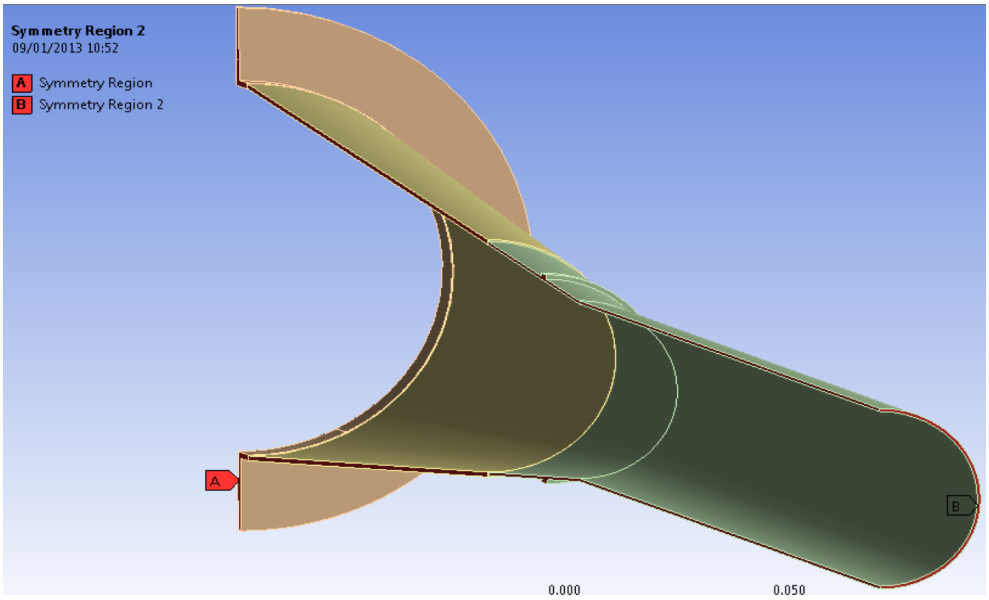

Figure 39: Technical drawing of half section of one side of the CMS central beam pipe. The change from cylindrical to conical shape is highlighted as well as the change from beryllium to aluminum.

- a central Beryllium pipe with a cylindrical shape of length equal to 2915 mm, centered about the interaction point (I.P.), an outer diameter of 45 mm and a thickness of 0.8 mm;
- a conical Beryllium pipe at each end of the central cylindrical pipe with a length of 444.5 mm, a half angle of 0.853 degrees and a thickness of 0.8 mm;
- a conical Aluminium 2219 pipe at each end of the conical beryllium pipe with a length of 1196 mm, a half angle of 0.853 degrees and a thickness of 0.8 mm.

As already explained in previous sections, the CMS central beam pipe is supported by two collars (Figure 35) positioned symmetrically with respect to the IP and distanced of 3260 mm and two end flanges. The total length of the central beam pipe, including the two end flanges, is 6240 mm.
The mechanical analysis has been carried out in the two main scenario foreseen for the central beam pipe: gravity plus vacuum and gravity plus vacuum plus temperature. To simulate these scenario specific loading conditions have been considered taking into account the physical constrains of the structure. In particular, the supports at Z= $\pm$ 1.6 m (Figure 35a), which consist of two collars placed around the conical portion of the pipe with each being attached to four prestressed radial wires, has been modeled taking into account influence of the wires in the collars' displacements: due to the relatively high stiffness of the wires in their longitudinal direction, all anchor points? degrees of freedom were considered unconstrained with the

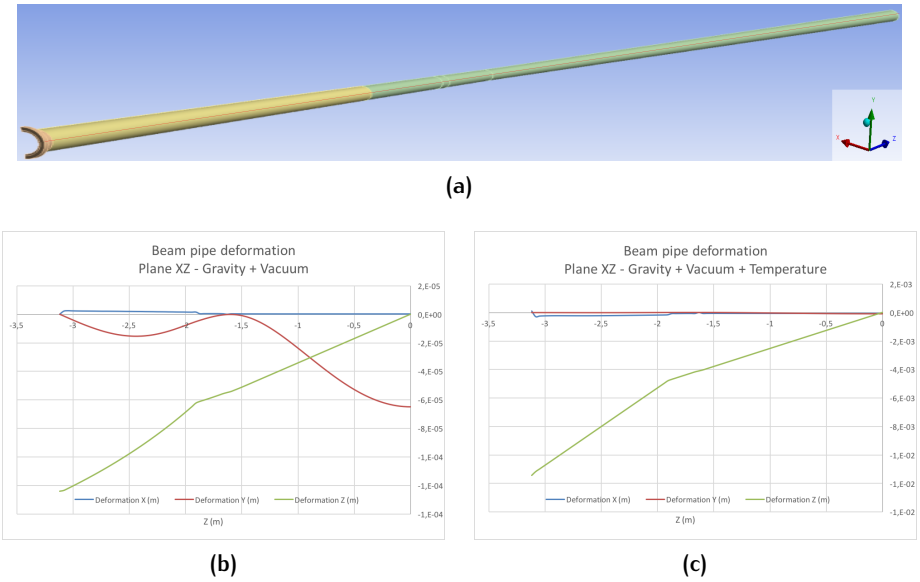

Figure 40: Mechanical simulation of the CMS central beam pipe structure (a) under nominal working load condition (b), *i.e.* gravity plus vacuum, and during bakeout operation (c), *i.e.* gravity plus vacuum plus temperature up to 250°C.

exception of the one corresponding to the translation in the longitudinal direction of the respective wire. Concerning the end flanges at Z=±3105mm (Figure 35b), all degrees of freedom were constrained with the exception of the translation degree of freedom in the beam pipe?s axial direction in order to not restrict the axial movement of the beam pipe. Finally, the presence of the double bellow has been accounted introducing a spring with longitudinal stiffness of 109 N/mm (according manufacturer data).
The results of the simulations in the above mentioned cases are illustrated in Figure 40. In normal operating conditions, *i.e.* vacuum plus gravity, the deformation along X direction is negligible while the maximum longitudinal deformation is -0.12 mm. In the bakeout scenario, *i.e.* vacuum plus gravity plus temperature up to 250°C, the deformations along X ad Y directions are negligible while the maximum longitudinal deformation is -11.4 mm.
These results gave a clear input to the design of the fiber optic sensors monitoring system to be installed on the central beam pipe.

3.5 THE IPIPE MONITORING SYSTEM

3.5.1 Design and layout

The iPipe monitoring system consists of four naked glass SMF-28 fibers (200 μm diameter: core-cladding-buffer) placed along the cardinal longitudinal positions on beam pipe cross section. 16 FBG sensors have been manufacted

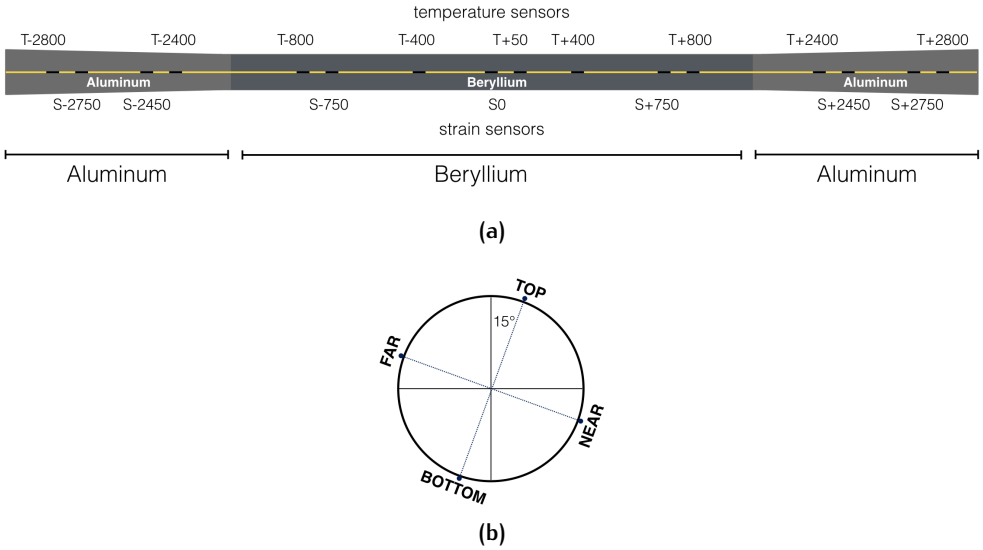

Figure 41: Longitudinal (a) and transverse (b) layout of the fibre optic monitoring system installed on the CMS central beam pipe. The quotes in (a) refer to the distance of the temperature and strain sensors with respect to the center of the pipe.

on each fibre, 7 of them are solidarly glued on the pipe to measure the local strain and the remaining 9 are left unglued but in contact with beam pipe in order to work as local thermometers and as strain temperature compensators for the adjacent strain sensors. A schematic representation of the FBG distribution around the beam pipe is depicted in Figure 41, while in Table 1 are reported the central wavelengths of each sensors as measured at room temperature after the installation of the arrays on the pipe was completed. In Figure 41a, the quotes indicate the positions, relative to the center of the central beam pipe of the FBG sensors. All the quote refer to the FBG sensors of a single fibre: the ones reported behind the drawing of the pipe are related to the strain FBGs, while the ones above are related to the temperature FBGs. As shown in Figure 41b, 4 FBGs array are installed on the central beam pipe tilted of 15° with respect to the cardinal position to cope with the installation of the 4 layer Pixel detector, that will happen in March 2017.
The system has been designed to stand the high radiation dose in this region during LHC operation and to survive the bakeout treatment of beam pipe at high temperature (up to 220°C), necessary to remove unwanted polluting particles from the inner surfaces of the beam pipe.

3.5.2 Preliminary studies on the glue

The new CMS central beam pipe, widely described in the previous sections, is made of 6 m length of beryllium tube with aluminium 2219 alloy at each

FBG type	Z coord [mm]	Array1 λ_B [nm]	Array2 λ_B [nm]	Array3 λ_B [nm]	Array4 λ_B [nm]
Temp	-2800	1511.819	1512.076	1512.155	1512.030
Strain	-2750	1517.049	1516.868	1516.887	1517.207
Strain	-2450	1522.058	1521.911	1521.668	1522.094
Temp	-2400	1527.301	1527.339	1526.631	1527.356
Temp	-800	1532.182	1532.347	1532.510	1532.416
Strain	-750	1537.224	1537.348	1537.915	1537.621
Temp	-400	1542.197	1542.496	1542.307	1542.311
Strain	0 [IP]	1547.281	1547.412	1547.391	1547.398
Temp	+50	1552.202	1552.421	1552.484	1552.620
Temp	+400	1556.984	1557.459	1557.011	1557.166
Strain	+750	1562.037	1562.320	1562.360	1562.500
Temp	+800	1567.295	1567.501	1567.306	1567.429
Temp	+2400	1572.075	1572.098	1571.986	1572.228
Strain	+2450	1576.897	1577.120	1577.115	1577.103
Strain	+2750	1582.168	1581.936	1581.751	1582.162
Temp	+2800	1587.174	1586.887	1586.696	1587.040

Table 1: Layout of the FBG array installed on the CMS central beam pipe as measured after the gluing procedure at RT in a surface laboratory at CERN.

extremity. Of critical importance has been to find glues which can fulfill the required condition of curing at room temperature, having low viscosity, being radiation resistance, without damaging the beam pipe materials in an irradiated area. Since keeping the beam pipe absolutely unaffected by the encapsulant is of highest importance, it was decided to study the interaction of the Stycast 2850 FT Catalyst 24 LV with Be and Al 2219 in various and representative conditions of use of CMS cavern to minimize any risk of damaging the beam pipe. The study focused on the effect of heat treatments due to bake out and on irradiation and is widely described in [97]. The samples investigated consist in 1 cm x 1 cm plates of Al 2219 and S-200-F beryllium alloy. No passivation treatment was applied to Be plates, while in the real conditions a passivation treatment is carried out which removes any possible machining contamination and enhances de protection of Be by passivation. From this point of view, the conditions of the test are more severe than in the real situation.[2]

3.5.2.1 *Gluing steps*

Preparation of the surface, gluing step and heat treatments were carried out by CERN specialized technician from the TE-MSC-MDT section. Metallic plates were cleaned with ethanol and carefully dried. On each plate, two drops of Stycast 2850 FT Catalyst 24 LV were deposited, one containing optical fiber and one without. The 24h curing was carried out at room temperature. Five plates of each material (Al 2219, Be) were prepared.

3.5.2.2 *Heat treatments and irradiation*

Three heat treatments were set up:

- room temperature for one week, 50% humidity (called RT in the following),
- 100°C for one week, 50% humidity in order to activate any diffusion process, (called 100°C in the following). Samples were deposited in closed jars in order to keep the humidity level during the 100°C heat treatment.
- 3 times 280°C for 2 days in order to simulate a severe bakeout (called BKO in the following).

The samples, 2 plates for each material, were placed in hermetically closed jars and introduced in oven for the heat treatments.
Part of the samples was also sent to IONISOS (France) for gamma irradiation up to a dose level of 200 kGy, to partially simulate the real environment,

2 Taking into account the specific hazards of Be, safety rules were discussed with Occupational Health & Safety and Environmental Protection Unit of CERN (J. Gulley). Thus, experimental work was guided by procedures submitted to OH&SEE unit prior to observation.

in term of ionizing radiation, that will be present in the beam pipe volume during the LHC collisions.
After heat treatments and irradiation, the samples were sent externally for cutting and polishing. The Be samples were sent to EXOTEC PRECISION (Lisieux Way, Taunton TA1 2JZ, UK), while Al 2219 were sent to METLAB Oy (Nuutisarankatu 15, 3900 Tampere, FI). The Al 2219 samples were mounted in a conductive resin, cut and polished while the Be samples were cut and polished directly without being mounted in a resin.

3.5.2.3 *Microscopic observations*

The microscopic observations took place in two stages. First, were carried out observations of the surface of gluing, called later on "from the top". Then, samples were cut and polished, and the cross-section was observed. The observations were carried out on three microscopes:

- Optical stereomicroscope M205C (Leica)
- Optical microscope Axio image M2m(Zeiss)
- SEM Sigma (Zeiss) equipped with Oxford 50 mm^2 X Max EDS (Energy-Dispersive X-ray Spectroscopy) detector

For the Al 2219 samples no great, nor generalised interaction was observed. However, Stycast of the Al 2219-BKO samples present cracks on the edge of the droplet but seems to remain adherent to the substrate. Nevertheless, no evident sign of corrosion was found. In Figure 42 SEM images from the top and of the cross-section are shown.
Concerning the beryllium, as first observation it has to be noticed that the Be samples show porosity. However, since this material is manufactured by powder metallurgy, presence of porosity is expected and unavoidable. Moreover, the preparation of the cross-surface induced damage of the surface, which complicates the interpretation of the results on the interface surface. No great, nor generalized interaction was detected on the Be samples and no marks of corrosion were identified. The Figure 43 present examples of the interface surface for different samples of Be, under the droplet of Stycast and out of it: the different samples do not show any significant difference in terms of roughness.
Finally, the mechanical properties and adherence of the Stycast, after all treatments was qualitatively checked by pulling on the optical fiber. In all cases, the fiber broke but the Stycast remained complete and adherent.

3.5.3 The Installation

We installed the sensors on beam pipe in May 2014 in one of the surface laboratories at CERN Meyrin site. The gluing was a very delicate phase of the entire project, demanding several trials on metal samples and tests of

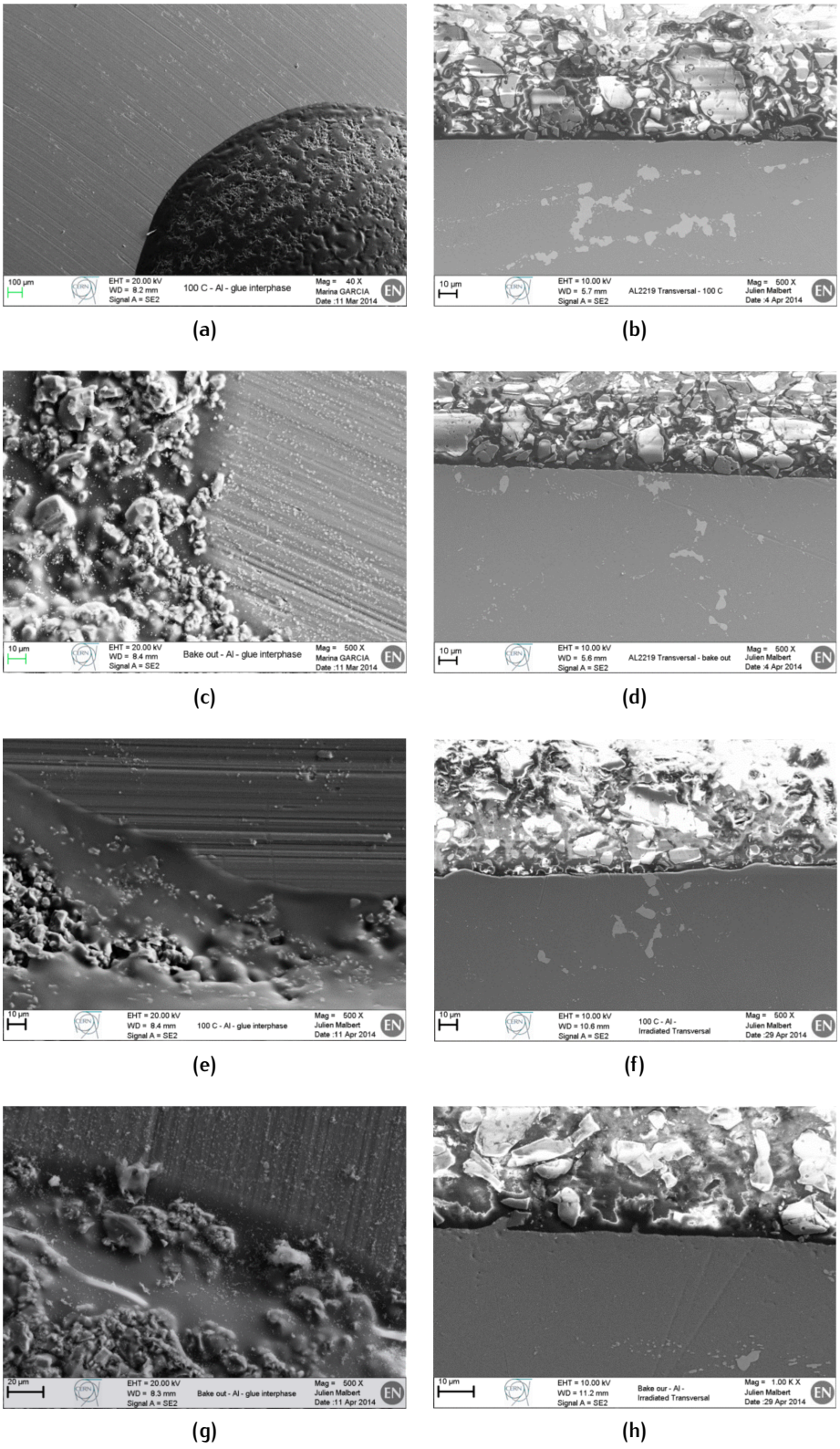

Figure 42: Al2219 samples SE views of the surface (a,c,e,g) and of the cross section (b,d,f,h) after the following treatments: 100°C (a,b), bakeout (c,d), 100°C plus γ-irradiation at 200kGy (e,f), bakout plus γ-irradiation at 200kGy (g,h).

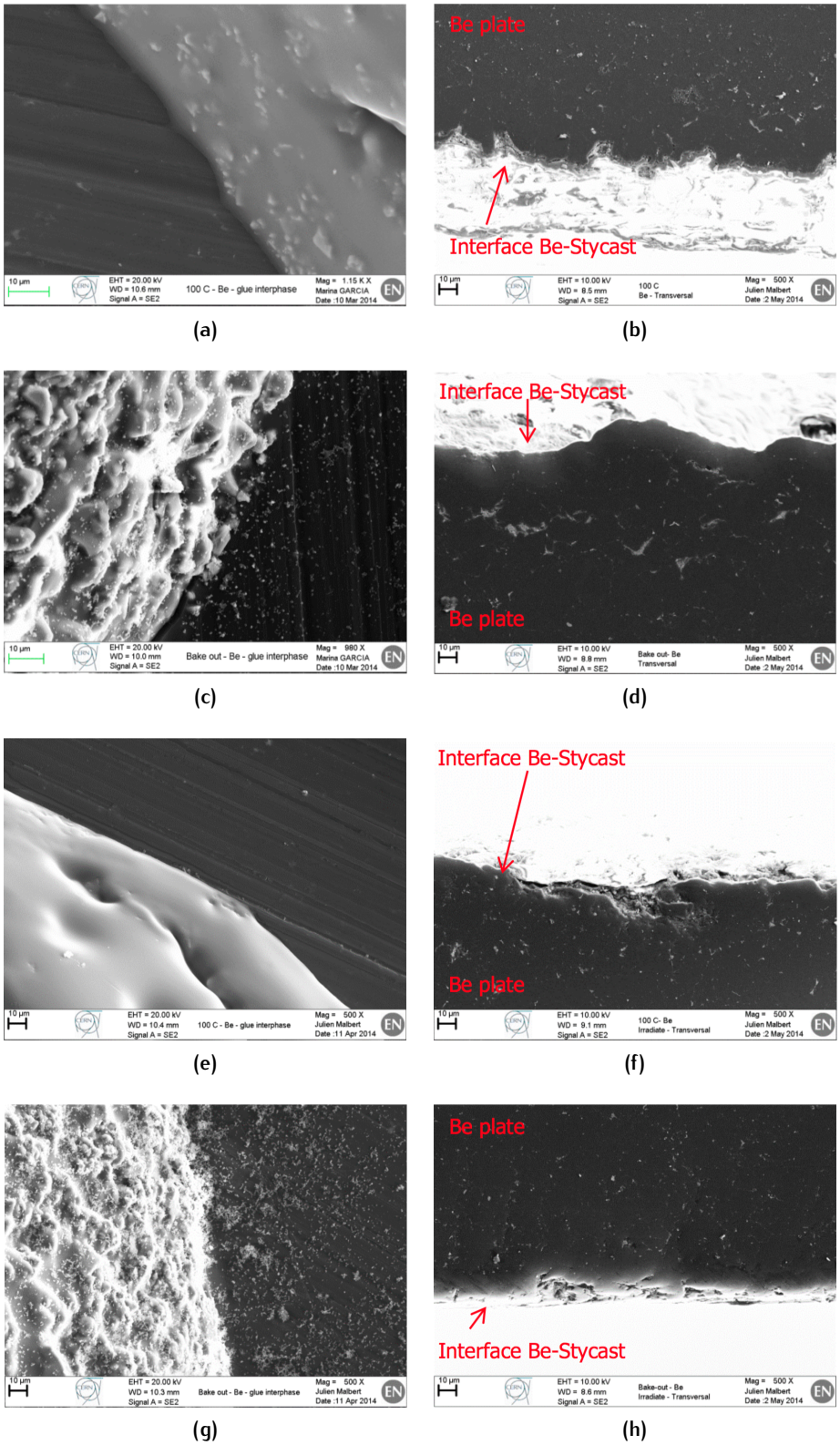

Figure 43: Al2219 samples SE views of the surface (a,c,e,g) and of the cross section (b,d,f,h) after the following treatments: 100°C (a,b), bakeout (c,d), 100°C plus γ-irradiation at 200kGy (e,f), bakout plus γ-irradiation at 200kGy (g,h).

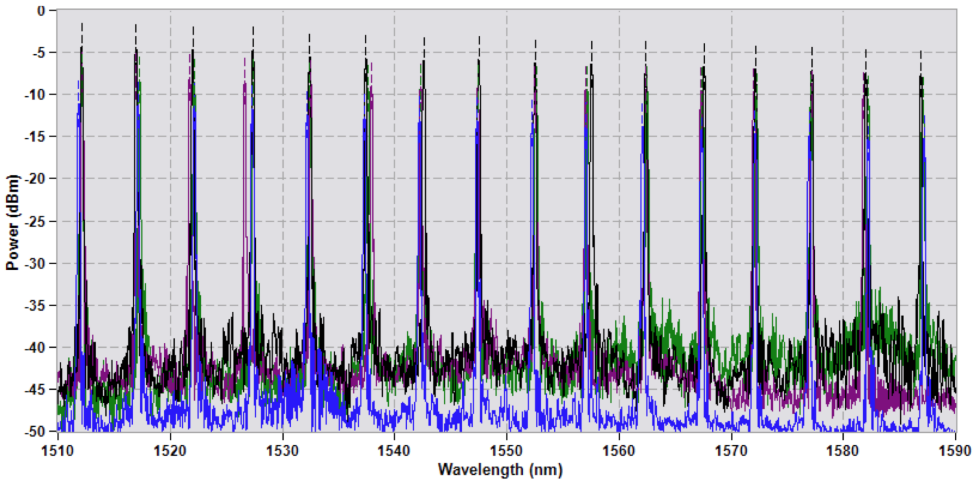

Figure 44: Spectra of the four arrays of the iPipe monitoring system as recorded with a MOI SM125 soon after the installation of the fiber on the CMS central beam pipe.

gluing strength in specific laboratories. Before the sensor array gluing, we had to position the fibre in the nominal position using temporary Kapton foil collars, removed after 24h curing of the glue. A part of the strain sensor positions, we secured the correct positioning of the fibre with additional gluing dots. In the technical specifications of iPipe project we were requested to secure a maximal sag of fibre by 200 micron with respect to the external beam pipe surface. This was mandatory to avoid any possible contact of fibre arrays with insertion of next generation CMS Pixel Tracker. Each array was positioned and glued in 24h. The day after the beam pipe was rotated by 90 degrees in order to have always the next array gluing position on top of the beam pipe. In 4 days the full setup of 4 fibres was successfully installed on the beam pipe. During the following week, the beam pipe was packed and shipped to CMS underground site for final installation in the CMS detector. The installation was completed by the end of June 2014.

3.5.4 The bakeout

To avoid colliding with gas molecules inside the accelerator, the beams of particles in the LHC must travel in a vacuum as empty as interstellar space: ultra-high vacuum is needed for the pipes in which particle beams travel. This includes 48 km of arc sections, kept at 1.9 K, and 6 km of straight sections, kept at room temperature, where beam-control systems and the insertion regions for the experiments are located.
In the arcs, the ultra-high vacuum is maintained by cryogenic pumping of 9000 cubic metres of gas. As the beam pipes are cooled to extremely low temperatures, the gases condense and adhere to the walls of the beam pipe

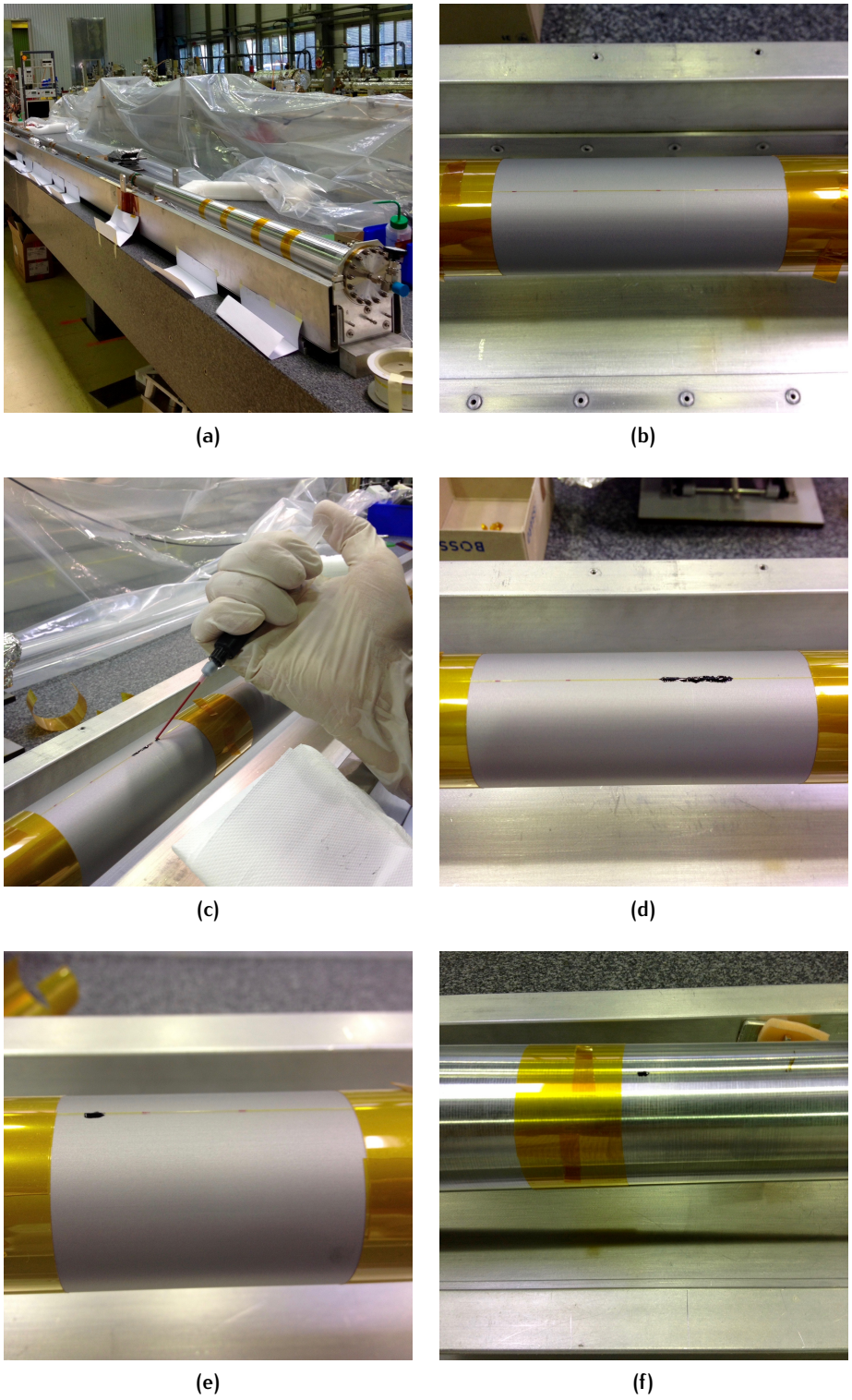

(a) (b) (c) (d) (e) (f)

Figure 45: Highlight of the various installation and gluing phases.The whole CMS central beam pipe structure with the Kapton collars to hold the fiber is shown in (a,b); the gluing of the strain sensors is made to see in (c,d); pictures of one of the gluing spot to reduce the fiber sagging on the Be (e) and Al (f) sectors.

by adsorption. Just under two weeks of pumping are required to bring the pressures down below $1.013 \cdot 10^{-10}$ mbar.
Two important design features maintain the ultra-high vacuum in the room-temperature sections. Firstly, these sections make widespread use of a non-evaporable *getter coating*, developed and industrialized at CERN, that absorbs residual molecules when heated. The coating consists of a thin liner of titanium-zirconium-vanadium alloy deposited inside the beam pipes. It acts as a distributed pumping system, effective for removing all gases except methane and the noble gases. These residual gases are removed by the 780 ion pumps. Secondly, the room-temperature sections allow bakeout of all components at 250°C. Bakeout is a procedure in which the vacuum chambers are heated from the outside in order to improve the quality of the vacuum. This operation needs to be performed at regular intervals to keep the vacuum at the desired low pressure.
The bakeout of the CMS central beam pipe has been performed soon after its installation inside the CMS detector, in August 2015. The beam pipe was set to nominal vacuum level and external heating up to 250°C was performed to secure the removal of any residual gas molecules attached to internal beam pipe metal walls. The consequent thermal expansion was causing a global elongation of beam pipe up to 3 mm in the Beryllium (Be) region and up to 1.5 mm in each of the two Aluminum2219 (Al) regions for an overall elongation of 6 mm. In despite of the extra length left between fibre gluing positions, we suffered some breaking points along the fibres. Some of them were happening in accessible regions and were subsequently repaired by fibres splicing in situ. Some of them were not recoverable and we could profit of the fibre double end reading in order to maximize the amount of readout sensors. Some other sensors (mostly strain ones) were suffering spectrum deterioration during the bakeout phase and consequently were tagged as not reliable anymore. At the end of the fibre recovering phase and sensors quality control we secured 40 reliable sensors out of the 64 initially installed. In Figure 46, the spectra after the recovery operation performed, in the months following the bakeout, are shown. The redundancy of amount of sensors initially defined in the iPipe project design turned out to be a relevant element to secure the final performance of the beam pipe monitoring system.

3.5.5 The need for recalibration

After the arrays installation on the beam pipe, the λ_0 of all the sensors has been re-calibrated in order to take into account the installation induced shift, with respect to the firm calibration parameters. Moreover, the extreme stressing conditions suffered during the bake-out made necessary a further re-calibrations of the sensors in order to take into account any effect on the λ_0 and sensitivity. Those actions have been performed while the beam pipe was still accessible making use of different local electronic sensors as references.

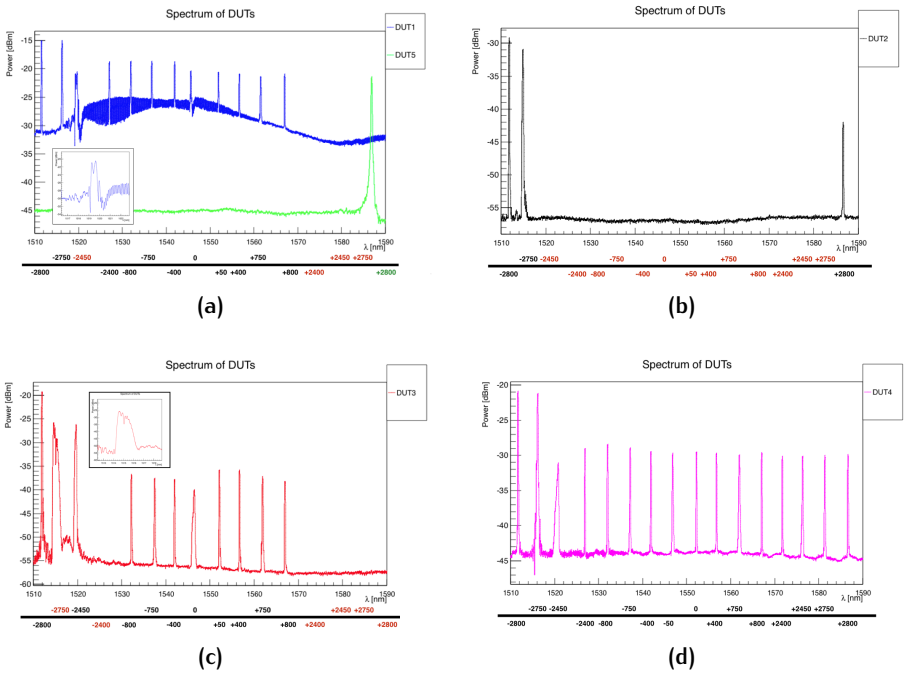

Figure 46: Spectra of the iPipe monitoring system, as recorded with via the FOS4CMS DAQ, soon after the installation of the fiber on the CMS central beam pipe. Distorted peaks are presents in the fibers TOP (a) and BOTTOM (c). The fiber FAR is almost not avilable (b), while the fiber NEAR has been completely recovered.

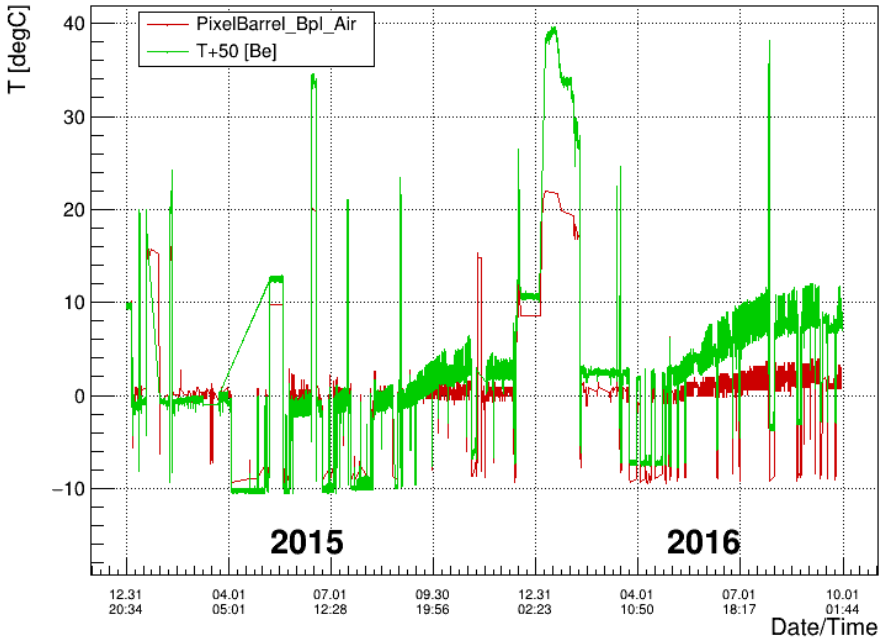

Figure 47: Temperature dynamic next to the IP as recorded by the iPipe T+50 sensor (green) and by an electronic sensor from the Pixel detector (red), from January 2015 to October 2016.

Figure 47 shows the temperature dynamic of the T+50 sensor, calculated with the parameter estimated from an *in situ* calibration of the λ_0. It is evident, by looking at the temperature dynamic of a reference electronic sensor of the Pixel placed nearby the IP, that this set of calibration parameters is not valid anymore when the temperature approaches the room temperature value. The presence of real thermal gradient between this two sensors, away from each other 3cm in the vertical direction, could not be physically explained assuming that the λ_B is changing only because of the thermo-optic effect.

After several recalibration trials and following the conclusions of several fruitful discussions with the Pixel temperature experts colleagues, we've decided to calibrate the iPipe temperature sensors with respect to the Pixel temperature sensors profiting of the last months of LS1, that is to say January and February 2015, and the commissioning phase which last up to beginning of May 2015. In these periods the temperature variations are only influenced by the Pixel cooling system and the Pixel volume can be considered to be in thermal equilibrium.

Figure 48 is a scatter plot between the λ_B of the sensor T+50 and the temperature recorded by the nearby Pixel temperature sensors. The distribution clearly show the presence of a wavelength shift not referable to the thermo-optic effect. Nevertheless, the distribution can be nicely fitted with to straight line with different slope. The best functions have been

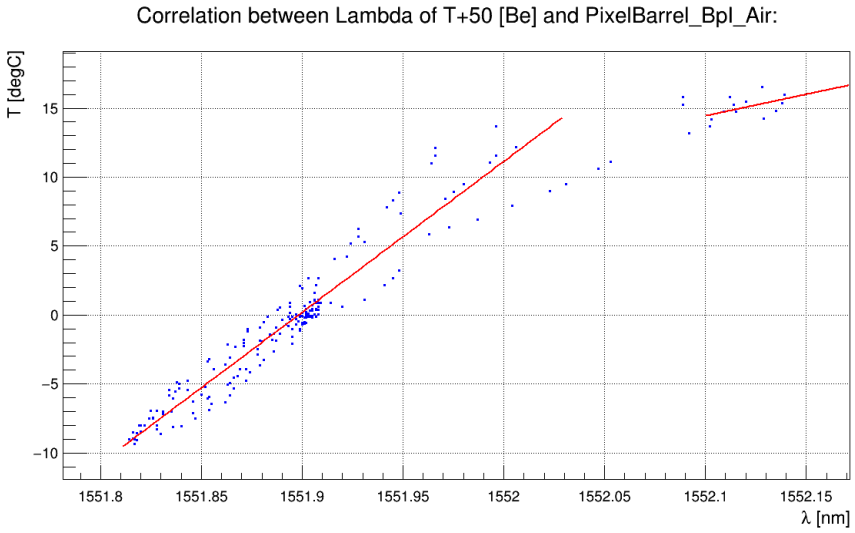

Figure 48: Correlation between the λ of T+50 and the temperature measured by the nearby Pixel's reference sensor. From a double linear fit, by minimizing the χ^2 the calibration constants are estimated. The turn around point is estimated to be at $\lambda = 1552$nm corresponding to the reference temperature of 11.4°C.

estimated with a linear fit by minimizing[3] the χ^2 and the intersection point of the two straight line represent the wavelength at which the slope changes. The temperature dynamic measured by the FBG at 50 mm from the IP, *i.e.* T+50, next to the one recorded by the nearby Pixel electronic sensor during the whole 2015 operation is shown in Figure 49, proving the reliability of the latter calibration parameters. This recalibration procedure has been applied to all the iPipe reliable temperature sensors and in Figure 50 the fits for the sensors T±400 and T±800 on the fiber TOP are shown. From these plots it is evident that a double straight line calibration is not needed for all the sensors. This last observation excludes the possibility that the change of the FBG response is due to the influence on the thermo-optic coefficient of thermal condition to which they have been exposed during the bakeout. However, the elasto-optic effect could be involved in this phenomenon. Indeed, considering that the critcal temperature for the glue is 155°C and that during the bakeout the central beam pipe has been subjected to a global elongation on ∼6 mm and recalling, from the section above, the way in which the fiber has been installed on the beam pipe, we can assume that a new tensioning state is present on the fiber from the end of the bakeout.
Nevertheless, the iPipe temperature monitoring is reliably working 24/7 since the beginning of 2015 and the monitoring data are currently displayed in the CMS Detector Control System (DCS).

3

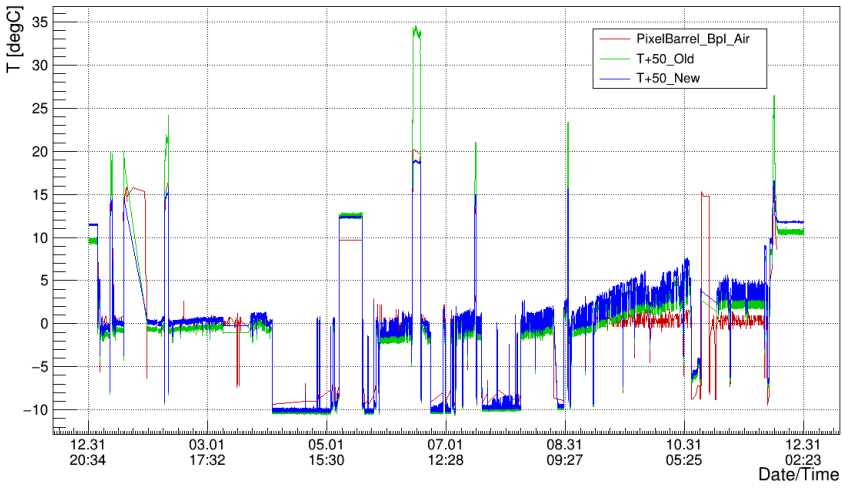

Figure 49: Temperature dynamic next to the IP as recorded by an electronic sensor from the Pixel detector (red) and the iPipe T+50 sensor, with the old calibration (green) and with the new double line calibration (blu), from January 2015 to October 2016.

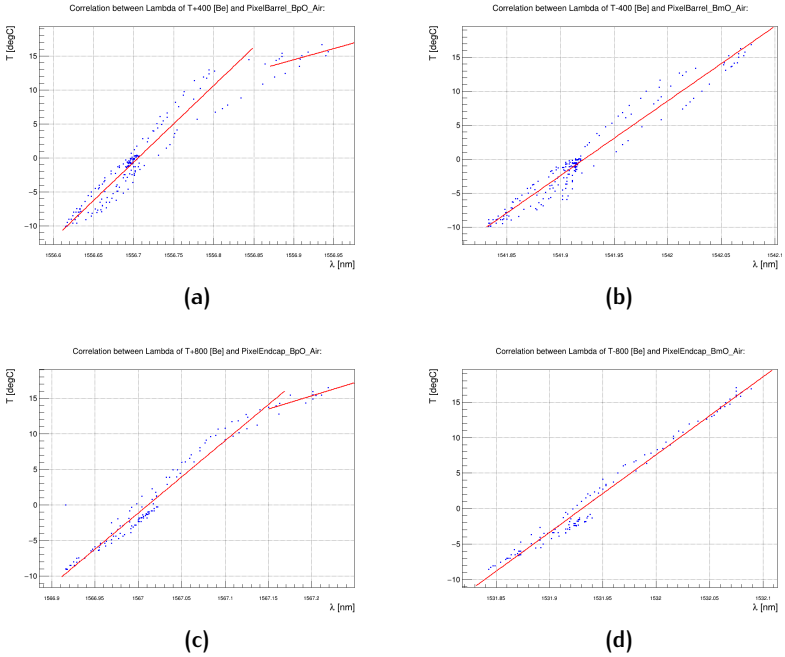

Figure 50: Correlation between the λ of T+400 (a), T-400(b), T+800(c), T-800(d) and the temperature measured by the nearby Pixel's reference sensor. The calibration parameters and well as the turn around point are estimated with a double linear fit (a,c) or with a linear fit (b,d), by minimizing the χ^2.

3.6 TEMPERATURE MONITORING

In Figure 51 it is shown the temperature profile of the beam pipe during the CMS operation throughout 2015 and 2016. As depicted in the beginning paragraphs of the chapter, the CMS central beam pipe in located inside the Pixel detector volume. The power consumption per pixel is estimated to be around 60μW; for the total of $\approx$ 39 million pixels, which compose the Pixel detector, this add up to 2.3kW. In order to ensure correct operation, the pixels of the temperature should be maintained at -10 degrees (a detailed description of the Pixel detector can be found in [77]).
As mention in the previous section, the re-calibration procedure of the iPipe temperature sensors has been done profiting of the Pixel temperature sensors, assuming that the thermal environment in the Pixel volume before the start of the LHC Run2 is driven only by the Pixel cooling system. Three main temperature intervals can be identified that correspond to different configuration of the CMS detector:

- room temperature, when the detector is in maintenance during the technical stop;
- ten degrees, when the detector is closed, the pixels boards and cooling system are off;
- between zero and minus ten degrees, when the detector is closed, the pixels boards are on and the cooling is on;
- minus ten degrees, when the detector is closed, the pixels board are off and the cooling is on.

From Figure 51, it is clearly visible the temperature gradient between the beryllium and the aluminium sectors of the central beam pipe. The beryllium part, *i.e.* the sensor from T+800 to T-800, is at $4 \div 9 \pm 1^{\circ}$C when the detector is closed but not operational and the cooling is on, while the aluminium parts are 3°C colder.

3.6.1 Considerations on radiation induced shift

The iPipe fibers can be considered as the closest detector with respect to the impact point. Indeed, the Pixel silicium sensors, after the EYETS2017 upgrade, will be at 29mm from the outer surface on the central beam pipe, while the iPipe fiber are in direct contact with the vacuum chamber. This implies that, our fibers will be exposed to all the particle resulting from the p-p collisions since the vacuum chamber wall are made of beryllium with the intend to minimize the particle interaction with it. This means that, during the LHC operations, the iPipe fiber will be exposed to a mixed radiation field resulting from the particles, leptons and hadrons, produced in the p-p collisions. The intensity of the ionizing radiation, during a time interval, is correlated with

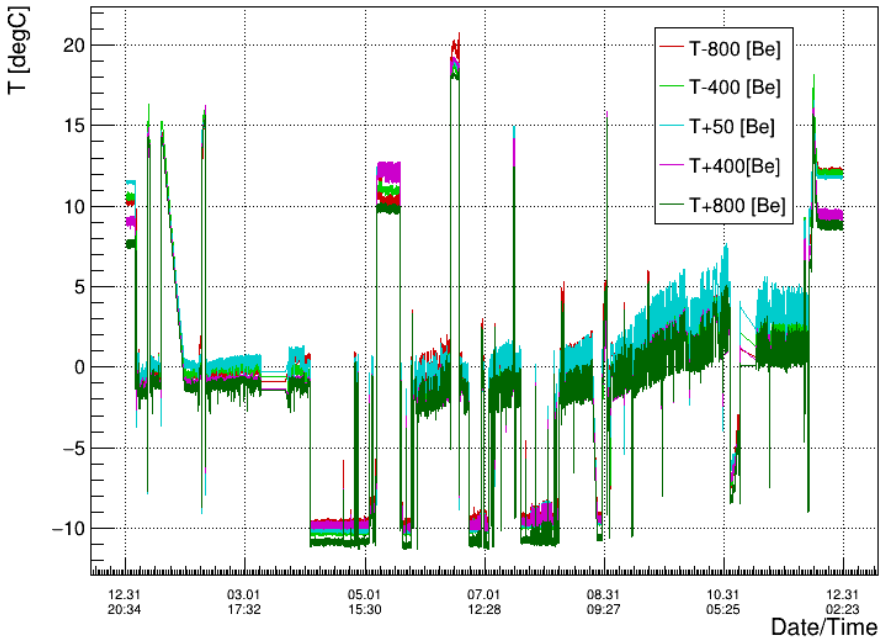

(a)

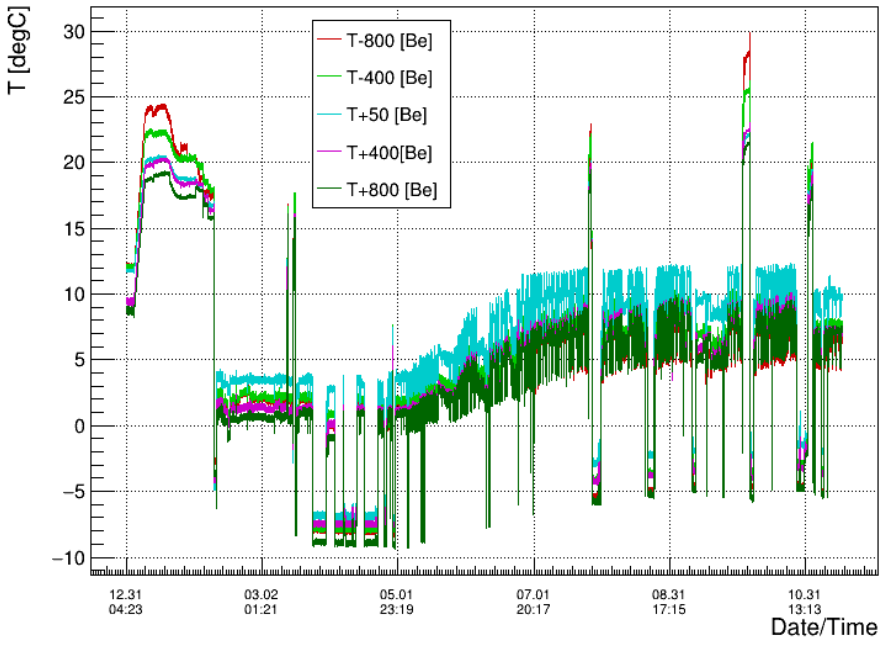

(b)

Figure 51: Temperature profile of the beam pipe during the CMS operation throughout 2015, (a), and 2016, (b).

the LHC delivered integrated luminosity.
Luminosity is an important indicator of the performance of an accelerator: it is proportional to the number of collisions that occur in a given amount of time. The luminosity is a quantity that measures the ability of a particle accelerator to produce the required number of interactions. It is the proportionality factor between the number of events per second dR/dt and the cross section σ_p:

$$\frac{dR}{dt} = L \cdot \sigma_p$$

Therefore, the unit of the luminosity is $cm^{-2}s^{-1}$. The formula for the luminosity of two Gaussian beams colliding head-on is given by:

$$L = \frac{N_1 N_2 f N_b}{4\pi\sigma_x\sigma_y}$$

where N_1 and N_2 are the number of particles per bunch, f the revolution frequency and N_b the number of bunches. The higher the luminosity, the more data the experiments can gather to allow them to observe rare processes.
On the other hand, the absorbed radiation dose is the mean energy deposited per unit mass, taking into account all the energy loss mechanisms. Ionization is the dominant energy loss mechanism in the Pixel volume. From the integrated luminosity it is possible to estimate the delivered dose over one year considering that one year of LHC operation corresponds to $8{\cdot}10^{15}$ inelastic proton-proton collisions, assuming an instant luminosity of $10^{34}\mathrm{cm}^{-2}\mathrm{s}^{-1}$, an inelastic cross-section of 80mb and a data taking period of 10^7s.
The profile of the integrated, LHC delivered and CMS recorded, luminosity during 2015 and 2016 in shown in Figure 52. Comparing these plots with the trends of the iPipe sensor T+50 in Figure **??** it is evident that the increase in luminosity correspond to an apparent increase in the temperature which reflect the Bragg wavelength shift (BWS) due to the ionizing radiation (see Chapter 2).
Thanks to the CMS BRIL community we are able to have an estimation, based on FLUKA simulation, of the deposited dose, as function of the coordinate system of CMS, with respect to the total integrated luminosity. From these calculation we can say that a total dose of O(10^6) Gy as been delivered during the 2016 operations while a total dose of O(10^5) Gy was delivered during 2015. The BWS are in agreement with those presented in literature, as for example the review paper [4] and in Figure **??**.
Finally, it should be noted that, in 2016, there is a walkaway also in the temperature measurement of the Pixel sensors. This is a physical temperature increase related to the radiation induced damage in the silicium boards of the Pixel detector, [7].

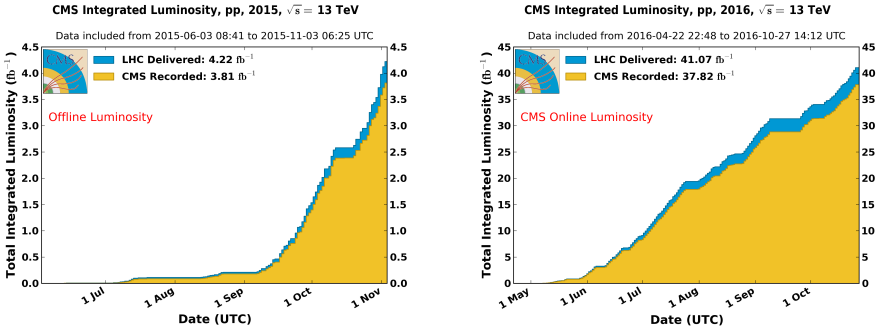

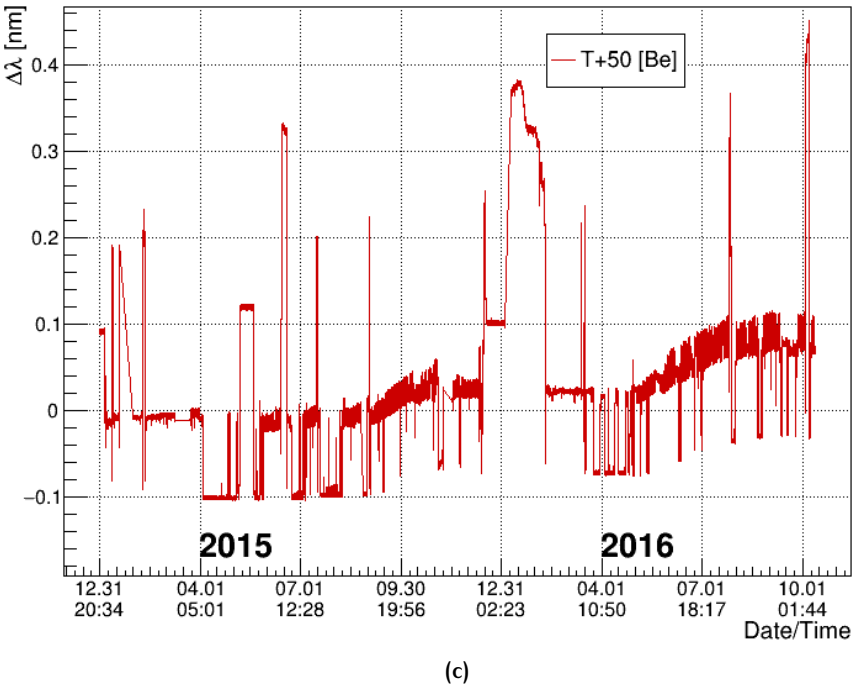

Figure 52: Delivered and integrated luminosity in the CMS detector during the LHC p-p collisions of 2015(a) and 2016 (b), and Bragg wavelength shit of sensor T+50 during 2015 and 2016 operations.

3.7 STRAIN MONITORING

To correctly evaluate the strain, it is necessary to separate strain and temperature effect in order to compensate the thermal apparent strain effect. Since in the CMS central beam pipe fibre optic monitoring system the temperature sensors are not bonded on the beam pipe, they can be considered strain-free and used as compensators.
In the previous chapter the FBG sensing features have been explained in details. Before showing the iPipe strain measurements it is necessary to recall and extend the physical phenomena behind the strain sensitivity of the FBG. In general, the grating's sensitivity is governed by the fiber elastic, elasto-optic and thermo-optic properties and the nature of the load or strain which is applied to the structure that the fiber is attached to or embedded within. Strain shifts the Bragg wavelength through dilating or compressing the grating and changing the effective index. The amount of wavelength shift is given by:

$$\frac{\delta\lambda_B}{\lambda_B} = (\frac{n^2}{2})[p_{11}\epsilon_1 + p_{12}(\epsilon_1 + \epsilon_2)] \tag{17}$$

where the principal strains are ϵ_1 along the fiber axis and ϵ_2 transverse to the fiber axis. If the strain is homogeneous and isotropic, then 17 simplifies into:

$$\frac{\delta\lambda_B}{\lambda_B} = [1 - p_e]\epsilon \approx 0.78\epsilon \tag{18}$$

where p_e express the photoelastic contributions as a function of the Poisson ratio and the fiber Pockel's coefficients [13], and is defined as:

$$p_e = (\frac{n^2}{2})[p_{12} - \mu(p_{11} + p_{12})] \tag{19}$$

As depicted in Figure 41, in our monitoring system there is a temperature measuring FBG at 5 cm distance from each strain measuring FBG. The strain sensors have been bonded on the beam pipe external surface by means of a thin layer of Stycast glue (see picture in Figure 45) while the temperature sensors are left free.
In general, the wavelength of an FBG sensors changed with strain and temperature:

$$\frac{\Delta\lambda}{\lambda_0} = k \cdot \epsilon + \alpha_\delta \Delta T \tag{20}$$

alpha where λ_0 is the base wavelength in the reference thermal and mechanical condition, $k = 1 - p_e$ is the gage factor, and $\alpha_\delta = \frac{\delta n/n}{\Delta T}$ express the change of the refractive index as a consequence of the temperature variation. The first term of equation 20, $k \cdot \epsilon$ describes the strain impact caused by force, ϵ_M, and temperature through the thermal expansion coefficient of the specimen, $\epsilon_T = \alpha_{sp}\Delta T$:

$$\epsilon = \epsilon_M + \epsilon_T \tag{21}$$

Going back to equation 20, it can be rewritten as follow:

$$\frac{\Delta\lambda^S}{\lambda_0^S} = k \cdot \epsilon_M + (k \cdot \alpha_{sp} + \alpha_\delta)\Delta T \tag{22}$$

If the FBG is not mechanically stressed, the signal $\Delta\lambda/\lambda_0$ will change only with temperature according to:

$$\frac{\Delta\lambda^T}{\lambda_0^T} = (k \cdot \alpha_{fiber} + \alpha_\delta)\Delta T \tag{23}$$

since the only mechanical effect acting on the grating is the thermal expansion of the fiber itself. Tipically, $\alpha_{fiber} \sim 0.5 \cdot 10^{-6}/K$ while the impact of the change of refractive index on the signal variation is one order of magnitude bigger, $\alpha_\delta \sim 5 \cdot 10^{-6}/K$.
When, as it is the case of the strain FBG of the iPipe monitoring system, a FBG sensor is fixed on a specimen the signal $\Delta\lambda/\lambda_0$ change with the strain on the specimen, ϵ, and therefore the thermal expansion coefficient is α_{sp} and not α_{fiber}[4]. From equation 22, we can desume an equation for a strain measuring FBG:

$$\epsilon_M = \frac{1}{k}\frac{\Delta\lambda}{\lambda_0} - \left(\alpha_{sp} + \frac{\alpha_\delta}{k}\right)\Delta T \tag{24}$$

From this last equation it follows that it is possible to have a measure of the mechanical strain, ϵ_M by means of a temperature compensation FBG, *i.e.* a temperature measuring FBG placed in a region of the specimen not subjected to any mechanical stress whose signal changes according to the following equation:

$$\frac{\Delta\lambda^C}{\lambda_0^C} = (k \cdot \alpha_{sp} + \alpha_\delta)\Delta T \tag{25}$$

Considering the layout of the iPipe monitoring system, the temperature FBG cannot be considered as temperature compensator since their signal variation is not divren by α_{sp}, as can be clearly seen in the plot presented in Figure 53, where the λ dynamic of the sensors T+50 and So are shown. By subtracting the signal of the sensor T+50, eq. 23, from that of So, eq. 22, we obtain the strain, $\epsilon = \epsilon_M + \epsilon_T$, acting on the IP of the CMS central beam pipe:

$$\epsilon = \frac{1}{k}\left(\frac{\Delta\lambda^S}{\lambda_0^S} - \frac{\Delta\lambda^T}{\lambda_0^T}\right) \tag{26}$$

In Figure 54 the strain dynamic over the 2015 (a) and 2016(b) operation of the CMS detector is shown. This plots reflect the thermal dynamic shown in Figure 51 in term of expansion and contraction of the structure caused

4 The thermal expansion coefficient for the metal of the CMS central beam pipe are $\alpha_{Al} = xx \cdot 10^{-6}/K$ and $\alpha_{Be} = xx \cdot 10^{-6}/K$

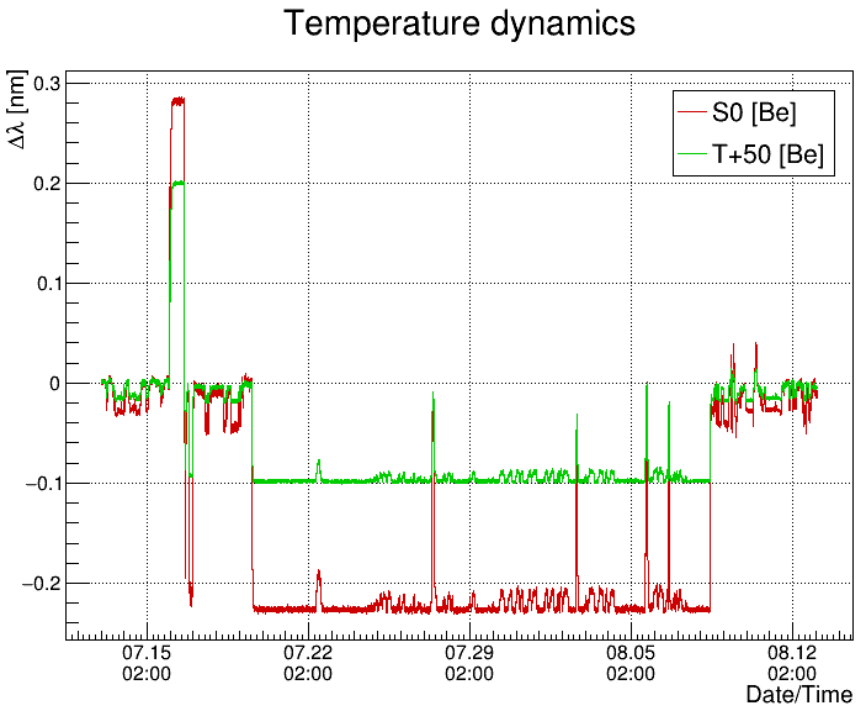

Figure 53: Temperature induced relative variation of the signal of the iPipe strain sensor at the IP, S0 (red), and the nearby temperature sensor T+50 (green).

by the temperature changes described in the previous section. The reference condition, *i.e.* zero strain, is set when the detector is closed and operational. In particular, it was set on March 24th, when the CMS detector was closed at the end of the upgrade operations of the LS1. The compressions and expansions are in agreement with the thermal model of the beam pipe, presented in Figure 40.

3.7.1 Magnetic field induced strain

The CMS magnet is the central device around which the experiment is built, with a 4 Tesla magnetic field. It is superconducting solenoid whose job is to bend the paths of particles emerging from high-energy collisions in the LHC. The more momentum a particle has the less its path is curved by the magnetic field, so tracing its path gives a measure of momentum. CMS began with the aim of having the strongest magnet possible because a higher strength field bends paths more and, combined with high-precision position measurements in the tracker and muon detectors, this allows accurate measurement of the momentum of even high-energy particles. As widely described in the previous chapter, the tracker and calorimeter detectors fit snugly inside the magnet coil whilst the muon detectors are interleaved with a 12-sided iron structure that surrounds the magnet coils and contains and guides the field. The enormous magnet also provides most of the

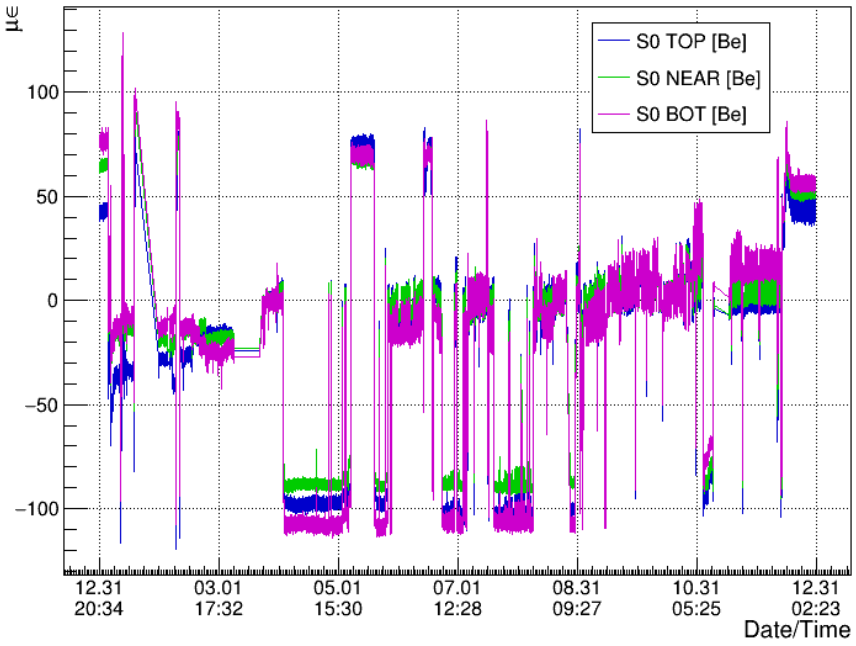

(a)

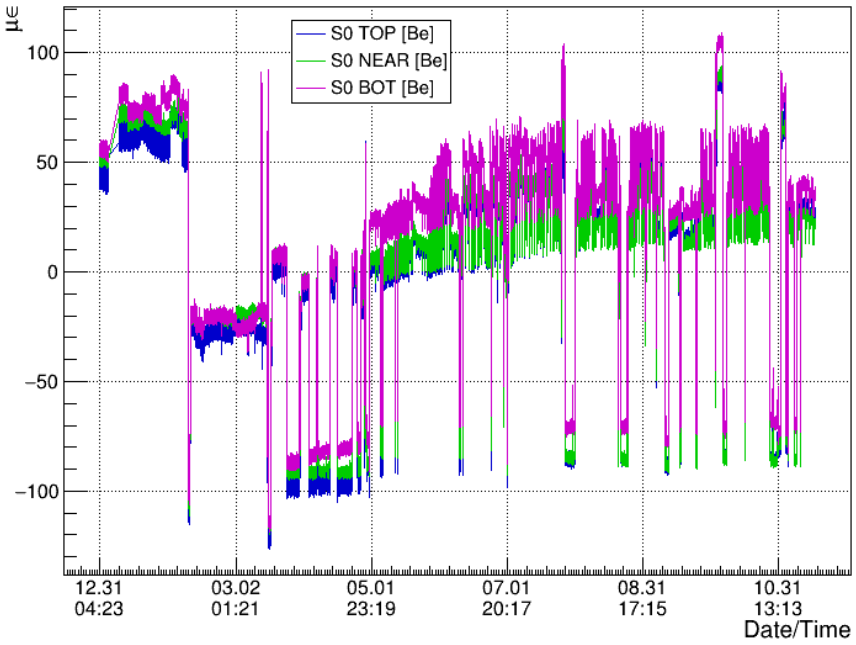

(b)

Figure 54: Strain dynamic on the beam pipe during the CMS operation throughout 2015, (a), and 2016, (b)

experiment's structural support, and must be very strong itself to withstand the forces of its own magnetic field.
When the magnetic field is switched on, the CMS Endcap structure shrinks toward the center of $\approx$ 13 mm resulting in mechanical forces acting on the double bellows, that may induce stress on the central beryllium beam pipe. The same happens when the solenoid ramps down, but in opposite direction. The supports involved in the movement, with reference to Figure 32, are the Endcap (10.4m) and the HF (13.7m) ones, while the other subsequent sectors of the CMS beam pipe do not introduce any mechanical stress on the central beam pipe when the solenoid magnet ramps.
In Figure 55a it is shown the λ variation during a magnet ramp-up, from 0 to 3.8T, of the sensors T+50 and S0 on the fiber installed on the TOP position. Before the start of the ramp, there is a decrease of the temperature of the beam pipe volume which reflects in a compression (ϵ_T) of the beam pipe structure. During the ramp the temperature is stable while the signal of the strain sensor exhibit a complex dynamic related to the mechanical component of the strain (ϵ_M) acting on the beam pipe. In Figure 55b the strain, calculated from eq. 26, acting on the IP is plotted for the three available sensing positions. It is evident that, while the field is ramping, the beam pipe is subjected to mechanical deformations of the order of 30 $\mu\epsilon$. The complexity of the motion is evident also in the difference between the strain dynamic of the three sensors, that reflects the fact that the magnetic field acts on the CMS structure dragging the Endcap towards his magnetic center.

Figure 56a shows the strain dynamic during a multistep ramp-up happened on September, 14th. It is worth to be noticed that once the B-field ramp reaches his first plateau the loading on the beam pipe is kept constant until the restart of the ramp when the movement picks up from where it left, reproducing almost the same dynamic shown in picture Figure 55b. In Figure 56b the strain deformations acting during a magnet ramp-down are shown. By way of example, in Figure 57 it is presented the strain at different sensing position along the beam pipe, S$\pm$750, S-2450 and S-2750 for the same ramp-up shown in Figure 55b.

Finally, in Figure 58 the relative strain, calculated with respect to the beginning of the ramp, of several ramps, occurred during the 2015, is plotted versus the magnetic field intensity. Figure 58a shows a set of ramp-up while a set of ramp-down, to be observed from right to left, is shown in Figure 58b.

In conclusion, we can state that the strain recorded on the central beam pipe by our monitoring system results from magnetic induced forces acting on the double bellows during the variations of the magnetic field. However, the amplitude of these strain deformations is negligible from a mechanical safety point of view. Indeed, during the magnetic field gradient the whole CMS beam pipe structure in subject to mechanical deformation of the order of $\approx$ 10 mm while the maximum measured strain deformations on the central beam pipe are of the order of 20$\mu\epsilon$.

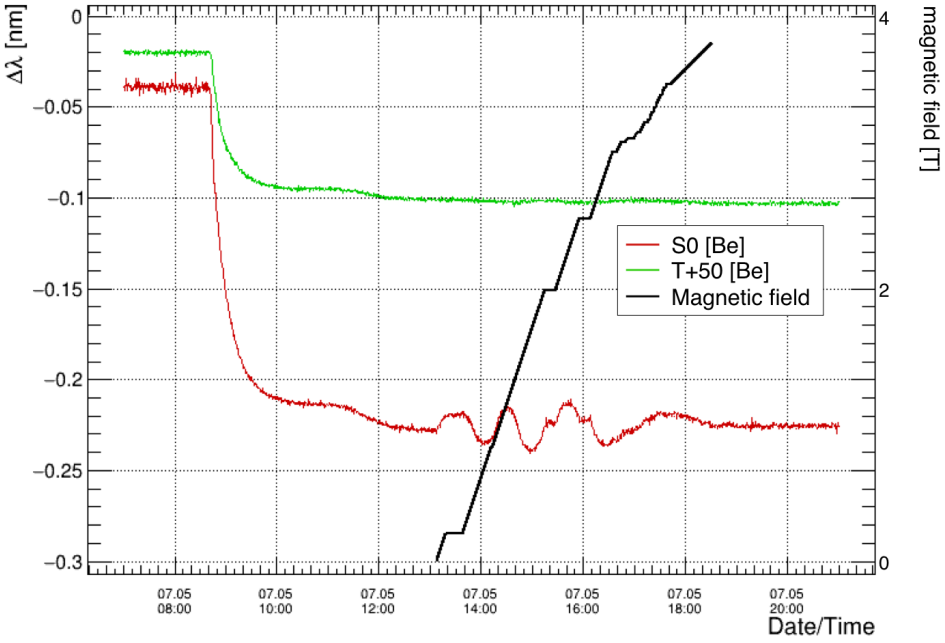

(a)

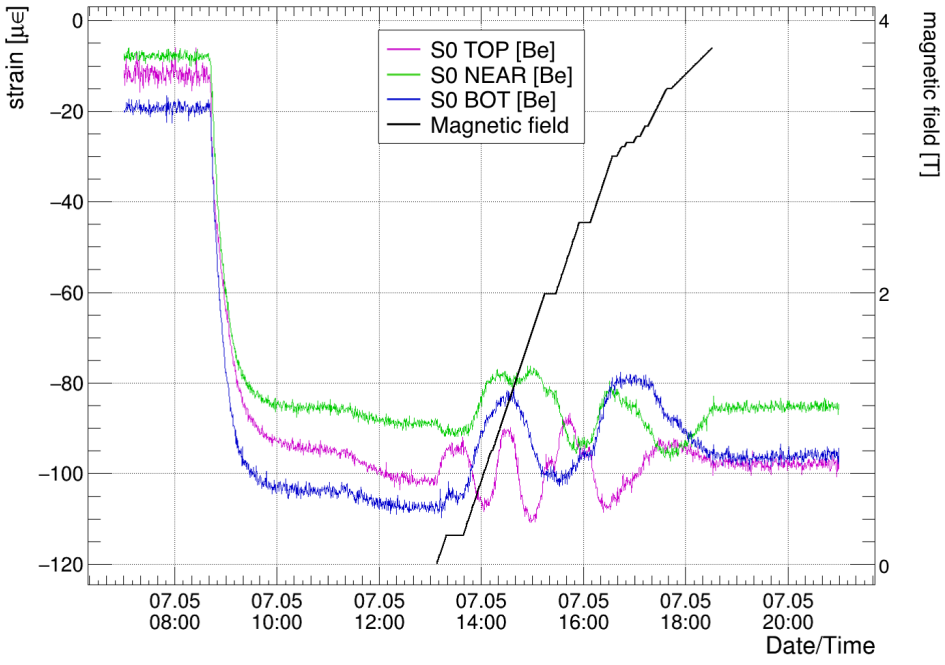

(b)

Figure 55: Comparison of the relative λ variation of one of the iPipe strain sensor at the IP, S0 (red), and the nearby temperature sensor, T+50 (green), during a magnet ramp happened on July, 5^{th} 2015 is presented in (a). The strain evolution, as recorded from the three available strain sensors at S0, during the ramp-up of the B-field is shown in (b).

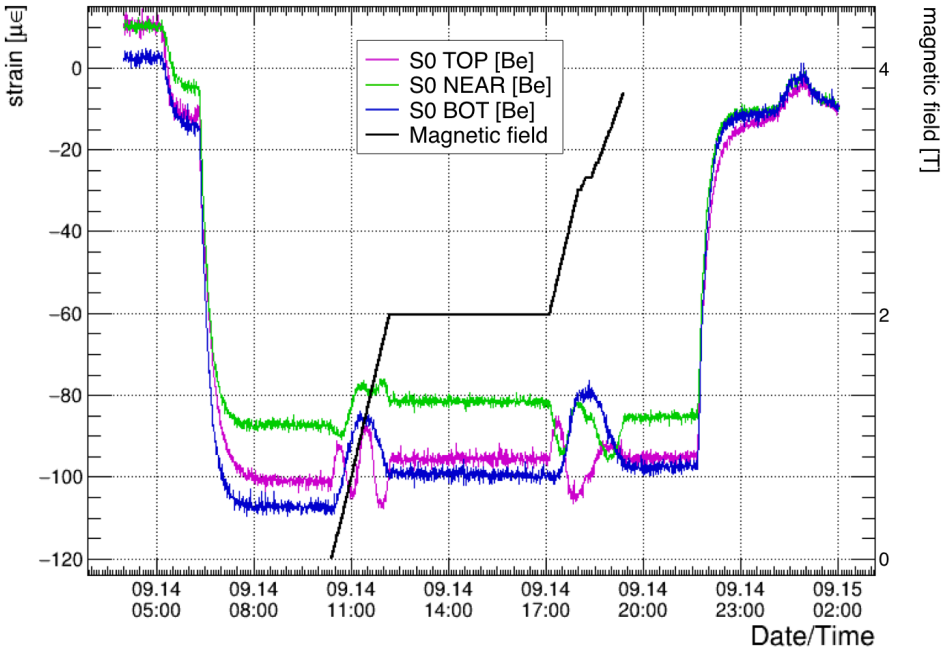

(a)

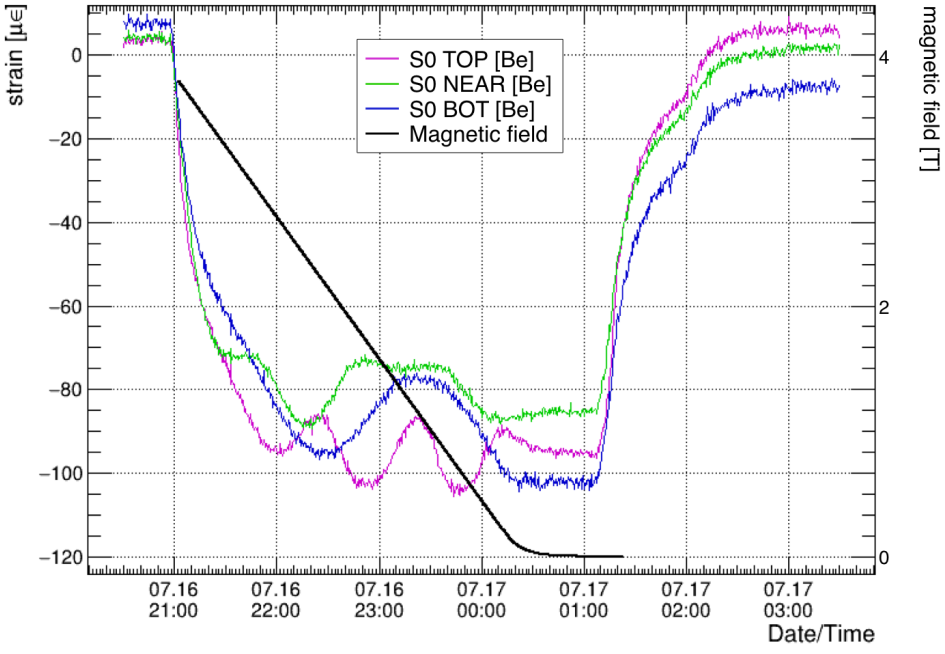

(b)

Figure 56: Strain evolution during a B-field multi-step ramp-up (a) on September, 14^{th} 2015 and during a ramp-down (b) on July, 16^{th} 2015, as recorded from the three available strain sensors at S0.

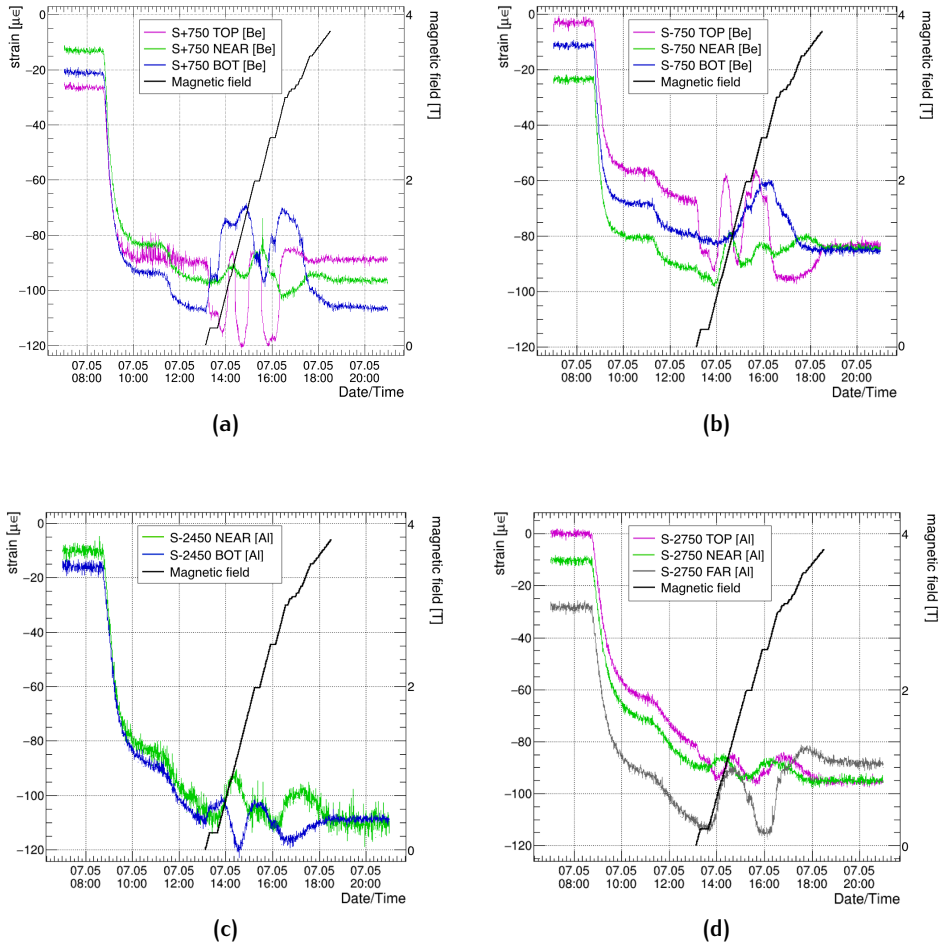

Figure 57: Strain evolution during a B-field ramp-up happened on July, 5^{th} 2015, as recorded from the available strain sensors at S+750 (a), S-750 (b), S-2450 (c) and S-2750 (d).

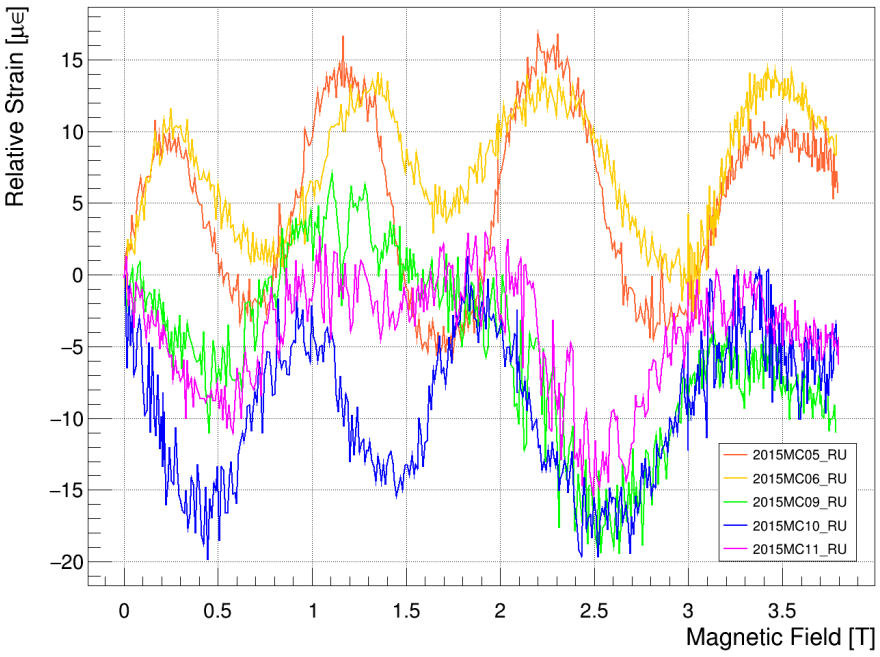

(a)

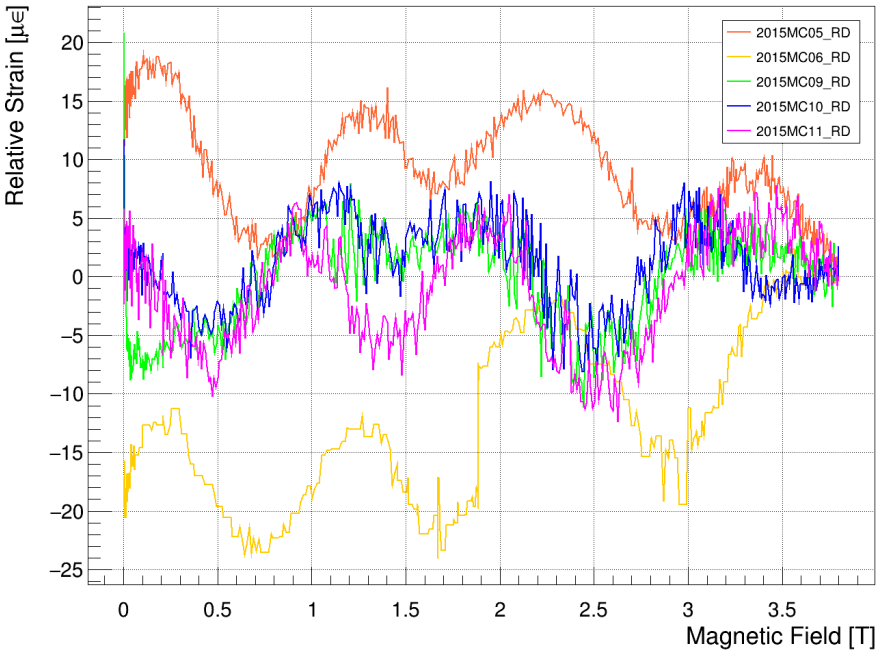

(b)

Figure 58: Relative strain during several magnet ramps (details in table). The magnitude of the oscillation during the ramps-up, (a), is $\approx 20\mu$m. The same applies to the ramps-down, (b), whose plot must be read from right to left.

Moreover, these results prove the extreme high sensitivity of our FBG strain sensors and validate their level of reproducibility. During the 2017 Technical Stop, *i.e.* from January to April, the new Pixel detector with 4 silicon layers will be installed and it will be placed at only 1,5 mm from central beam pipe external face. During the future CMS operations, the mechanical stability of the central beam pipe will be a crucial parameter to be monitored since an abnormal deformation could be very dangerous for the surrounding detectors.

3.8 CONCLUSION

The iPipe system has proved to be an important innovation in the framework of the Structural health monitoring of crucial parts of the CMS detector and LHC beam pipe.
The work related to this chapter of the Thesis has been of fundamental importance for the manufacturing of the iPipe system, its installation, commissioning and operation. The iPipe system data analysis demonstrated the complete fulfillment of the initial technical specs in terms of monitoring and quantify any deformation induced on the CMS central beam pipe during the experiment and LHC operations. Moreover, the data analysis here presented proved the overall sensitivity and reliability of this innovative and effective monitoring system.
The measure of the mechanical stability of the CMS central beam pipe was of critical importance in the view of the reduction of the clearance between the beam pipe and the surrounding Pixel detector foreseen in the Pixel upgrade of 2017. The iPipe measurements are a good indication of the stability of the structure, since strain deformations only of the order of $20\mu\epsilon$ has been measured during the CMS magnet ramps, when the whole CMS structure is known to be subjected to magnetic field induced deformations of the order of 10 mm. These measurements were indeed a direct indication of the correct design manufacturing and operation of the new CMS central beam pipe, even during the B-field induced stresses.

4 IPIPE MEASUREMENT OF THE BEAM INDUCED HEATING

4.1 BEAM INDUCED RF HEATING

A beam of charged particles, basically, moves inside an accelerator under the Lorentz force produced by the external electromagnetic fields generated, *e.g.*, from the guiding and focusing magnets and RF cavities. As the beam intensity increases, the electromagnetic fields self-generated by the beam, particularly the fields generated by the beam interacting with its surroundings, will perturb the external fields prescribed by the accelerator optics design, which is made considering the beam as a collection of noninteracting single particles [98]. These electromagnetic fields are called wake fields[1] since they remain usually behind the (ultra-relativistic) exciting particles. The wake fields can influence the motion of trailing particles, in the longitudinal and in one or both transverse directions, leading to energy losses, beam instabilities, or producing undesirable secondary effects such as excessive heating of sensitive components at or near the chamber wall, called beam-induced RF heating. Therefore, in practice the elements of the vacuum chamber should be designed to minimize the self-generated (secondary) electro-magnetic fields. For example, chambers with different cross-sections should be connected with tapered transitions; unnecessary cavities should be avoided; bellows should preferably be separated from the beam by shielding; plates should be grounded or terminated to avoid reflections; poorly conductive materials should be coated with a thin layer of very good conductor (such as copper) when possible, etc.

4.1.1 The phenomenon

The wake functions characterizes the electromagnetic interaction of the beam with the surrounding environment. The electromagnetic problem is posed setting the Maxwell's equations with the beam as source term and boundary conditions given by the structure in which the beam propagates [99]. A particle q_0 going through a device of length L, leaves behind an electromagnetic fields and a probe charged q at distance z will feel a force as a result (see Figure 59). The integral of this force over the device defines the wake function, assuming the particles to move with the same velocity $v = \beta c$, where c is the speed of light and β is the relativistic factor. A detailed calculation of the wake fields is given in [100].

1 The terminology *wake* comes from the consideration that, in the relativistic limit, the causality principle dictates that there can be no electromagnetic field in front of the beam.

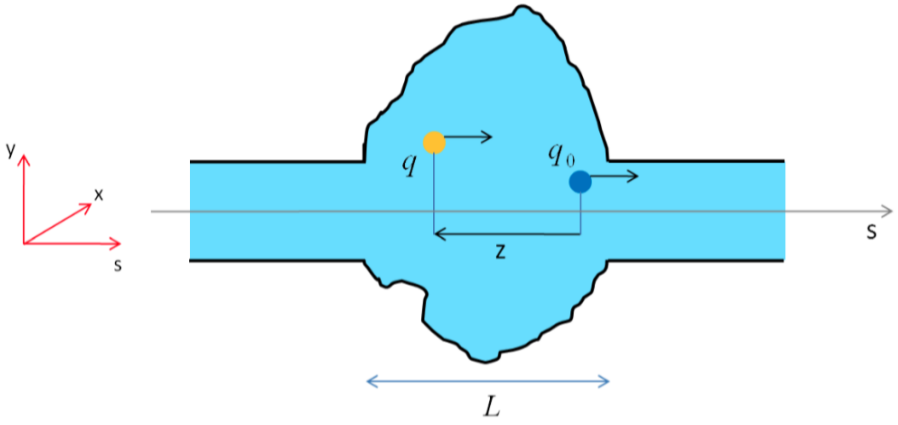

Figure 59: Pictorial representation of a device of arbitrary cross section along an accelerator.

It is often useful to examine the frequency content of the wake field, a time domain quantity, by performing a Fourier transform on it. This leads to the concept of impedance, a frequency domain quantity, which represents, for the plane under consideration (longitudinal, horizontal or vertical), the force integrated over the length of an element, from a source to a test wave (as a function of their frequency), normalized by their charges. As the conductivity, permittivity and permeability of a material depend in general on frequency, it is usually better (or easier) to treat the problem in the frequency domain. The idea of representing the accelerator environment by an impedance was introduced by Sessler and Vaccaro [101].
The RF fields generated by the proton beam interact with the beam surrounding materials and energy can be dissipated in the non-perfectly conducting walls, eventually leading to local heating; the LHC experience is widely described [102]. The power loss, which is due to the real part of the longitudinal impedance, is always proportional to the square of the number of particles per bunch but it depends on the frequency distribution of the impedance. It can be linear with the number of bunches, when the bunches are independent, *i.e.* for a wake-field that does not extend beyond a short range (or broadband impedance) which does not couple the consecutive bunches. On the other hand, it can be proportional to the square of the number of bunches, when the bunches are not independent, *i.e.* for a wake-field which couples the consecutive bunches, (or narrowband impedance), [103]. The power P_{loss} lost by a beam composed of M

equi-spaced and equi-populated bunches of N_b protons traveling in the aperture of an LHC equipment of longitudinal impedance Z_{long} is [102]:

$$P_{loss} = 2(eMN_b f_{rev})^2 \Big(\sum_{p=1}^{\infty} Re\big[Z_{long}(2\pi pMf_{rev})\big] \times Powerspectrum(2\pi pMf_{rev}) \Big) \tag{27}$$

where e is the proton charge, f_{rev} is the revolution frequency, the power spectrum of the bunch as a function of frequency is given by $Powerspectrum(f)$. In the frame of this formalism, it is important to note that the power loss is proportional to the square of the total intensity MN_b for a sharp narrowband impedance at resonating frequency $f_{resonator}$:

$$P_{loss} = 2(eMN_b f_{rev})^2 Re\big[Z_l(2\pi pMf_{resonator})\big] \times Powerspectrum(2\pi pMf_{resonator}) \Big) \tag{28}$$

if the resonating frequency coincides with one of the beam frequencies. On the other hand, the power loss is still proportional to the square of the bunch intensity N_b but linear with the number of bunches M for a broadband impedance:

$$P_{loss} = 2(eMN_b f_r)^2 \Big(\frac{1}{Mf_{rev}} \int_0^{+\infty} Re\big[Z_l(2\pi f)\big] \times Powerspectrum(2\pi f) \Big) \tag{29}$$

The $Powerspectrum(f)$ includes the information on the bunch length, which has a huge effect on the P_{loss}, as demonstrated in [104]. This consideration poses the request for detailed investigation on the beam induced RF heating in preparation for the High Luminosity LHC scenario, when the bunch intensity will double.

4.2 LHC OBSERVATIONS

Beam induced RF heating was one of the major limitations to increasing the LHC luminosity in Run 1 [103]. Temperature increase in near-beam devices, due to electromagnetic fields generated by the proton beam interacting with the longitudinal beam coupling impedance of these devices, was indeed observed to cause severe damage, delays or dumps [102]. During the first long LHC shutdown in 2013-14 (LS1), many actions were taken by CERN equipment groups as well as experiments to solve existing problems and prevent new ones for modified or newly installed hardware [105], while a summary of beam induced RF heating issues for 2015 is provided in [106].
The usual solutions to avoid beam-induced RF heating are the following, depending on the situation:

- Increase the distance between the beam and the equipment.
- Coat with a good conductor if the heating is predominantly due to resistive losses and not geometric losses.
- Close large volumes (which could lead to resonances at low frequency) and add a smooth transition. This is why beam screens and RF fingers are installed.
- Adding a material with losses allows reducing the amplitude of narrow-band impedance modes by broadening them, but the remaining power into that material has to be handled in a proper way.
- Improve the subsequent heat transfer:
  - Convection: there is none in vacuum.
  - Radiation: usually, the temperature is already quite high for the radiation to be efficient. One should therefore try and improve the emissivities of surrounding materials.
  - Conduction: good contacts and thermal conductivity are needed.
  - Active cooling: the LHC strategy was to water cool all the near beam equipment.
- Try and design an All Modes Damper (AMD) if possible, to remove the heat as much as possible to an external load outside vacuum, where it can be more easily cooled away. This can also work together with a damping ferrite.
- Increase the bunch length, but then the luminosity will be decreased due to the geometric reduction factor in the absence of crab cavities (and possible losses from the RF bucket). The longitudinal distribution can also play a very important role for some devices, and it should be kept under tight control.
- Install temperature monitoring on critical devices to warn about (and prevent) possible damages.

To extend the discovery potential of LHC a design study for a novel machine configuration, the High Luminosity LHC (HL-LHC), was started with the goal to increase its luminosity by a factor of 10 beyond its design value. Within the framework of the HL-LHC project [107] a first impedance estimation was done concerning new configuration. In particular, the impedance of the upgraded experimental beam pipe was also studied, since a reduction of diameter of the inner detector of CMS (inner radius from 29 mm to 21.7 mm) was proposed to increase the detector performance [108]. Studies showed an expected increase of $\sim$ 30% of the power loss for CMS vacuum chambers, from 1.4 W to 1.9 W per meter length.

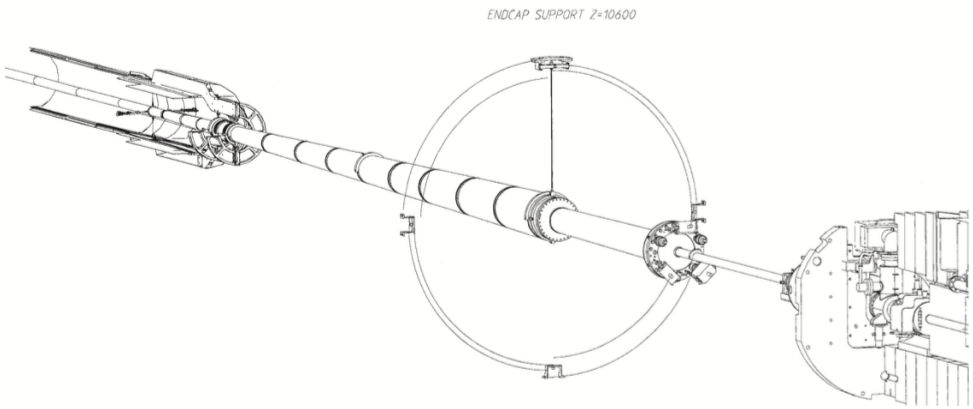

Figure 60: A 3D view of the presently installed CMS vacuum chamber. The beam pipe is shown from the interaction point to the compensation module.

4.3 CMS BEAM PIPE IMPEDANCES

The vacuum chamber inside of the CMS experiment is matched to the needs of the installed detector components. A 3D-view of the presently installed vacuum system is shown in Figure 60. The description of the structure of the CMS beam pipe, together with the comparison between the new and the old CMS central beam pipe, has been the subject of the previous chapter where more detailed pictures are shown. The calculation of the wake fields for the present, as well as for the former, designs of the whole CMS vacuum chamber are presented in [109], [110], [111], [112], [113]. The reduction of the central beam pipe diameter has been done in the frame of the HL-LHC requests coming from the upgrade of the CMS detector. A representation of the vacuum chamber of the CMS experiment for the HL-LHC in r-z-coordinates is shown in Figure 61: the vacuum chamber has a rotational symmetry along the z axis.

The wake fields and higher order modes of the new beam pipe of the CMS detector for the High Luminosity LHC configuration (HL-LHC) have been calculated and extensively discussed in [113]. The longitudinal and transverse effective impedances increase significantly with reduced radius and the power loss is increased by ∼30% by the radius reduction from 29mm to 21.7mm.

4.4 IPIPE DIRECT MEASUREMENTS

The iPipe monitoring system FBG sensors are placed on the outer surface of the CMS central beam pipe, in direct contact with the metallic surface.

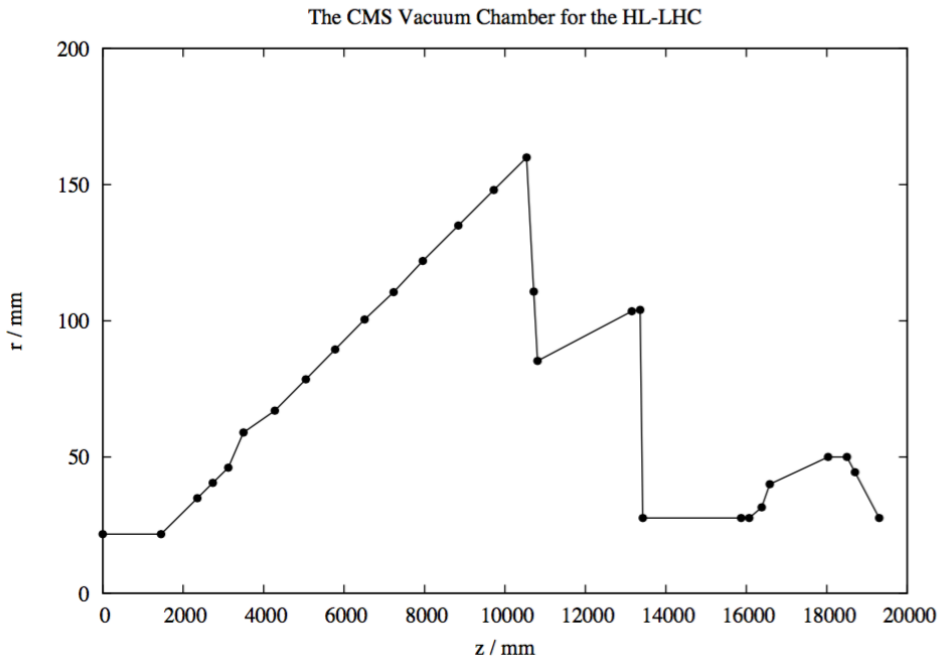

Figure 61: A representation of the vacuum chamber of the CMS experiment for the HL-LHC in r-z-coordinates. All dimensions are in mm. The interaction point (IP) is at z = 0 mm.

This peculiar, and unique, sensing position allow to measure for any thermal dynamic that took place on the vacuum chamber structure. Moreover, the system has been designed to take data 24/7 at 0.1Hz. In the frame of the beam induced heating phenomenon, it is interesting to focus the thermal analysis on the time interval defined from the moment when the protons are injected in the LHC machine the beams are tuned to the start of the collisions.

4.4.1 LHC Fill

Everything start with the injection of the protons in the LHC ring. They are easiest to get from hydrogen, the simplest atom with just one electron orbiting one proton. Indeed, the LHC starts with a bottle of hydrogen gas. An electric field is used to strip hydrogen atoms of their electrons to yield protons. Linac 2, the first accelerator in the chain, accelerates the protons to the energy of 50 MeV. The beam is then injected into the Proton Synchrotron Booster (PSB), which accelerates the protons to 1.4 GeV, followed by the Proton Synchrotron (PS), which pushes the beam to 25 GeV. Protons are then sent to the Super Proton Synchrotron (SPS) where they are accelerated to 450 GeV. The protons are finally transferred to the two beam pipes of the LHC to reach their maximum energy of 6.5 TeV. The beam in one pipe circulates clockwise while the beam in the other pipe circulates anti-clockwise.

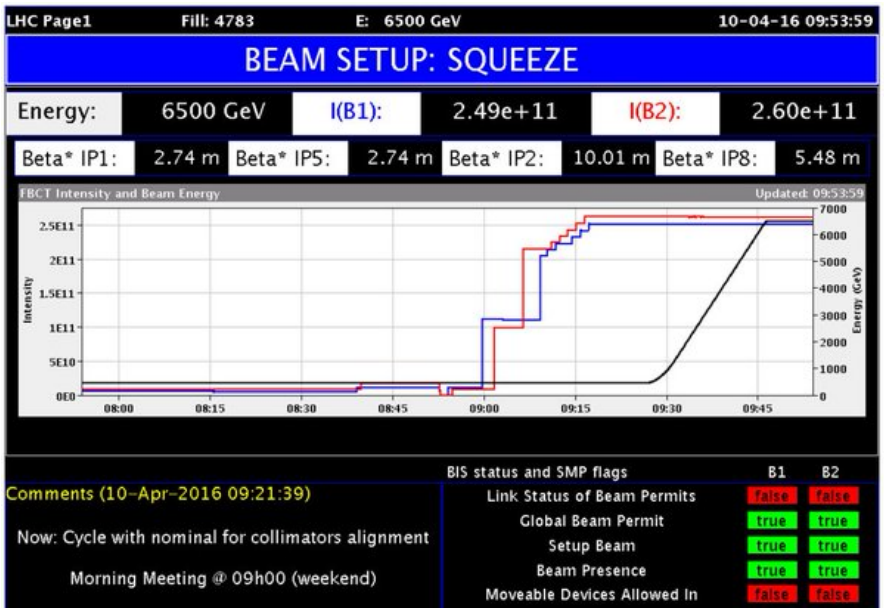

Figure 62: Screenshot from the LHC vistar page 1 during a standard Fill operation.

Beams circulate for many hours inside the LHC beam pipes under normal operating conditions. The two beams are brought into collision inside four detectors, ALICE, ATLAS, CMS and LHCb, where the total energy at the collision point is equal to 13 TeV. A screenshot from the LHC monitoring tool is reported in Figure 62.

Every Fill cycle is a sequence made of tightly coupled tasks that need to be carried out in strict order and have to be accomplished successfully to allow the LHC machine to make a transition from one state to another. A complete description of the LHC operating modes ca be found in [114], while part of those tasks, which are interesting for the subsequent considerations, are described in the following:

- SETUP: Possibly beam in transfer lines with transfer line dumps in. Includes pre-injection plateau and injection plateau - no beam in ring.
- ABORT: Recovery mode following beam permit drop. This mode can be entered from any state if there is no beam in the machine.
- INJECTION PROBE BEAM: If either ring 1 or ring 2 will be injected with or have safe beam circulating. In this mode a number of checks will be done for the different accelerator sub-systems before injecting higher intensities. The aim will be to establish a circulating safe beam with a given lifetime.
- INJECTION SETUP BEAM: During the INJECTION PROBE BEAM we will be able to make measurements with very limited precision. In order to make more precise measurements before filling for physics, a

SETUP BEAM will be used. This beam will be wholly representative of the physics beam to follow, just with fewer bunches to stay below the damage threshold.

- INJECTION PHYSICS BEAM: At this stage the machine has been optimized. It proved to be able to have circulating beam with appropriate lifetime and it is ready to accept higher intensities needed for physics. Within this mode, prior to high intensity beam injection, a pilot beam will be injected since the accelerator will be empty when this mode is reached.
- PREPARE RAMP: Injection complete, preparing for ramp.
- RAMP: Ready to ramp or ramping or immediate post ramp.
- FLAT TOP: Ramp finished - pre-squeeze checks.
- SQUEEZE: Preparing for or squeezing: the beams are fine-tuned, and focused at the four points around the LHC where they cross, and the experiments will record the collisions.
- ADJUST: Preparing for collisions or adjusting beams after the squeeze. Possible to enter this mode from STABLE BEAMS. Possible to enter this mode at the end of STABLE BEAMS without the intention of going back into physics.
- STABLE BEAMS: Stable conditions with collisions in the experiments: The LHC is now running smoothly, the beams are behaving as expected, and the experiments can start recording data.
- BEAM DUMP WARNING: This mode is used before a requested beam dump at the end of stable beams. It is bypassed in case of emergency dump.
- RAMP DOWN: Ramp down and cycling after programmed dump at end of physics fill.

4.4.2 iPipe beam induced heating

The thermal behavior of the CMS central beam pipe during a typical LHC fill, as recorded by the iPipe monitoring system is shown in Figure 63. To achieve this result the database in which the iPipe data are stored has been merged with a dedicated LHC database where all the information about the fills are stored during the LHC operations. Indeed, the black line in the plot in Figure 63 represents the intensity of one of the two LHC proton beams, whose maximum value is $1.08 \cdot 10^{11}$protons. At a first observation, it can be seen that while the LHC is performing its initial operations, during the ramp, the CMS central beam pipe temperature is increasing, while when the collisions

start and, consequently, the beam intensity decreases, the temperature on the pipe is decreasing.
Focusing on the right part of the plot in Figure 63(a) and moving to the plot in Figure 63(a), it can be seen that the temperature increase is factorable in two parts. As the beam intensity starts to increase there is a temperature increase on the pipe between the injection of the physics beam and the declaration of stable beam, while a further temperature increase is recorded by the iPipe sensors after the stable beam declaration. Further data analysis and correlations with status of subdetectors sorrounding the beampipe, show that the latter temperature increase corresponds to the heat generated by the start of the CMS data taking, *e.g.* the activation of the electronic board of the detectors (Silicon Pixel detector of the CMS inner tracker) surrounding the beam pipe.
The first temperature increase is clearly related to the presence of the beam in the pipe and can be associated to the above described RF beam induced heating phenomenon, since any other source of beam heating can be excluded. Indeed, there can be other sources of beam induced heating than wakefields:

- synchrotron radiation, but the CMS central beam pipe is a straight section of the LHC ring and no synchrotron radiation is forseen; 1tem direct beam losses, that is why we focus on period before collisions and resulting losses;

- electron cloud, the presence of the CMS magnetic field inhibit the electrons of the cloud from interacting with the vacuum chamber walls.

Moreover, the central beam pipe is located in the tracker volume, which is a thermal and humidity controlled environment. A detailed analysis has been performed and the results are presented in the following section.

To understand the nature of the beam induced heating on the CMS Central beam pipe a corresponding analysis between the beam parameters and the iPipe measured ΔT has been performed. Figure 64(a) shows the temperatura increase and the number of bunches (M) for each fill during the 2016 LHC operations, while in Figure 64(b) the delta temperature are plotted against the number of bunches, for the temperatura sensor at 50mm from the impact point. The latter plot is the direct measurement of the correlation between the temperature increase and the number of bunches per Fill, which goes in the direction of a linear correlation. From what described in the previous sections concerning the beam RF induced heating, this linear behavior can be seen as the confirmation of a broadband impedance for the CMS central beam pipe.
In Figures 65, 66 and 67 the results for the beryllium, negative and positive, and the aluminum central beam pipe sectors are shown.

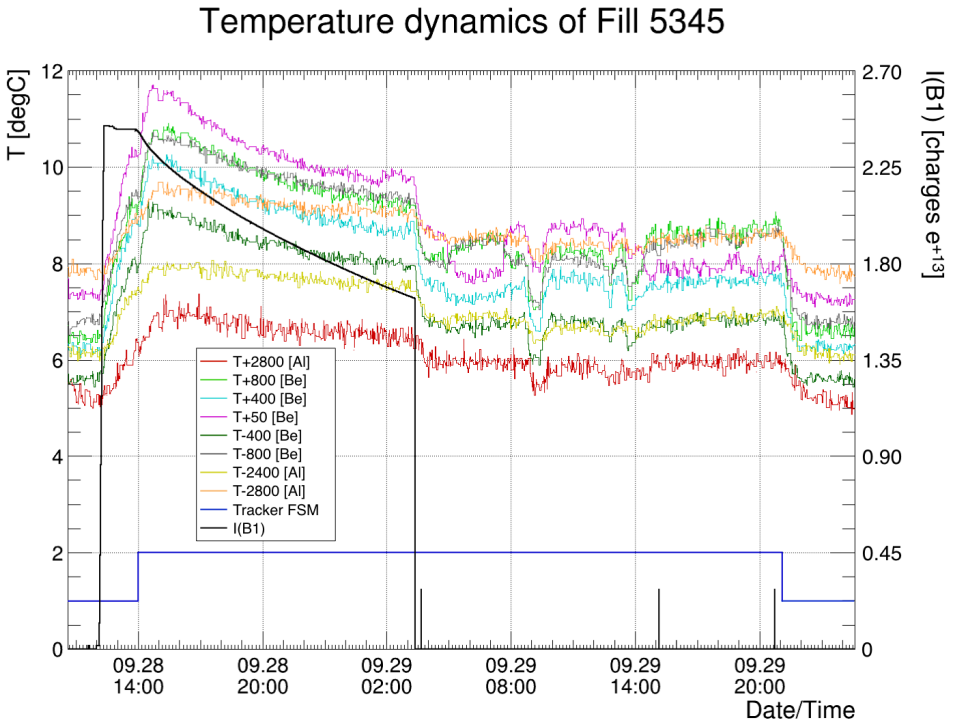

(a)

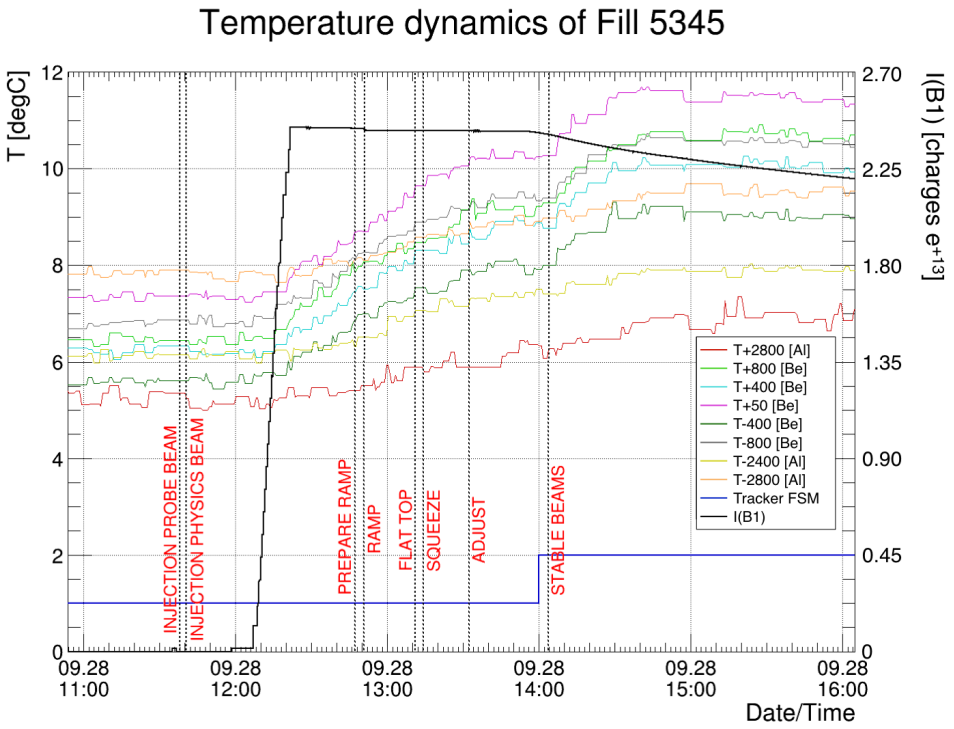

(b)

Figure 63: Thermal dynamic on the CMS central beam pipe during the LHC Fill 5345 happened in September 2016 (a) and highlight of the temperature increase during the beams filling and setting phases (b).

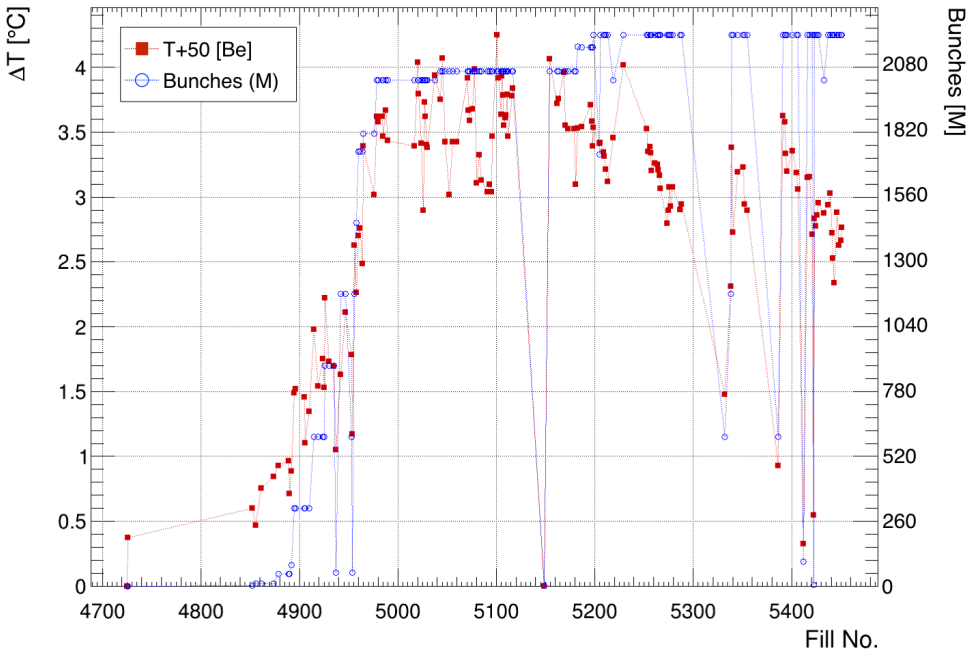

(a)

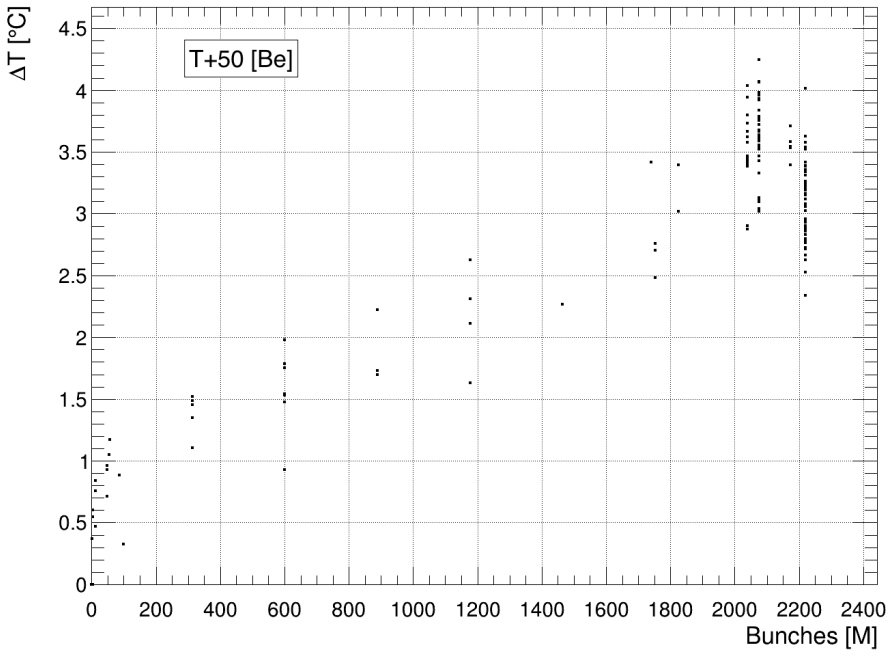

(b)

Figure 64: Temperature increase between *injection of probe beam* and *stable beam* (a) and correlation between the number of bunches [M] and the temperature variation of each Fill (b) occurred in 2016 LHC operation.

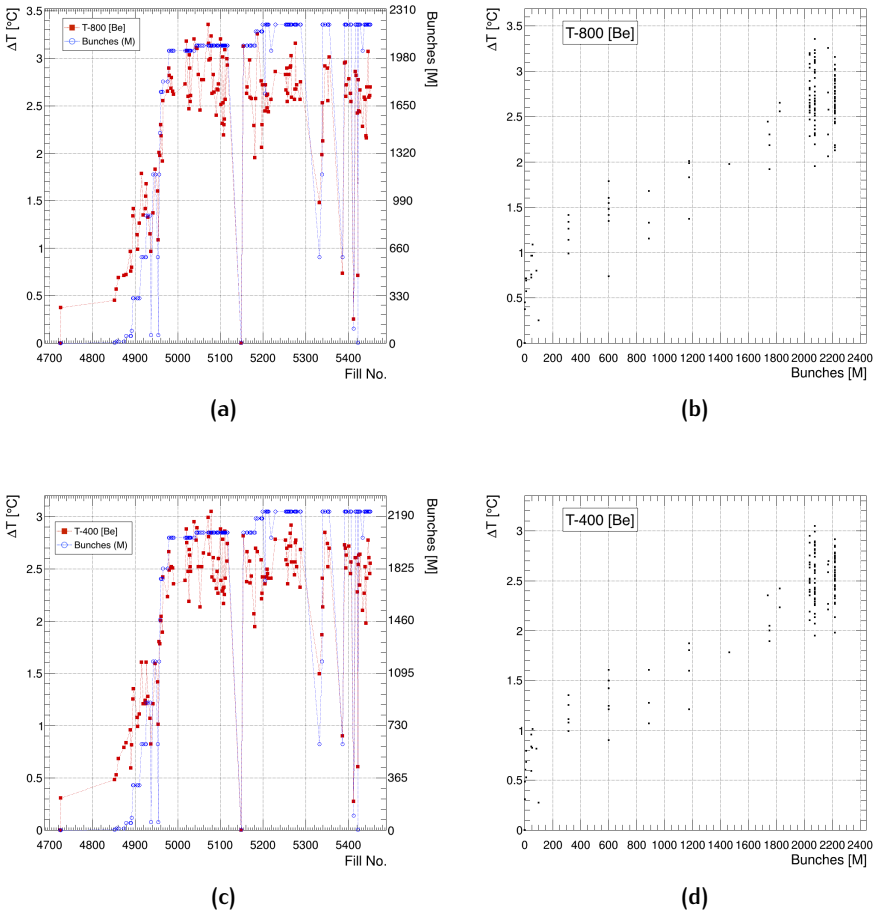

Figure 65: Temperature increase between *injection of probe beam* and *stable beam* (a,c) and correlation between the number of bunches [M] and the temperature variation of each Fill occurred in 2016 LHC operation (b,d) on the beryllium minus region (T-800 and T-400, respectively).

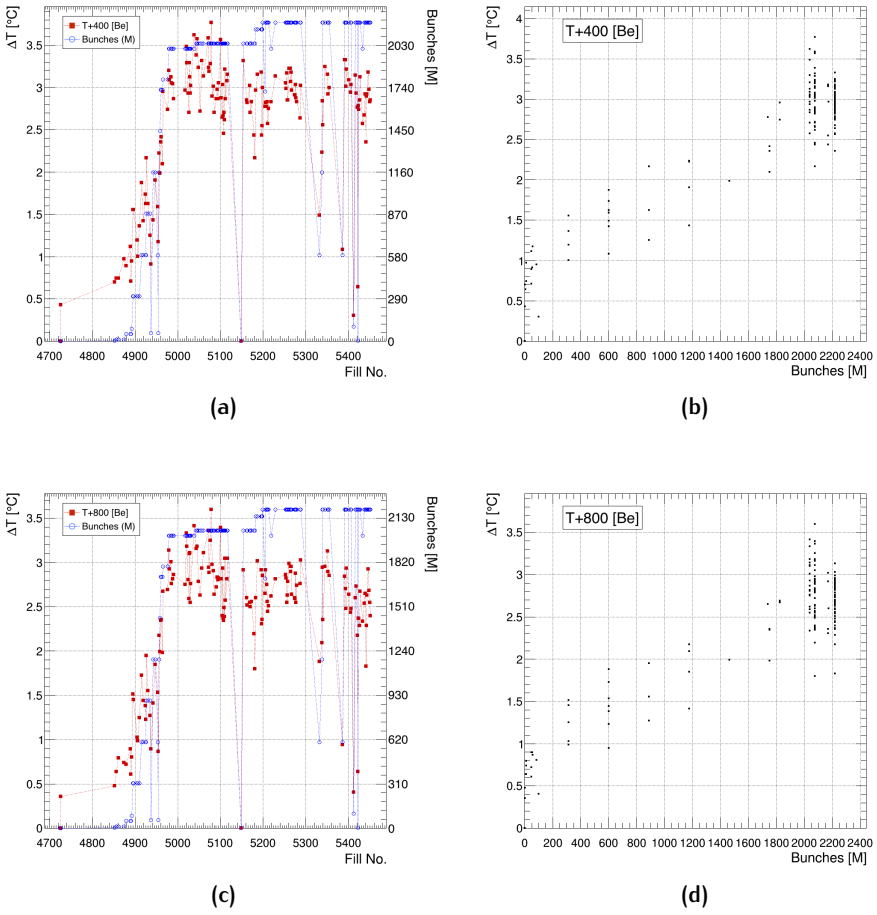

Figure 66: Temperature increase between *injection of probe beam* and *stable beam* (a,c) and correlation between the number of bunches [M] and the temperature variation of each Fill occurred in 2016 LHC operation (b,d) on the beryllium plus region (T+400 and T+800, respectively).

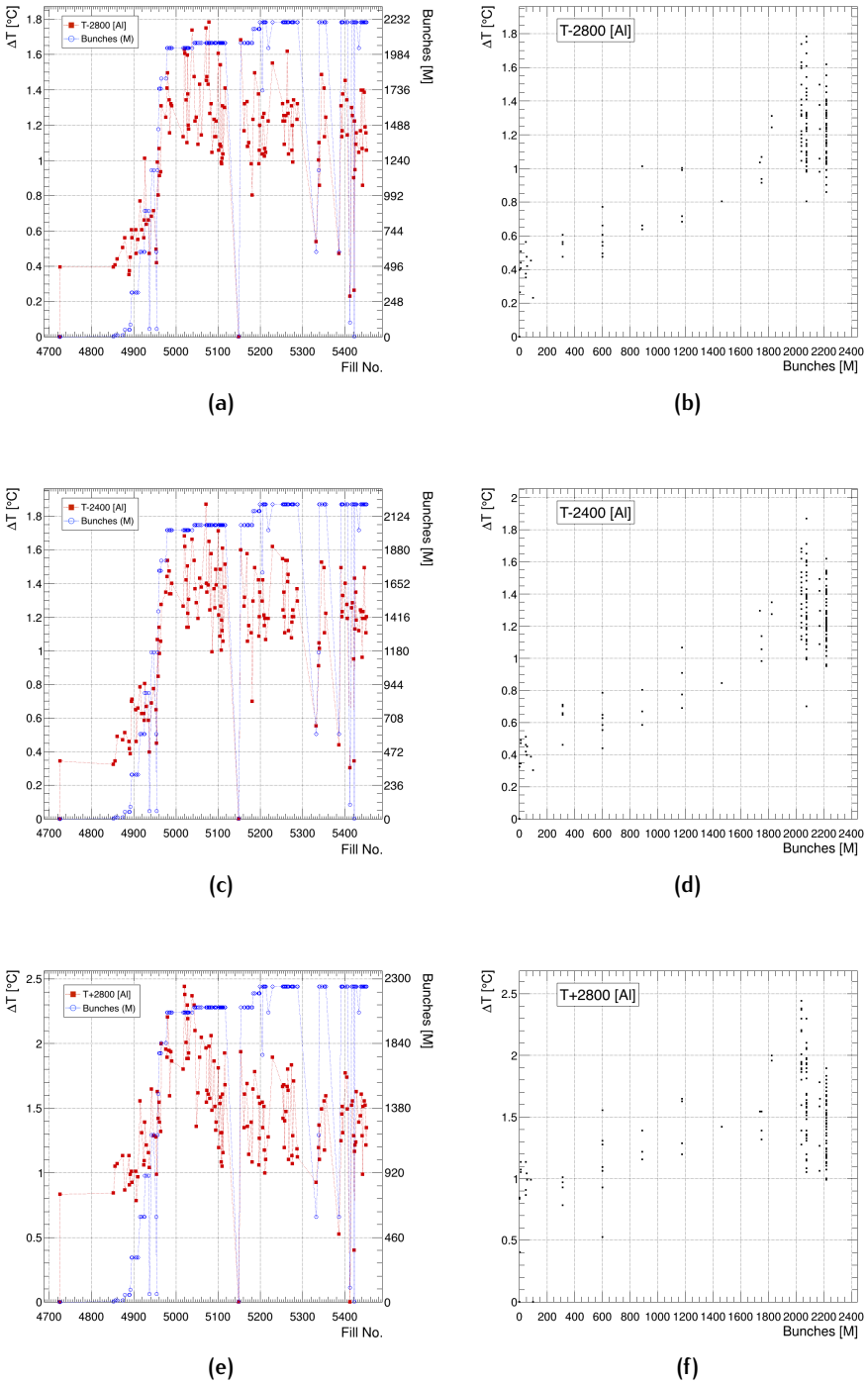

Figure 67: Temperature increase between *injection of probe beam* and *stable beam* (a,c,e) and correlation between the number of bunches [M] and the temperature variation of each Fill occurred in 2016 LHC operation (b,d,f) on the aluminum region (T-2800, T-2400 and T+2800, respectively).

4.5 IPIPE UPGRADE

Following the excellent results achieved in the direct measurement of the beam RF induced heating on the CMS central beam pipe, the CMS Collaboration decided that the iPipe monitoring system will be installed also to the $z = \pm 10$ m sectors, with respect to the impact point, located in the CMS HF pipe zones, referring to the technical drawing in Figure 60. Indeed, from the calculation discussed in [113] the presence of a mode trapped at the end of the End-cap pipe, about $\pm$10m from the interaction point, is highlighted resulting in a potential power loss up to 250W [115] if it is excite by the wake of the beam. This scenario poses the need for a continuous and reliable monitoring of this sections of the CMS beam pipe. With the support of the CMS Central Technical Coordination, we have designed an upgrade of the iPipe system to satisfy this request, coming from both the CMS and the LHC communities.

The $z = \pm 10$ m zones are characterized by a particular double cone shape geometry, which is responsible for the predicted trapped mode. The variation of the CMS beam pipe radius is reported in Figure 61. The HF beam pipe is made of stainless steel, 3mm thick. The zones to be monitored consist of 1.5m around the $z = \pm$10.7m flanges; the layout of this upgrade of the iPipe is shown in Figure 68(a). Referring to the CMS conventional coordinate system, the iPipe system upgrade includes the sensoring of both the plus and minus z region, with respect to the IP. For each $z = 10$ m region it is divided in IP side and non-IP side, due to the presence of the flanges at $z = \pm 10.7$ m which identify a no-fibers region of 29 cm, as depicted in Figure 68. On both IP and non-IP sides the monitoring system consists of four FBGs arrays, each one made of four FBG to be used as temperature sensors, to be placed on the four cardinal positions. The proposed sensors distribution is depicted in the schematic in Figure 68(b): the distance between two consecutive FBG is 25 cm. In Figure 69 some photos taken during this recent FBGs arrays installation are shown.

This system is designed to stand the high ionizing radiation level that will be produced during the next years LHC collisions in this region. Indeed, based on the arguments and test measurements discussed in the previous chapter and on the studied on the state of the art of the radiation tolerance of the FBG sensors argued in the first chapter of this Thesis, the iPipe upgrade arrays are made with fluorine-doped fibers, namely the Fujikura RRSMFA [116], where the FBG sensors will be written with the use of the femtosecond laser technology [27].

The system is now under commissioning and will be ready to take data when the LHC operation will resume at the end of the 2017 year end technical stop.

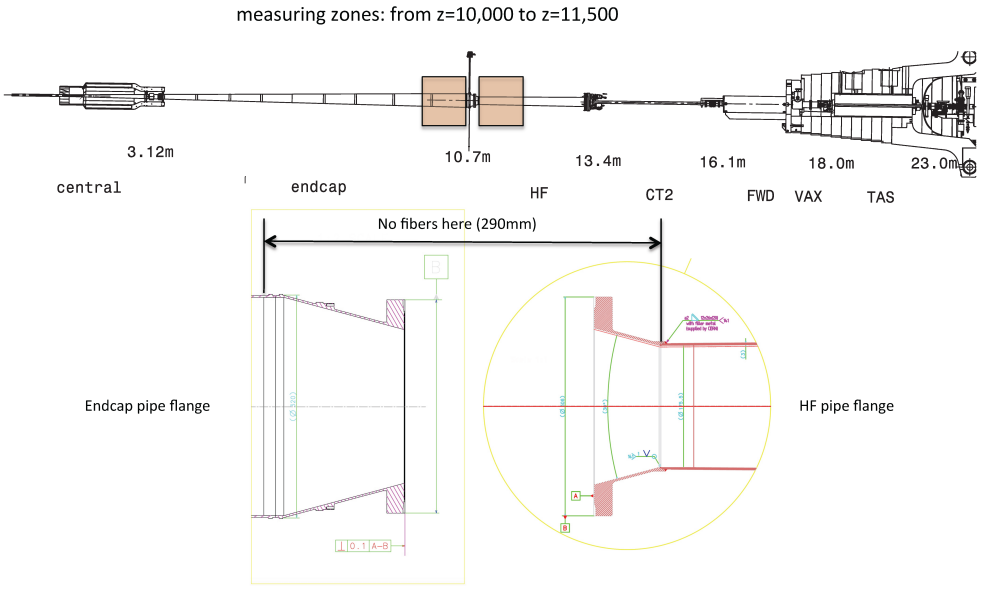

(a)

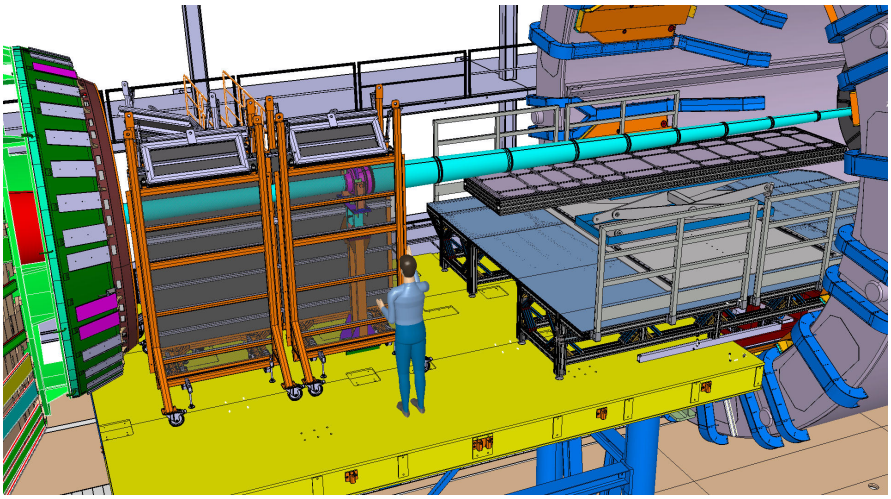

(b)

Figure 68: Schematic of the zone around the $z = \pm 10.7$ m supports of the CMS beam pipe to be equipped with a FBGs temperature monitoring system and 3D view of the CMS configuration, with the radiation shielding in position, needed to install the arrays for the iPipe upgrade (b).

(a) (b) (c) (d) (e) (f)

Figure 69: Picture of the CMS in open configuration with the working platform in place (a); focus on the radiation shielding around the z = 10.7 m support (b); installation of the FBG arrays and fan-in fan-out LC-APC patch-panel (c,d); detailed view of one of the FBGs arrays installed (e,f).

4.6 CONCLUSIONS AND FUTURE PERSPECTIVES

The beam RF induced heating is a key effect to be monitored during the operations of a particle accelerator. In particular, the LHC has faced this issue during the Run1 collisions when the beam RF induced heating posed some limitations to the performances of the machine, [104]. The LHC chosen strategy to mitigate the beam RF induced heating comprise also the temperature monitoring of the critical parts of the LHC accelerator ring. The temperature monitoring is not always a trivial task and conventional electronic sensor not always can be used in the specific harsh environments represented by the LHC accelerator components. Indeed, the presence of magnetic field (up to 8.5 T in the bending sector on the LHC ring), as well as the very high level of ionizing radiation, makes the electronic temperature sensors unreliable for long term measurement during the LHC operations.
The iPipe monitoring system, which has been the subject of present PhD thesis work, turned to be a solid and reliable solution for these challenging temperature monitoring tasks as well. The iPipe system data analysis proved in particular the precision and reproducibility for the measurement of local thermal gradients on the accelerator sectors. The data shown in present chapter highlight the reliability of the iPipe sensing method applied to the monitoring of the beam RF induced heating: those data can be seen as the first direct measure of the beam RF induced heating on the CMS central beam pipe, made possible by the uniqueness of the iPipe monitoring system. Indeed, as already underlined in the previous chapter, the CMS central beam pipe is the first, successful, example of direct measurements of the temperature dynamic of a particle accelerator impact sector.
The data presented in Figures 64, 65, 66 and 67 are a clear evidence of a linear correlation between the temperature increase and the number of bunches of each LHC fill, confirming with a direct measurement the hypothesis of resistive wall impedance for the CMS central beam pipe. Moreover, from the data shown in Figure 67 we can state that the aluminum sectors turns to get less warm with respect to the beryllium sector giving an first indirect indication that the narrow-band impedance resonances, predicted to be at $z = \pm 10.7$ m with respect to the impact point [113], may not have been excited during the last two year of LHC operations.
The results presented in this chapter have triggered the interest of the CMS and LHC communities. A first solid outcome is the request of the upgrade of the iPipe system, in order to directly measure the temperature dynamic around the $z = \pm 10.7$ m zone of the CMS beam pipe. A direct monitoring of these zones will be of crucial importance in the framework of the HL-LHC, since the predicted narrow-band impedance resonances can, potentially, dissipate up to 250 W in these regions. Recently, we installed the new iPipe sensors and the system is now under commissioning in order to be ready to record data when the LHC collision will resume at the end of the YETS2017. Moreover, the data recorded will be integrated also in the TIMBER platform

[117, 118], the user interface to the LHC Logging System [119], in order to be shared on line with the LHC team.
The whole CMS beam pipe 32 will be changed in LS2 with a new one to cope with the HiLumi-LHC and CMS-Phase II requests [120]. Since the installation should take place before the end of 2020, the design and feasibility studies have already started and the CMS Central Technical Coordination supports the installation of a completely new iPipe monitoring system from $z = -16$ m to $z = +16$ m, that is to say on the entire length of this new beam pipe.

CONCLUSIONS

The work presented in present Thesis has focused on the innovative application of a fiber optic monitoring system to the central beam pipe of the CMS experiment.
The central beam pipe is a fundamental element of both, the CMS experiment and the LHC ring: it is the place where the high energy proton-proton collisions take place in CMS underground site. It has to stand to an extreme vacuum condition (up to 10^{-13} atm) and, at the same time, it must not interfere with the particle resulting from collisions. To satisfy those conditions, in its final version, the central beam pipe is made of a gossamer Beryllium tube that needs to be continuously monitored to have information about its structural and health state. In addition, it is mandatory that, any monitoring system to be installed on the beam pipe must not interfere with the particle detectors that wrap around the pipe, nor create interferences on the operation of surrounding CMS particle detectors. Radiation immunity represents one of the most important specification required to a monitoring system operating in a High Energy Physics (HEP) environment, while other needs are: low complexity layout, multiplexing and multi-parameters measurement capabilities. On the basis of these technical specifications, we designed and installed a unique structural system based on Fibre Bragg Grating (FBG) sensors, that has been called iPipe monitoring system, on the new central beam pipe of the CMS experiment to monitor the thermal condition and on-line unpredictable mechanical deformations.
Present Thesis work has been of fundamental importance for the design and manufacturing of the iPipe system, its installation, commissioning and operation. The performed, and here presented, data analysis confirm that the iPipe system fulfilled the initial monitoring requests, quantifying any deformation induced on the CMS central beam pipe during the experiment operations. Moreover, the data presented proved the overall high sensitivity and reliability of this innovative monitoring system.
The measure of the mechanical stability of the CMS central beam pipe was of critical importance in the view of the reduction of the clearance between the beam pipe and the surrounding Pixel detector foreseen in the Pixel upgrade of 2017. The iPipe measurements are a good indication of the stability of the

structure since strain deformations only of the order of 20 $\mu\epsilon$ has been measured during the CMS magnet ramps, when the whole CMS structure is known to be subjected to magnetic field induced deformations of the order of 10 mm. The iPipe system has indeed proved to be an important innovation in the framework of the monitoring of crucial parts of the CMS detector and LHC beam pipe.

Focusing on the thermal measurements, the iPipe system proved the capability also for direct measurement of the beam induced RF heating on the CMS central beam pipe. The beam RF induced heating is a key effect to be monitored during the operations of a particle accelerator. In particular, the LHC has faced this issue during the Run1 collisions when the beam RF induced heating posed some limitations to the performances of the machine. The temperature monitoring of the different elements of the LHC accelerator is not always a trivial task and conventional electronic sensor cannot be used in all the harsh environments represented by the LHC accelerator components. Indeed, the presence of magnetic field (up to 8.5T in the bending sector on the LHC ring), as well as the very high level of ionizing radiation, makes the electronic temperature sensors unreliable for long term measurement during the LHC operations. The iPipe monitoring system, turned out to be a solid and reliable solution for these challenging temperature monitoring tasks, in particular for the measurement of local thermal gradients on the accelerator sectors. The thermal data analysis, performed in present Thesis work, has highlighted the reliability of the iPipe sensing method applied to the monitoring of the beam RF induced heating. Those data can be seen as the first direct measure of the beam RF induced heating on the CMS central beam pipe, made possible by the uniqueness of the iPipe monitoring system. Indeed, the CMS central beam pipe is the first, successful, example of direct measurements of the temperature dynamic of a particle accelerator in the sector where particles collide. The results presented in the chapter 4 have triggered a further interest of the CMS and LHC communities. As a first outcome we collected the request of the upgrade of the iPipe system, in order to directly measure the temperature dynamic around the z = 10.7 m zone of the CMS beam pipe. A direct monitoring of these zones is of crucial importance in the frame of the HL-LHC, since the predicted narrow-band impedance resonances can, potentially, dissipate up to 250W in this region. We have recently installed the new iPipe sensors by and the system is going to be commissioned in order to be ready for data-taking we the LHC operation will resume. Moreover, the recorded data will be shared in a common platform with the LHC team.

Moreover, an extended upgrade of iPipe monitoring system have been recently confirmed in the framework of the renovation of the whole CMS beam pipe, that will happen during LS2, before the end of 2020.

The iPipe system is a unique and innovative solution which will represent a milestone for beam pipe monitoring in high energy physics. Its first

implementation, documented in present Thesis work, proved the capability of direct measurements of beam pipe thermal and strain dynamics, opening new perspectives in the manufacturing of solid and reliable structural health monitoring system in this domain.

BIBLIOGRAPHY

[1] T. Erdogan, "Fiber grating spectra," *Journal of lightwave technology*, vol. 15, no. 8, pp. 1277–1294, 1997.

[2] H. Henschel, S. K. Hoeffgen, K. Krebber, J. Kuhnhenn, and U. Weinand, "Influence of fiber composition and grating fabrication on the radiation sensitivity of fiber bragg gratings," in *Radiation and Its Effects on Components and Systems, 2007. RADECS 2007. 9th European Conference on*, pp. 1–8, IEEE, 2007.

[3] A. Faustov, P. Saffari, C. Koutsides, A. Gusarov, M. Wuilpart, P. Megret, K. Kalli, and L. Zhang, "Highly radiation sensitive type ia fbgs for future dosimetry applications," *IEEE transactions on nuclear science*, vol. 59, no. 4, pp. 1180–1185, 2012.

[4] A. Gusarov and S. K. Hoeffgen, "Radiation effects on fiber gratings," *IEEE Transactions on Nuclear Science*, vol. 60, no. 3, pp. 2037–2053, 2013.

[5] J.-L. Caron, *Layout of the LEP tunnel including future LHC infrastructures.*, vol. LHC-PHO-1997-057. CERN, Feb 1997. AC Collection. Legacy of AC. Pictures from 1992 to 2002.

[6] G. M. Berruti, P. Petagna, S. Buontempo, A. Makovec, Z. Szillasi, N. Beni, M. Consales, and A. Cusano, "One year of fbg-based thermo-hygrometers in operation in the cms experiment at cern," *Journal of Instrumentation*, vol. 11, no. 03, p. P03007, 2016.

[7] D. A. Matzner Dominguez, D. Abbaneo, K. Arndt, N. Bacchetta, A. Ball, E. Bartz, W. Bertl, G. M. Bilei, G. Bolla, H. W. K. Cheung, *et al.*, *CMS Technical Design Report for the Pixel Detector Upgrade*. CERN, 2012.

[8] G. Rajan, *Optical Fiber Sensor: advaced techniquee and applications*. CRC press, 2015.

[9] K. Grattan and T. Sun, "Fiber optic sensor technology: an overview," *Sensors and Actuators A: Physical*, vol. 82, no. 1, pp. 40–61, 2000.

[10] A. D. Kersey, M. A. Davis, H. J. Patrick, M. LeBlanc, K. Koo, C. Askins, M. Putnam, and E. J. Friebele, "Fiber grating sensors," *Journal of lightwave technology*, vol. 15, no. 8, pp. 1442–1463, 1997.

[11] V. Bhatia and A. M. Vengsarkar, "Optical fiber long-period grating sensors," *Optics letters*, vol. 21, no. 9, pp. 692–694, 1996.

[12] R. Kashyap, *Fiber bragg gratings*. Academic press, second ed., 2009.

[13] K. O. Hill and G. Meltz, "Fiber bragg grating technology fundamentals and overview," *Journal of lightwave technology*, vol. 15, no. 8, pp. 1263–1276, 1997.

[14] A. M. Vengsarkar, P. J. Lemaire, J. B. Judkins, V. Bhatia, T. Erdogan, and J. E. Sipe, "Long-period fiber gratings as band-rejection filters," *Journal of lightwave technology*, vol. 14, no. 1, pp. 58–65, 1996.

[15] S. W. James and R. P. Tatam, "Optical fibre long-period grating sensors: characteristics and application," *Measurement science and technology*, vol. 14, no. 5, p. R49, 2003.

[16] K. Hill, Y. Fujii, D. C. Johnson, and B. Kawasaki, "Photosensitivity in optical fiber waveguides: Application to reflection filter fabrication," *Applied physics letters*, vol. 32, no. 10, pp. 647–649, 1978.

[17] G. Meltz, W. Morey, and W. Glenn, "Formation of bragg gratings in optical fibers by a transverse holographic method," *Optics letters*, vol. 14, no. 15, pp. 823–825, 1989.

[18] D. Lam and B. K. Garside, "Characterization of single-mode optical fiber filters," *Applied Optics*, vol. 20, no. 3, pp. 440–445, 1981.

[19] A. Yariv, "Coupled-mode theory for guided-wave optics," *IEEE Journal of Quantum Electronics*, vol. 9, no. 9, pp. 919–933, 1973.

[20] P. J. Lemaire, R. Atkins, V. Mizrahi, and W. Reed, "High pressure h/sub 2/loading as a technique for achieving ultrahigh uv photosensitivity and thermal sensitivity in geo/sub 2/doped optical fibres," *Electronics Letters*, vol. 29, no. 13, pp. 1191–1193, 1993.

[21] K. O. Hill, B. Malo, F. Bilodeau, D. Johnson, and J. Albert, "Bragg gratings fabricated in monomode photosensitive optical fiber by uv exposure through a phase mask," *Applied Physics Letters*, vol. 62, no. 10, pp. 1035–1037, 1993.

[22] A. Othonos and X. Lee, "Novel and improved methods of writing bragg gratings with phase masks," *IEEE Photonics Technology Letters*, vol. 7, no. 10, pp. 1183–1185, 1995.

[23] B. Malo, J. Albert, K. Hill, F. Bilodeau, D. Johnson, and S. Theriault, "Enhanced photosensitivity in lightly doped standard telecommunication fibre exposed to high fluence arf excimer laser light," *Electronics Letters*, vol. 31, no. 11, pp. 879–880, 1995.

[24] T. Erdogan and J. Sipe, "Tilted fiber phase gratings," *JOSA A*, vol. 13, no. 2, pp. 296–313, 1996.

[25] G. C. Righini, A. Tajani, and A. Cutolo, *An introduction to optoelectronic sensors*, vol. 7. World Scientific, 2009.

[26] A. Cusano, A. Cutolo, and J. Albert, *Fiber Bragg grating sensors: recent advancements, industrial applications and market exploitation*. Bentham Science Publishers, 2011.

[27] S. A. Slattery, D. N. Nikogosyan, and G. Brambilla, "Fiber bragg grating inscription by high-intensity femtosecond uv laser light: comparison with other existing methods of fabrication," *JOSA B*, vol. 22, no. 2, pp. 354–361, 2005.

[28] H. Kogelnik, "Coupled wave theory for thick hologram gratings," *Bell Labs Technical Journal*, vol. 48, no. 9, pp. 2909–2947, 1969.

[29] I. Malitson, "Interspecimen comparison of the refractive index of fused silica*," *Josa*, vol. 55, no. 10, pp. 1205–1209, 1965.

[30] A. D. Kersey, "A review of recent developments in fiber optic sensor technology," *Optical fiber technology*, vol. 2, no. 3, pp. 291–317, 1996.

[31] Y. Li, Z. Hua, F. Yan, and P. Gang, "Metal coating of fiber bragg grating and the temperature sensing character after metallization," *Optical Fiber Technology*, vol. 15, no. 4, pp. 391–397, 2009.

[32] K. Krebber, H. Henschel, and U. Weinand, "Fibre bragg gratings as high dose radiation sensors?," *Measurement Science and Technology*, vol. 17, no. 5, p. 1095, 2006.

[33] D. A. Barber and N. H. Rizvi, "Practical study of the effects of exposure conditions on the quality of fiber bragg gratings written with excimer and argon-ion lasers," in *Photonics Fabrication Europe*, pp. 16–25, International Society for Optics and Photonics, 2003.

[34] T.-E. Tsai, G. M. Williams, and E. J. Friebele, "Index structure of fiber bragg gratings in gesio2 fibers," *Optics letters*, vol. 22, no. 4, pp. 224–226, 1997.

[35] J.-L. Archambault, L. Reekie, and P. S. J. Russell, "100% reflectivity bragg reflectors produced in optical fibres by single excimer laser pulses," *Electronics Letters*, vol. 29, no. 5, pp. 453–455, 1993.

[36] L. Dong, W. Liu, and L. Reekie, "Negative-index gratings formed by a 193-nm excimer laser," *Optics letters*, vol. 21, no. 24, pp. 2032–2034, 1996.

[37] S. Pissadakis and M. Konstantaki, "Type iia gratings recorded in b-ge codoped optical fibre using 213 nm nd: Yag radiation," in *Optical Communication, 2005. ECOC 2005. 31st European Conference on*, vol. 3, pp. 563–564, IET, 2005.

[38] E. Lindner, J. Canning, C. Chojetzki, S. Brückner, M. Becker, M. Rothhardt, and H. Bartelt, "Thermal regenerated type iia fiber bragg

gratings for ultra-high temperature operation," *Optics Communications*, vol. 284, no. 1, pp. 183–185, 2011.

[39] Y. Liu, J. Williams, L. Zhang, and I. Bennion, "Abnormal spectral evolution of fiber bragg gratings in hydrogenated fibers," *Optics letters*, vol. 27, no. 8, pp. 586–588, 2002.

[40] A. Simpson, K. Kalli, K. Zhou, L. Zhang, and I. Bennion, "Formation of type ia fibre bragg gratings in germanosilicate optical fibre," *Electronics Letters*, vol. 40, no. 3, pp. 163–164, 2004.

[41] G. Simpson, K. Kalli, K. Zhou, L. Zhang, and I. Bennion, "Blank beam fabrication of regenerated type ia gratings," *Measurement Science and Technology*, vol. 15, no. 8, p. 1665, 2004.

[42] S. J. Mihailov, C. W. Smelser, P. Lu, R. B. Walker, D. Grobnic, H. Ding, G. Henderson, and J. Unruh, "Fiber bragg gratings made with a phase mask and 800-nm femtosecond radiation," *Optics letters*, vol. 28, no. 12, pp. 995–997, 2003.

[43] S. J. Mihailov, C. W. Smelser, D. Grobnic, R. B. Walker, P. Lu, H. Ding, and J. Unruh, "Bragg gratings written in all-sio2 and ge-doped core fibers with 800-nm femtosecond radiation and a phase mask," *Journal of Lightwave Technology*, vol. 22, no. 1, p. 94, 2004.

[44] C. W. Smelser, S. J. Mihailov, and D. Grobnic, "Hydrogen loading for fiber grating writing with a femtosecond laser and a phase mask," *Optics letters*, vol. 29, no. 18, pp. 2127–2129, 2004.

[45] C. W. Smelser, S. J. Mihailov, and D. Grobnic, "Formation of type i-ir and type ii-ir gratings with an ultrafast ir laser and a phase mask," *Optics express*, vol. 13, no. 14, pp. 5377–5386, 2005.

[46] C. Liao and D. Wang, "Review of femtosecond laser fabricated fiber bragg gratings for high temperature sensing," *Photonic Sensors*, pp. 1–5, 2013.

[47] A. Gusarov, D. Starodubov, F. Berghmans, O. Deparis, Y. Defosse, A. F. Fernandez, M. Decréton, P. Mégret, and M. Blondel, "Comparative study of the mgy dose level γ-radiation effect on fbgs written in different fibres," in *Proc. SPIE*, vol. 3746, pp. 608–611, 1999.

[48] D. Grobnic, H. Henschel, S. K. Hoeffgen, J. Kuhnhenn, S. J. Mihailov, and U. Weinand, "Radiation sensitivity of bragg gratings written with femtosecond ir lasers," in *SPIE Defense, Security, and Sensing*, pp. 73160C–73160C, International Society for Optics and Photonics, 2009.

[49] A. Morana, *Gamma-rays and neutrons effects on optical fibers and Bragg gratings for temperature sensors*. PhD thesis, Saint Etienne, 2013.

[50] S. Vasiliev, E. Dianov, K. Golant, O. Medvedkov, A. Tomashuk, V. Karpov, M. Grekov, A. Kurkov, B. Leconte, and P. Niay, "Performance of bragg and long-period gratings written in n-and ge-doped silica fibers under/spl gamma/-radiation," in *Radiation and Its Effects on Components and Systems, 1997. RADECS 97. Fourth European Conference on*, pp. 480–483, IEEE, 1997.

[51] X. Lan, Q. Han, T. Wei, J. Huang, and H. Xiao, "Turn-around-point long-period fiber gratings fabricated by co _{2} laser point-by-point irradiations," *IEEE Photonics Technology Letters*, vol. 23, no. 22, pp. 1664–1666, 2011.

[52] S. Kher, S. Chaubey, R. Kashyap, and S. M. Oak, "Turnaround-point long-period fiber gratings (tap-lpgs) as high-radiation-dose sensors," *IEEE Photon. Technol. Lett.*, vol. 24, no. 9, pp. 742–744, 2012.

[53] H. Henschel, S. K. Hoeffgen, J. Kuhnhenn, and U. Weinand, "High radiation sensitivity of chiral long period gratings," *IEEE Transactions on Nuclear Science*, vol. 57, no. 5, pp. 2915–2922, 2010.

[54] A. Gusarov, S. Vasiliev, O. Medvedkov, I. Mckenzie, and F. Berghmans, "Stabilization of fiber bragg gratings against gamma radiation," in *Radiation and Its Effects on Components and Systems, 2007. RADECS 2007. 9th European Conference on*, pp. 1–8, IEEE, 2007.

[55] V. Neustruev, E. Dianov, V. Kim, V. Mashinsky, M. Romonov, A. Guryanov, V. Khopin, and V. Tikhomirov, "Ultraviolet radiation- and γ radiation-induced color centers in germanium-doped silica glass and fibers," *Fiber & Integrated Optics*, vol. 8, no. 2, pp. 143–156, 1989.

[56] F. Berghmans, A. F. Fernandez, B. Brichard, F. Vos, M. C. Decreton, A. I. Gusarov, O. Deparis, P. Megret, M. Blondel, S. Caron, *et al.*, "Radiation hardness of fiber optic sensors for monitoring and remote handling applications in nuclear environments," in *Photonics East (ISAM, VVDC, IEMB)*, pp. 28–39, International Society for Optics and Photonics, 1999.

[57] A. Gusarov, B. Brichard, and D. Nikogosyan, "Gamma-radiation effects on bragg gratings written by femtosecond uv laser in ge-doped fibers," *IEEE Transactions on Nuclear Science*, vol. 57, no. 4, pp. 2024–2028, 2010.

[58] H. Henschel, S. K. Hoeffgen, J. Kuhnhenn, and U. Weinand, "Influence of manufacturing parameters and temperature on the radiation sensitivity of fiber bragg gratings," *IEEE Transactions on Nuclear Science*, vol. 57, no. 4, pp. 2029–2034, 2010.

[59] S. Lin, N. Song, J. Jin, X. Wang, and G. Yang, "Effect of grating fabrication on radiation sensitivity of fiber bragg gratings in gamma

radiation field," *IEEE Transactions on Nuclear Science*, vol. 58, no. 4, pp. 2111–2117, 2011.

[60] A. Gusarov, F. Berghmans, A. F. Fernandez, O. Deparis, Y. Defosse, D. Starodubov, M. Decreton, P. Mégret, and M. Bondel, "Behavior of fibre bragg gratings under high total dose gamma radiation," *IEEE Transactions on Nuclear Science*, vol. 47, no. 3, pp. 688–692, 2000.

[61] A. Gusarov, C. Chojetzki, I. Mckenzie, H. Thienpont, and F. Berghmans, "Effect of the fiber coating on the radiation sensitivity of type i fbgs," *IEEE Photonics Technology Letters*, vol. 20, no. 21, pp. 1802–1804, 2008.

[62] S. K. Hoeffgen, H. Henschel, J. Kuhnhenn, U. Weinand, C. Caucheteur, D. Grobnic, and S. J. Mihailov, "Comparison of the radiation sensitivity of fiber bragg gratings made by four different manufacturers," *IEEE Transactions on Nuclear Science*, vol. 58, no. 3, pp. 906–909, 2011.

[63] A. F. Fernandez, B. Brichard, F. Berghmans, and M. Decreton, "Dose-rate dependencies in gamma-irradiated fiber bragg grating filters," *IEEE Transactions on Nuclear Science*, vol. 49, no. 6, pp. 2874–2878, 2002.

[64] A. I. Gusarov and D. B. Doyle, "Modeling of gamma-radiation impact on transmission characteristics of optical glasses," *Photonics for Space and radiation Environments II*, vol. 4547, pp. 78–85, 2002.

[65] A. Gusarov, F. Berghmans, O. Deparis, A. F. Fernandez, Y. Defosse, P. Mégret, M. Decréton, and M. Blondel, "High total dose radiation effects on temperature sensing fiber bragg gratings," *IEEE Photonics technology letters*, vol. 11, no. 9, pp. 1159–1161, 1999.

[66] H. Henschel, D. Grobnic, S. K. Hoeffgen, J. Kuhnhenn, S. J. Mihailov, and U. Weinand, "Development of highly radiation resistant fiber bragg gratings," *IEEE Transactions on Nuclear Science*, vol. 58, no. 4, pp. 2103–2110, 2011.

[67] A. F. Fernandez, A. I. Gusarov, S. Bodart, K. Lammens, F. Berghmans, M. Decre, P. Me, M. Blondel, A. Delchambre, *et al.*, "Temperature monitoring of nuclear reactor cores with multiplexed fiber bragg grating sensors," *Optical Engineering*, vol. 41, no. 6, pp. 1246–1254, 2002.

[68] A. Gusarov, A. F. Fernandez, S. Vasiliev, O. Medvedkov, M. Blondel, and F. Berghmans, "Effect of gamma–neutron nuclear reactor radiation on the properties of bragg gratings written in photosensitive ge-doped optical fiber," *Nuclear Instruments and Methods in Physics Research Section B: Beam Interactions with Materials and Atoms*, vol. 187, no. 1, pp. 79–86, 2002.

[69] A. Gusarov, D. Kinet, C. Caucheteur, M. Wuilpart, and P. Mégret, "Gamma radiation induced short-wavelength shift of the bragg peak in type i fiber gratings," *IEEE Transactions on Nuclear Science*, vol. 57, no. 6, pp. 3775–3778, 2010.

[70] Y.-J. Rao, "Recent progress in applications of in-fibre bragg grating sensors," *Optics and lasers in Engineering*, vol. 31, no. 4, pp. 297–324, 1999.

[71] Micron Optics, Inc., "http://www.micronoptics.com/."

[72] L. Evans and P. Bryant, "LHC Machine," *JINST*, vol. 3, p. S08001, 2008.

[73] ATLAS collaboration, "The ATLAS Experiment at the CERN Large Hadron Collider," *JINST*, vol. 3, p. S08003, 2008.

[74] CMS Collaboration, "The CMS Experiment at the CERN LHC," *JINST*, vol. 3, p. S08004, 2008.

[75] ALICE Collaboration, "The ALICE experiment at the CERN LHC," *JINST*, vol. 3, p. S08002, 2008.

[76] LHCb Collaboration, "The LHCb Detector at the LHC," *JINST*, vol. 3, p. S08005, 2008.

[77] CMS Collaboration, *The CMS tracker system project : Technical Design Report*, vol. CERN-LHCC-98-06. CERN, 1998.

[78] CMS Collaboration, *The CMS electromagnetic calorimeter project: Technical Design Report*, vol. CERN-LHCC-97-33. CERN, 1997.

[79] CMS Collaboration, *The CMS hadron calorimeter project: Technical Design Report*, vol. CERN-LHCC-97-31. CERN, 1997.

[80] CMS Collaboration, *The CMS muon project: Technical Design Report*, vol. CERN-LHCC-97-32. CERN, 1997.

[81] A. L. Angelis and A. D. Panagiotou, "CASTOR: A dedicated detector for the detection of centauros and strangelets at the LHC," *Journal of Physics G: Nuclear and Particle Physics*, vol. 23, no. 12, p. 2069, 1997.

[82] Z. Szillási, S. Buontempo, N. Béni, G. Breglio, A. Cusano, A. Laudati, M. Giordano, A. Saccomanno, D. Druzhkin, and A. Tsirou, "One year of fos measurements in cms experiment at cern," *Physics Procedia*, vol. 37, pp. 79–84, 2012.

[83] R. Arcidiacono, "CMS DCS design concepts," in *10th ICALEPCS Int. Conf. on Accelerator and Large Expt. Physics Control Systems*, 2005.

[84] Distribution Information Management system DIM, "http://dim.web.cern.ch/dim."

[85] PVSS, "https://readthedocs.web.cern.ch/display/ICKB/WinCC-OA+Service."

[86] JCOP framework, "http://itcobe.web.cern.ch/itcobe/Projects/."

[87] F. Fienga, N. Beni, G. Breglio, S. Buontempo, M. Consales, A. Cusano, R. Favre-Felix, A. Gaddi, M. Giordano, and A. Irace, "Fiber optic sensors structural monitoring of the beam pipe in the cms experiment at the cern," *Fotonica AEIT Italian Conference on Photonics Technologies*, 2015.

[88] F. Fienga, N. Beni, G. Breglio, S. Buontempo, M. Consales, A. Cusano, A. Gaddi, A. Irace, M. Giordano, and Z. Szillasi, "Fibre optic sensors structural health monitoring of the central beam pipe in the cms experiment at the cern laboratories," in *EWSHM2016 European Workshop on Structural Health Monitoring*, 2016.

[89] M. Huhtinen, A. Rubbia, and P. A. Aarnio, "Calculation of neutron background generated by various beam pipe geometries at LHC," *Nucl. Instrum. Meth.*, vol. A351, pp. 236–239, 1994.

[90] P. A. Aarnio and M. Huhtinen, *Beam pipe related background revisited*, vol. CMS-IN-1997/025. CERN, 1997.

[91] M. Huhtinen, *Impact of beam-pipe geometry on radiation background in CMS*, vol. CMS-IN-2000/069. CERN, 2000.

[92] F. Feyzi *et al.*, "Cms beam pipe support and protection manual," tech. rep., CERN, 2010.

[93] B. Jeanneret, *Geometrical acceptance in LHC v5.0*, vol. LHC-PROJECT-NOTE 111. CERN, 1997.

[94] S. Agostinelli, J. Allison, K. a. Amako, J. Apostolakis, H. Araujo, P. Arce, M. Asai, D. Axen, S. Banerjee, G. Barrand, *et al.*, "GEANT4, a simulation toolkit," *Nuclear instruments and methods in physics research section A: Accelerators, Spectrometers, Detectors and Associated Equipment*, vol. 506, no. 3, pp. 250–303, 2003.

[95] G. Battistoni, F. Cerutti, A. Fasso, A. Ferrari, S. Muraro, J. Ranft, S. Roesler, P. Sala, M. Albrow, and R. Raja, "The FLUKA code: Description and benchmarking," in *AIP Conference proceedings*, vol. 896, pp. 31–49, AIP, 2007.

[96] F. Ramos, "Preliminary mechanical analysis of the new cms central beam pipe," tech. rep., CERN, 2012.

[97] F. Leaux *et al.*, "Gluing tests of stycast 2850 ft lv24 on 316l, al 2219 and be plates," tech. rep., CERN, 2014.

[98] A. W. Chao, *Physics of collective beam instabilities in high energy accelerators*. Wiley, 1993.

[99] C. Zannini, *Electromagnetic Simulation of CERN accelerator Components and Experimental Applications*. PhD thesis, CERN, 2013-03-11.

[100] L. Palumbo, V. G. Vaccaro, and M. Zobov, "Wake fields and impedance," in *Advanced accelerator physics. Proceedings, 5th Course of the CERN Accelerator School, Rhodos, Greece, September 20-October 1, 1993. Vol. 1, 2*, pp. 331–390, 1994.

[101] A. Sessler and V. G. Vaccaro, *ISR-RF/67-2*. CERN, 1967.

[102] B. Salvant *et al.*, "Beam induced RF heating," in *Evian Workshop on LHC beam operation*, 2012.

[103] E. Metral, "Rf heating from wake losses in diagnostic structures," in *Internation Beam Instrumentation Conference IBIC2013*, 2013.

[104] E. Metral *et al.*, "Beam-induced heating / bunch length / rf and lessons for 2012," in *LHC Performance Workshop*, 2012.

[105] B. Salvant *et al.*, "Update on Beam Induced RF Heating in the LHC," in *4th International Particle Accelerator Conference IPAC2013*, 2013.

[106] B. Salvant *et al.*, "Beam induced RF heating in LHC in 2015," in *7th International Particle Accelerator Conference IPAC2016*, 2016.

[107] A. Barachetti, L. Rossi, and A. Szeberenyi, *High Luminosity Large Hadron Collider Design Study, Final Project Report: Deliverable D1.14*, vol. CERN-ACC-2016-0007. CERN, 2016.

[108] Veness *et al.*, "Specification of new vacuum chambers for the lhc experimental interactions," in *4th International Particle Accelerator Conference IPAC2013*, 2013.

[109] O. Bruning, *Loss Factor and Longitudinal Higher Order Modes in the CMS Experimental Chamber*, vol. LHC Project Note 14. CERN, 1995.

[110] R. Wanzenberg, *Calculation of Higher Order Modes and Wakefields for the Vacuum Chamber of the CMS Experiment at the LHC*, vol. LHC Project Note 418. CERN, 2009.

[111] E. Metral and R. Wanzenberg, "Wake and higher order mode computation for cms experimental chamber at the lhc," in *Particle Accelerator Conference PAC09*, 2009.

[112] A. Ball, "Beampipe design/approval/procurement," Pix meeting, CERN, 2011.

[113] R. Wanzenberg and O. Zagorodnova, *Calculation of Wakefields and Higher Order Modes for the New Design of the Vacuum Chamber of the CMS Experiment for the HL-LHC*, vol. CERN-ATS-Note-2013-018. CERN, 2013.

[114] M. Lamont, R. Alemany, and S. Page, *Functional specification LHC Modes*, vol. LHC-OP-ES-0005. CERN, 2007.

[115] E. Metral, *High Luminosity Large Hadron Collider Design Study, Beam Intensity Limitations*, vol. CERN-ACC-2014-0297. CERN, 2014.

[116] K. Aikawa *et al.*, "Radiation-resistant single-mode optical fibers," *Fujikura Giho*, 2008.

[117] TIM Operations Portal, "http://cern.ch/tim-operation/."

[118] J. Stowisek *et al.*, *Technical infrastructure monitoring from the CCC*, vol. CERN-TS-Note-2005-015. CERN, 2005.

[119] LHC Logging Project, "http://lhc-logging.web.cern.ch/lhc-logging/."

[120] W. Zeuner, "Cms beam pipe exchange," CMS Week, CERN, Apr. 2017.